University of Alberta

Detailed examination of iron meteorites and impact generated carbonaceous spherules associated with the Whitecourt Meteorite Impact Crater, Alberta, Canada

by

Jennifer Diane Newman

A thesis submitted to the Faculty of Graduate Studies and Research
in partial fulfillment of the requirements for the degree of

Master of Science

Earth and Atmospheric Sciences

Spring 2014
Edmonton, Alberta

Abstract

The impact of an iron meteorite <1100 years ago near Whitecourt, Alberta, Canada formed a crater 36 m in diameter. The impacting body fragmented upon impact, scattering thousands of shrapnel-shaped fragments around the crater. Internal examination of the fragments reveal that the mineralogy is consistent with a type IIIAB iron meteorite and most of the deformations in texture observed is a result of the impact. The high preservation of the impact site has protected the meteorite fragments from severe weathering as well as preserving small amorphous carbonaceous spherules distributed in the soil surrounding the crater. The carbonaceous spherules were generated during the impact when biomass was heated rapidly enough to form molten spherules which were then dispersed by the expanding impact plume. The examination of preserved meteorites and spherules provide insights into low-energy meteorite impacts, which are rare in the current terrestrial impact record.

Acknowledgements

I would like to acknowledge funding for this project was provided by the Natural Sciences and Engineering Research Council (NSERC) grant 261740-08 and to the Canadian Space Agency (CSA) and Western University for the ASTRO/CPSX Graduate Student Travel Award to present this work at the 44th Lunar and Planetary Science Conference.

For sample analysis at the University of Alberta I would like to thank Nathan Guerin and George Braybrook (scanning electron microscope), Ilona Ranger, Tom Chacko, and Andrew Locock (electron microprobe), Mark Labbe and Martin Von Dollen (sample prep), Diane Caird (X-ray diffraction), Igor Jakob (photography), and Greg Baniak and Tiffany Playter (micro-CT training). I would also like to thank Randy Kofman for providing data and sharing his knowledge and insight of the impact site from his previous study of the area.

Documentation and the ability to study a significant portion of meteorites from the impact site was essential to many areas of this study and could not have been accomplished without the time and effort provided by local and foreign meteorite hunters including Brad Newman, Murray Paulson, Luc and Joan Guillemette, Wito Jakielaszek, Rick Huziak, Geoff Notkin, Steve Arnold, Rob Wesel, Mike Bandli, Jason Phillips, Jeff Kuyken, and the numerous volunteers that have spent a day or more searching and recording meteorite finds, every meteorite counts. I would also like to thank Rod Stevens and family for their initial discovery of the impact crater, continued search efforts, documentation of finds, and donation of meteorites to the University of Alberta for study and preservation.

And most of all I would like to thank my supervisor Chris Herd for first introducing me to the Whitecourt crater all those years ago, taking the time to look at the meteorites I had recovered after weekend trips to the impact site, and ultimately for suggesting I take on this project. His help and guidance regarding this research are greatly appreciated.

Table of Contents

List of Tables

List of Figures

CHAPTER 1: Introduction

1.1. Introduction

Meteors are common atmospheric events which last for short durations before completely burning up, leaving no material to reach Earth's surface. Larger fireball events are more brilliant but often break apart or explode during atmospheric transit so only small fragments reach the surface; a recent example occurred on February 15, 2013 near Chelyabinsk, Russia (Chernogor and Rozumenko, 2013). Even rarer are events where material survives atmospheric transit intact creating an impact crater when it reach Earth's surface. Transit through Earth's atmosphere is a destructive process where meteorites are ablated and usually fragment; ablation refers to the heating of the exterior surface where the surface melt is evaporated and oxidized (Badyukov and Raitala, 2012). If fragmentation occurs at an altitude of several km, in the lower and more dense atmosphere, similar to the Sikhote-Alin fall in 1947, then pieces become smoothed and often regmaglypted (thumbprint-like sculpting of surface) with lower altitudes producing more angular fragments (Krinov, 1966). Smoothing is caused by the ablation of the meteorite's external surface. A thin fusion crust forms on the outer surface and when formed on iron meteorites has a composition of fully and partially oxidized metal, such as magnetite (Buchwald, 1975). The heat from ablation penetrates deeper than the fusion crust causing the outer rim to melt. This thermally altered rim is called the heat alteration zone and is identified by its rapidly cooled recrystallized texture (Axon, 1969). Melt driven from the meteorite's surface during atmospheric ablation is usually vaporized but if melt droplets are large enough they solidify to create ablation spherules such as those from the Sikhote-Alin event (Krinov, 1966; Badyukov and Raitala, 2012).

Meteorites that fragment and survive their atmospheric passage have a characteristic distribution on Earth's surface called a strewnfield. The meteorites within a strewnfield have an ellipse-shaped distribution where the major axis of the ellipse corresponds to the direction of fall and the minor axis represents the lateral dispersion along the direction of fall (Norton, 2002). The lower in the atmosphere that fragmentation occurs, the smaller the extent of the resulting ellipse will be. The Sikhote-Alin fall was observed to have several atmospheric fragmentation events low in the atmosphere which is reflected in the small distribution area of 2.1 km by 0.96 km (Krinov, 1966). Within distribution ellipses there is also a mass sorting component where more massive fragments travel farther and fall last in the downrange direction, with less massive samples occupying the opposite end of the ellipse (Norton, 2002). This same concept can be applied to multiple crater forming events or a combination of cratering and fragmentation as observed at the Henbury crater field in Australia or Sikhote-Alin, where distribution is based on fragment mass (Roddy et al., 1988; Buhl and McColl, 2012; Krinov, 1966). A number of variables can affect the outcome of cratering events caused by a meteorite including the angle, speed, diameter, and composition of the impactor.

Another decisive factor affecting crater properties is the geographic location and the nature of the target material. Since Earth's surface is mostly covered by water many falls are not recoverable whereas land impacts have a better chance of being preserved. Some locations are more favourable, such as cold or hot deserts, where the lack of precipitation prevents crater erosion and meteorite weathering (Munoz et al., 2007). Meteorites and craters can potentially be found anywhere on Earth, but the likelihood of discovery is based on local environmental factors of temperature, precipitation, and human activity. The length of time these are preserved, or their terrestrial age, increases when mechanical and chemical weathering rates are low (Norton, 2002). Young, well-preserved terrestrial impact craters are rare yet they can provide valuable insights into the impact event and the diversity of factors that influence crater characteristics.

1.2. Origin and components of IIIAB iron meteorites

Iron meteorites formed early in the evolution of our solar system through the process of differentiation. Differentiation occurs when an accreting planetary body becomes large enough to generate internal heat causing the heavier components, such as Fe and Ni, to melt and migrate to the center of the body forming a metallic core. Heat is also supplied by the decay of short lived radiogenic isotopes, especially ^{26}Al (Haack and McCoy, 2007). Studies using the short-lived ^{182}Hf-^{182}W radiogenic isotope system have placed the timing of differentiation 1-2.5 Myr after Solar System formation (Kleine et al., 2005). Differentiation of the silicate and metal phases of the parent body make this an ideal system as hafnium is lithophile and tungsten is siderophile. Following differentiation the body cools slowly then a large collision sometime during the subsequent history of the parent body disrupts and fragments it to its core. The magnitude of the collision can send some fragments in various directions with the potential of impacting other objects or pieces can remain in the asteroid belt for millions of years before being dislodged from their orbit by resonances with other objects. In the case of the Whitecourt meteorite an iron core fragment from such a collision crossed Earth's orbit less than 1100 years ago which created the Whitecourt Meteorite Impact Crater (WMIC).

Iron meteorites are predominantly Fe-Ni alloys and as such their structure and composition are influenced by the behaviour of phases in the Fe-Ni system. The structures of the two primary Fe-Ni alloys kamacite and taenite are related to cooling temperatures associated with different phases of iron; kamacite contains α-iron and taenite has γ-iron. Gamma-iron exists when the temperature of pure iron is above 910°C and has a face-centred cubic (fcc) lattice. Upon cooling to 910°C the transformation to the body-centered cubic (bcc) α-iron phase begins (Uhlig, 1954). Each iron phase is able to accommodate the substitution of Ni atoms, which are randomly distributed throughout the lattice, for any of the iron atoms. An increase in Ni content compared to pure iron reduces the temperature at which the γ to α transformation will occur; 10% Ni lowers the transformation temperature to about 700°C (Uhlig, 1954).

Iron meteorites are classified based on chemical and structural properties (Krot et al., 2007). Octahedrites are the most common iron meteorite and are divided further based on the width of kamacite (Fe-Ni) lamellae from coarsest to finest. Kamacite lamellae are the main component of the iron meteorite-specific texture called the Widmanstätten pattern, which crystallizes as parallel lamellae in an octahedral arrangement (Fig. 1-1a). The Widmanstätten pattern is readily visible in polished samples etched in nitol; nitol is a solution of 10% HNO_3 and 90% ethanol (e.g. Norton, 2002; Szurgot et al., 2008). Octahedral crystallization of kamacite occurs in three dimensions so intra- or inter-sample variation may exist after etching, depending on how the meteorite was cut in relation to the octahedral orientation (Fig. 1-1b). This texture in octahedrites shows the intergrowth of Fe-Ni metal phases resulting in lamellae of varying widths among the octahedrite group but the widths remain nearly constant within a specific meteorite. Width is related to cooling rate of the parent body where wider lamellae indicate a large diameter body and slower cooling rate. Whitecourt meteorites belong to the medium

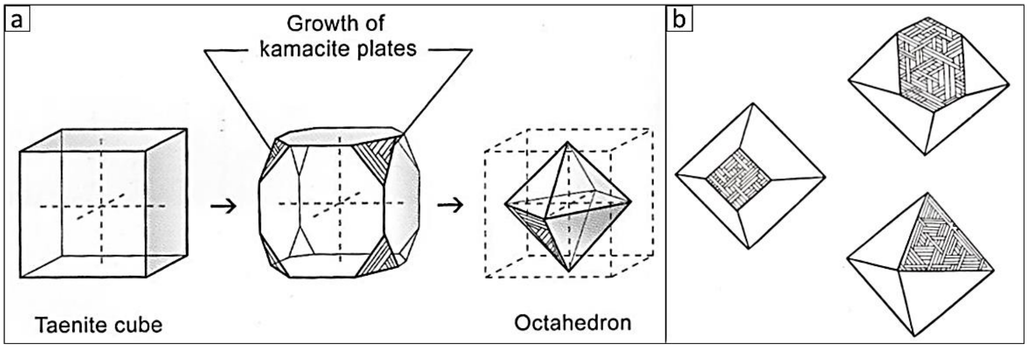

Figure 1-1: (a) As meteoritic iron cools from cubic taenite, kamacite lamellae truncate the cube corners resulting in an octahedral kamacite structure. [from Norton and Chitwood, 2008] (b) Widmanstätten pattern as it would appear parallel to (100), (110), and (111) faces of the parent taenite crystal. [from Buchwald, 1975]

octahedrite structural group, and the IIIAB chemical group (Herd et al., 2008). Type IIIAB is the largest of the 13 chemical groups which are determined by log plots of trace elements, such as Ir, Ga, and Ge, versus Ni (Fig. 1-2). All but two of these chemical groups are considered to be

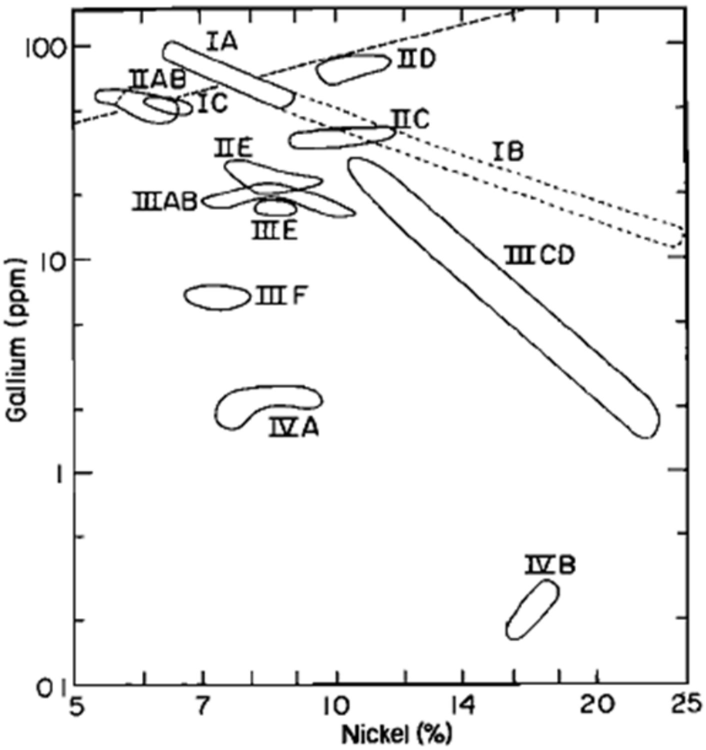

Figure 1-2: Logarithmic plot of gallium (Ga) versus nickel (Ni) for iron meteorite groups. [from Scott and Wasson, 1975]

magmatic irons meaning they were formed by fractional crystallization of differentiated parent bodies (Krot et al., 2007). Type IIIAB irons are considered to be magmatic in origin and by combining this with information from their structural group (almost exclusively medium octahedrite) the IIIAB parent body had a cooling rate of 50 K Myr^{-1} which corresponds to a diameter of about 50 km (Haack and McCoy, 2007). In addition to the primary Fe-Ni metal composition of iron meteorites, type IIIABs are known to contain mainly sulfide and phosphide accessory minerals with rarer occurrences of carbides, nitrides, and graphite (Scott and Wasson, 1975).

1.3. Impact spherules

Characteristics of terrestrial craters are variable due to the diversity of conditions involved in their formation. Similarly the production of any type of impact melt should have a similar diversity, due to variations in target material. Several types of spherules have been reported in terrestrial impact craters which differ in their composition, indicating different origins and conditions of formation. Impact spherules can have diverse compositions but are typically metallic or silicate-rich, reflecting either the meteorite composition or target material (Table 1-1). Both materials are melted and/or vaporized during a typical impact. The surviving melt solidifies and is incorporated into the impact ejecta. Impact ejecta is classified as either proximal or distal depending if it is located less than or greater than 2.5 crater diameters from the point of impact, respectively (Glass and Simonson, 2012).

Simple craters can retain meteoritic debris and impact melt in the ejecta surrounding the crater (Table 1-1). If the impactor has a metallic composition, the metal may melt during impact and form small metallic spherules which are ejected out of the crater, as was the case with the Barringer crater in Arizona, USA (Blau et al., 1973; Artemieva and Pierazzo, 2011). After impact the liquefied metal droplets cool rapidly as they are ejected and the solid spherules of Fe, Ni, P, and S oxides are dispersed around the crater (Blau et al., 1973). Larger impact events resulting in complex craters can produce glassy melt known as tektites; the minimum diameter for a crater that has produced tektites is 10 km (the Bosumtwi crater in Africa; Howard, 2011). Melt formed in this way is termed tektite if it is >1 cm or microtektite if the size is <1 mm. Tektites are usually spherical but forms generated from rapid rotation create teardrop, dumbbell, and disc shapes (Howard, 2011; Glass and Simonson, 2012). Microtektites and other impact melt are composed mainly of glass which is generated when the target sediment is melted and ejected from the impact site (Howard, 2011). Microtektites usually contain vesicles and sometimes also have relict quartz inclusions in those found within close proximity to their source crater (Glass and Simonson, 2012). These inclusions are the result of unmelted grains becoming incorporated into the melt at the moment of impact. Since microtektites and other impact glasses form during impact they can assist in narrowing down a target location if the melt is transported some distance away from the impact.

Table 1-1: Characteristics and composition from a selection of impact related melt

Impact melt	Size (µm)	Shape	Colour	Primary composition	Magnetic	Reference
ablation spherule						
Sikhote-Alin	0.7 to <10	spherical, ovoid	black	Ni-bearing magnetite, metal	yes	Badyukov and Raitala (2012)
impact spherule						
Kamil	<<1-150	spherical	n/a	Fe-Ni metal and Fe-Ni oxides	yes	D'Orazio et al. (2011)
Canyon Diablo	100-2000	spheroid	n/a	metallic; Fe, Ni, S, P	yes	Blau et al. (1973)
Canyon Diablo	n/a	spherical	n/a	metallic and/or iron oxide	yes	Hodge and Wright (1970)
Sikhote-Alin	n/a	spherical	n/a	metallic and/or iron oxide	yes	Hodge and Wright (1970)
Henbury	~150	spherical	n/a	meteoritic Fe/Ni	yes	Hodge and Wright (1970)
Henbury	~170	spherical	n/a	soil components and Fe	yes	Hodge and Wright (1970)
Boxhole	70-260	spheroid	n/a	FeO, NiO	yes	Hodge and Wright (1973)
microtektite and impact glass						
Australasian	<1000	droplet, dumbbell, spherical, disc	yellow, brown, green, colourless	SiO_2, Al_2O_2, FeO,MgO, K_2O, CaO, Na_2O	no	Cassidy et al. (1969)
Darwin	2000-10000	droplet, spheroid, elongate	white, dark green, black	SiO_2, Al_2O_2, TiO_2, FeO, MgO, CaO, K_2O, Na_2O	no	Howard (2008)

1.4. Younger Dryas carbon spherules

Some impact-generated spherules may not have as obvious an origin as those described above, arguably resulting from an event in which a crater is not formed or preserved. It has been proposed that spherules originated from an airburst or impact about 12900 years ago near the beginning of the Younger Dryas stadial (Firestone et al., 2007). These carbon spherules have been reported as being >75 % carbon, black, highly vesicular, and spherical in shape (Firestone et al., 2007). The mechanism by which these carbon spherules formed is proposed to have been through an intense wildfire that was initiated as a result of this massive event. Twelve indicators, including carbon spherules, were presented as evidence of a major event occurring at this time by Firestone et al. (2007). Several years later the debate regarding the source of these indicators began when they were challenged as being impact related with most explained by naturally occurring terrestrial processes (Scott et al., 2010; Pinter et al., 2011). The leading alternate (non-impact) explanations for the Younger Dryas carbon spherules include fungal sclerotia and termite coprolites (Scott et al., 2010). Fungal sclerotia are hard resistant structures composed of packed filamentous cells (hyphae) for survival and reproduction (Fig. 1-3); sclerotia are black, brown or dark brown in colour, have a smooth surface, have a well differentiated outer and inner layer, and are sometimes hollow (Watanabe et al., 2007; Watanabe, 2010). Some of the biological explanations have some resemblance to the carbon spherules but are not completely identical; even in image comparisons by Scott et al. (2010) similarities between spherules (Fig. 1-3B) and sclerotia (Fig 1-3G,I,J) are limited to general features and not specific details. For the biological explanations to be accepted as the actual origin of these carbon spherules then all components should be observed and present in all the examples of all spherules examined.

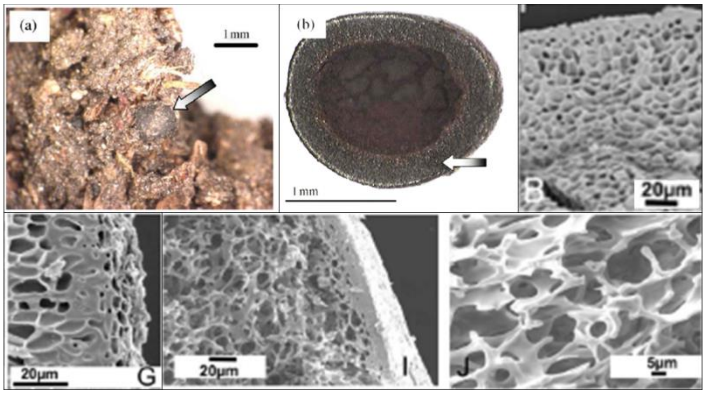

Figure 1-3: Fungal sclerotia. (a) *Cenococcum geophilium* (arrowed) in soil from Japan. (b) Internal hollow structure of *C. geophilium.* [(a-b) from Watanabe et al., 2007] (B) Internal structure of a carbon spherule from a Younger Dryas soil horizon. (I) Broken *Sclerotium rolfsii* showing its thick rind. (J) Fused fungal hyphae of *S. rolfsii*. [(B,G,I,J) from Scott et al., 2010]

The assertion by Firestone et al. (2007) that the Younger Dryas carbon spherules formed during intense wildfires across North America due to a massive impact is the weakness in their explanation. The wildfire origin is well argued against by Scott et al. (2010) and Pinter et al. (2011), casting doubt on this as a credible formation process. Scott et al. (2010) focussed on dismissing the wildfire claim and go as far as to perform their own experiments on fungal sclerotia. Some of the charred sclerotia created by Scott et al. (2010) have features common to the carbon spherules, like size and colour, but are not identical as the hyphae in the sclerotia are not all connected to form rounded pores and the outer rind of the sclerotia have a type of cell distinct from what is observed in its interior. Sclerotia formed by different fungal species are not identical but Scott et al. (2010) compare several species to the carbon spherules; each having slight differences even after charring. Granted they were attempting to disprove the wildfire as the source of their formation but did not consider other formation mechanisms. If the wildfire mechanism can be ruled out then much of the Scott et al. (2010) information regarding the charred sclerotia is no longer comparable to the carbon spherules if there is no reason for them to have been charred in their formation. Detailed chemical compositions of the carbon spherules, fungal sclerotia or termite coprolites are not reported. Knowing these compositions would be a more effective tool for determining the origin of the carbon spherules than by relying on visual similarities or differences alone. More recently Israde-Alcántara et al. (2012) report evidence from Mexico to support the Younger Dryas boundary impact hypothesis, albeit with some variations compared to the initial hypothesis. This new evidence includes a black carbon-rich layer containing carbon spherules, microspherules, and nanodiamonds comparable to Firestone et al.'s (2007) indicators of a major impact or airburst causing the Younger Dryas event but rule out their origin as being wildfire-related. Israde-Alcántara et al.'s (2012) model involves an air shock by a comet or asteroid that generated enough intense thermal radiation at Earth's surface to pyrolyze biomass, generating these indicators which were distributed several seconds later by the air shock and elevated into the upper atmosphere. Once in the upper atmosphere they were transported by prevailing winds and deposited across the Northern and Southern Hemispheres.

In this thesis I carry out a detailed study of the distribution, mineralogy, and petrology of Whitecourt iron meteorites (Chapter 2) and investigate the morphology, internal structure, and composition of amorphous carbonaceous spherules discovered at the impact site (Chapter 3). Together these chapters provide insights into the rarely preserved low-energy impact process that produced the Whitecourt Meteorite Impact Crater less than 1100 years ago.

Bibliography

Artemieva N. and Pierazzo E. 2011. The Canyon Diablo impact event: 2. Projectile fate and target melting upon impact. *Meteoritics & Planetary Science* 46:805-829.

Axon H. J. 1969. Pre-terrestrial deformation effects in iron meteorites. In *Meteorite Research*, edited by Millman P. M. New York: Springer-Verlag New York Inc. pp. 796-805.

Badyukov D. D. and Raitala J. 2012. Ablation spherules in the Sikhote Alin meteorite and their genesis. *Petrology* 20:520-528.

Blau P. J., Axon H. J., and Goldstein J. I. 1973. Investigation of the Canyon Diablo metallic spheroids and their relationship to the breakup of the Canyon Diablo meteorite. *Journal of Geophysical Research* 78:363-374.

Buchwald V. F., 1975. Handbook of iron meteorites. Los Angeles: University of California Press. 1418 p.

Buhl S. and McColl D. 2012. *Henbury craters & meteorites, their discovery, history and study*, 1st ed. Hamburg: Reimer GmbH & Co.KG. 166 p.

Cassidy W. A., Glass B., and Heezen B. C. 1969. Physical and chemical properties of Australasian microtektites. *Journal of Geophysical Research* 74:1008-1025.

Chernogor L. F. and Rozumenko V. T. 2013. The physical effects associated with Chelyabinsk meteorite's passage. *Problems of Atomic Science and Technology* 4:136-139.

D'Orazio M., Folco L., Zeoli A., and Cordier C. 2011. Gebel Kamil: The iron meteorite that formed the Kamil crater (Egypt). *Meteoritics & Planetary Science* 46:1179-1196.

Firestone R. B., West A., Kennett J. P., Becker L., Bunch T. E., Revay Z. S., Schultz P. H., Belgya T., Kennett D. J., Erlandson J. M., Dickenson O. J., Goodyear A. C., Harris R. S., Howard G. A., Kloosterman J. B., Lechler P., Mayewski P. A., Montgomery J., Poreda R., Darrah T., Que Hee S. S., Smith A. R., Stich A., Topping W., Wittke J. H., and Wolbach W. S. 2007. Evidence for an extraterrestrial impact 12,900 years ago that contributed to the megafaunal extinctions and the Younger Dryas cooling. *Proceedings of the National Academy of Science* 104:16016-15021.

Glass B. P. and Simonson B. M. 2012. Distal impact ejecta layers: Spherules and more. *Elements* 8:43-48.

Haack H. and McCoy T. J. 2007. Iron and stony-iron meteorites. In *Treatise on geochemistry, volume 1.12*, edited by Heinrich D. H. and Karl K. T. Oxford, Pergamon, pp.1-22.

Herd C. D. K., Froese D. G., Walton E. L., Kofman R. S., Herd E. P. K., and Duke M. J. M. 2008. Anatomy of a young impact event in central Alberta, Canada: Prospects for the missing Holocene impact record. *Geology* 36:955-958.

Hodge P. W. and Wright F. W. 1970. Meteoritic spherules in the soil surrounding terrestrial impact craters. *Nature* 225:717-718.

Hodge P. W. and Wright F. W. 1973. Particles around Boxhole meteorite crater. *Meteoritics* 8:315-320.

Howard K. T. 2008. Geochemistry of Darwin glass and target rocks from Darwin crater, Tasmania, Australia. *Meteoritics & Planetary Science* 43:479-496.

Howard K. T. 2011. Volatile enhanced dispersal of high velocity impact melts and the origin of tektites. *Proceedings of the Geologists' Association* 122:363-382.

Israde-Alcántara I., Bischoff J. L., Dominguez-Vázquez G., Li H-C., DeCarli P. S., Bunch T. E., Wittke J. H., Weaver J. C., Firestone R. B., West A., Kennett J. P., Mercer C., Xie S., Richman E. K., Kinzie C. R., and Wolbach W. S. 2012. Evidence from central Mexico supporting the Younger Dryas extraterrestrial impact hypothesis. *Proceedings of the National Academy of Science* 109:E738-E747.

Kleine T., Mezger K., Palme H., Scherer E., and Münker C. 2005. Early core formation in asteroids and late accretion of chondrite parent bodies: Evidence from ^{182}Hf-^{182}W in CAIs, metal-rich chondrites, and iron meteorites. *Geochimica et Cosmochimica Acta* 69:5805-5818.

Krinov E. L. 1966. *Giant meteorites*, 1st English ed. New York: Pergamon Press. 39 p.

Krot A. N., Keil K., and Scott E. R. D. 2007. Classification of Meteorites. In *Treatise on geochemistry, volume 1.05*, edited by Heinrich D. H. and Karl K. T. Oxford, Pergamon, pp.1-52.

Munoz C., Guerra N., Martinez-Frias J., Lunar R., and Cerda J. 2007. The Atacama Desert: A preferential arid region for the recovery of meteorites – Find location features and strewnfield distribution patterns. *Journal of Arid Environments* 71:188-200.

Norton O. R. 2002. *The Cambridge encyclopedia of meteorites*, 1st ed. Cambridge: Cambridge University Press. 354 p.

Pinter N., Scott A. C., Daulton T. L., Podoll A., Koeberl C., Anderson R. S., and Ishman S. E. 2011. The Younger Dryas impact hypothesis: A requiem. *Earth-Science Reviews* 106:247-264.

Roddy D. J., Shoemaker E. M., Shoemaker C. S., and Roddy J. K. 1988. Aerial photography and geologic studies of impact structures in Australia (abstract #1501). 19th Lunar and Planetary Science Conference.

Scott A. C., Pinter N., Collinson M. E., Hardiman M., Anderson R. S., Brain A. P. R., Smith S. Y., Marone F., and Stampanoni M. 2010. Fungus, not comet or catastrophe, accounts for carbonaceous spherules in the Younger Dryas "impact layer". *Geophysical Research Letters* 37: L14302, doi: 10.1029/2010GL043345.

Scott E. R. D. and Wasson J. T. 1975. Classification and properties of iron meteorites. *Reviews of Geophysics and Space Physics* 13:527-546.

Szurgot M., Rozniakowski K., Wojtatowicz T. W., and Polanski K. 2008. Investigation of microstructure and thermophysical properties of Morasko iron meteorites. *Crystal Research and Technology* 43:921-930.

Uhlig H. H. 1954. Contribution of metallurgy to the origin of meteorites Part I: Structure of metallic meteorites, their composition and the effect of pressure. *Geochimica et Cosmochimica Acta* 6:282-301.

Watanabe M., Inoue Y., Sakagami N., Bolormaa O., Kawasaki K., Hiradate S., Fujitake N., and Ohta H. 2007. Characterization of major and trace elements in sclerotium grains. *European Journal of Soil Science* 58:786-793.

Watanabe T. 2010. *Pictorial atlas of soil and seed fungi*, 3rd ed. Boca Raton: CRC Press. 404 p.

CHAPTER 2: Distribution, mineralogy, and petrology of Whitecourt iron meteorites

2.1. Introduction

The Whitecourt Meteorite Impact Crater (WMIC) was discovered in 2007 and since then further information has been collected, expanding the knowledge of this site and the impact event that it represents. Work by Kofman et al. (2010) on the 36 m diameter simple crater estimates that the iron impactor was traveling in an east-northeast direction with a velocity of 10 km s^{-1} or less before it impacted Earth at an angle between 40° and 55°. The incoming meter-sized body has an estimated mass around 5.6×10^3 kg (Herd et al., 2008). The iron impactor was a relatively common IIIAB medium octahedrite (Herd et al., 2008). Factors that contribute to the significance of the WMIC include its high state of preservation, the small size and young age of the crater, and the presence of meteorites and their abundance. Documented meteorite finds associated with this site total over 4700 with a total mass of over 227 kg. Of the 183 known terrestrial craters, less than 20 also have meteorites that survived the effects of the impact event (Earth Impact Database; University of New Brunswick, 2013). With a terrestrial age of <1100 years, based on radiocarbon dates obtained from charcoal found in the paleosol beneath the ejecta layer (Herd et al., 2008), the impact postdates any glacial activity which would have modified the crater and re-distributed the meteorite fragments. A counterexample is the distribution of the Muonionalusta iron meteorites in Sweden that have a terrestrial age of >800000 years, during which the meteorites were re-distributed and buried by at least two glaciations, obliterating the original strewnfield (Wickman, 1970).

The small diameter of the Whitecourt crater corresponds to a smaller impacting mass and lower amount of energy produced at the time of impact, compared to other simple craters with a diameter in the km size range, such as Barringer crater in Arizona, USA. Reduced energy would cause less impactor vaporization resulting in the preservation of some of the original material. However, only about 4% of the estimated initial mass of the WMIC impactor survived the impact, based on the current totals of recovered shrapnel fragments and the absence of a large buried mass below the crater fill (Kofman et al., 2010). These fragments are identical in composition to the original body with the only changes due to physical effects from the explosion of the impactor during impact. The pieces that most resemble the pre-atmospheric meteoroid are the recovered regmaglypted individuals that spalled off the main body during atmospheric transit. These were not modified during the crater-forming event and therefore best represent the state of the meteoroid before its collision with Earth. Previously discovered features, such as a single metallic spherule recovered from the crater fill at the base of the transient crater boundary as well as quartz grains with planar microstructures and meteorite dust, support a low energy, albeit hypervelocity event (Kofman et al., 2010).

2.2. Methods

Field work was directed at recovering meteorite fragments located near the crater, with permission from Alberta Historic Resources, to improve the distribution of meteorites in this protected area. Meteorites were located using metal detectors and their position marked using handheld GPS devices as well as noting their recovery depth when possible. In the lab the external surfaces of meteorites were gently scrubbed in deionized water to remove excess dirt or debris followed by an acetone wash. The weight of each meteorite was measured and the external surface was examined using a stereo microscope, making note of morphological surface features of the fragments.

Meteorites were cut using a Buehler Isomet low speed saw and a 12.7 cm x 0.0381 cm wafering blade and deionized water was used as lubricant. Once the first piece of a fragment was cut for samples to be examined for scanning electron microscope (SEM) analysis a second parallel cut was made to the opposite side, making a flat mounting surface. Cut faces were polished by hand using wet to dry sandpaper and finished by using a grinding wheel with alumina suspended fluids. Small pieces were mounted in 1" epoxy plugs before polishing. Some meteorite samples were then etched using nitol. Some polished meteorites were not carbon coated because they were already conductive by nature while all epoxy-mounted meteorites required a carbon coating for further analyses.

A Zeiss EVO MA 15 SEM was used to obtain backscattered and secondary electron images and EDS (energy dispersive spectrometry) analysis provided semi-quantitative elemental data for determining the composition of minerals present in the meteorites. The chemical composition of several meteorites was also determined using quantitative measurement with a JEOL 8900 electron probe microanalyzer (EPMA) using wavelength dispersive spectrometry (WDS). Analytical conditions for all minerals, except carlsbergite, operated with an accelerating voltage of 20 kV and a 20 nA probe current. The analyzed elements, with standards, were Ti (rutile), P (apatite), S (FeS_2), Fe (hematite), Cr (chromite), Ni (Ni wire CB1), Co (Co metal), Cu (chalcopyrite), and Zn (gahnite). For carlsbergite analyses, the accelerating voltage was 20 kV, probe current was 20 nA, and the analyzed elements and standards were N (boron nitride), Cr (Cr_2O_3 CB1), Fe (hematite), Ni (Ni wire CB1), Co (Co metal), and Zn (gahnite).

2.3. Results

2.3.1. Distribution

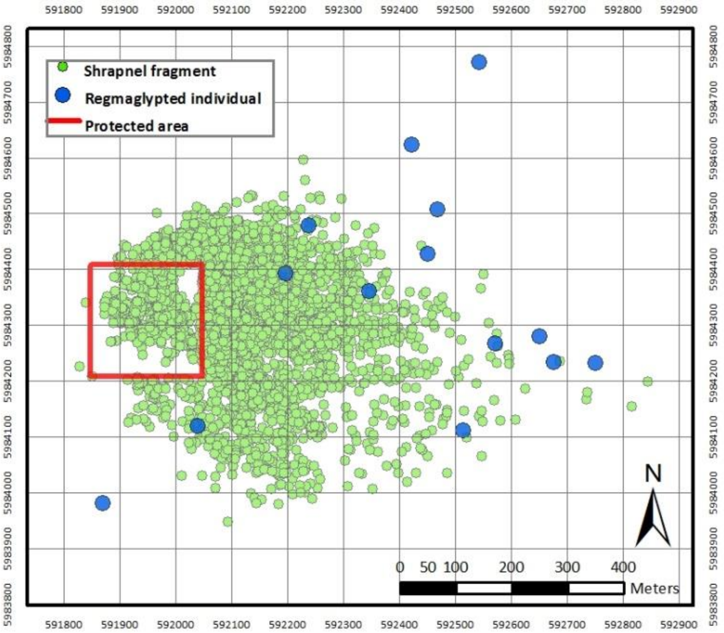

Figure 2-1: Map showing the locations of reported Whitecourt meteorite finds; the impact crater is located at the center of the protected area and grid spacing is 100 m.

There are two overlapping but distinct distributions of Whitecourt meteorites: one for the shrapnel-shaped fragments and another for the regmaglypted individuals (Fig. 2-1). Over 4700 shrapnel fragments have been documented and range in weight from <1 g to 1899 g. The majority of the fragments are at the small end of the range with 95% of documented pieces having a weight <100 g. The shrapnel-shaped fragments form an elliptical area east of the crater (Fig. 2-2). The majority of reported fragments are from outside the protected area and represent more thorough recovery efforts with few gaps in distribution despite some finds not being reported. Small gaps in meteorite distribution within the main ellipse correspond with ephemeral streams or marshy areas where searching is impractical. The two most distal fragments known were found about 900 m east of the crater with weights of 277.5 g and 128.6 g. The concentration of meteorites is highest along the eastern outside edge of the protected area and decreases as the distance away from the crater increases. Very few fragments have been found west of the crater and once outside the protected area (~100 m away) the number drops

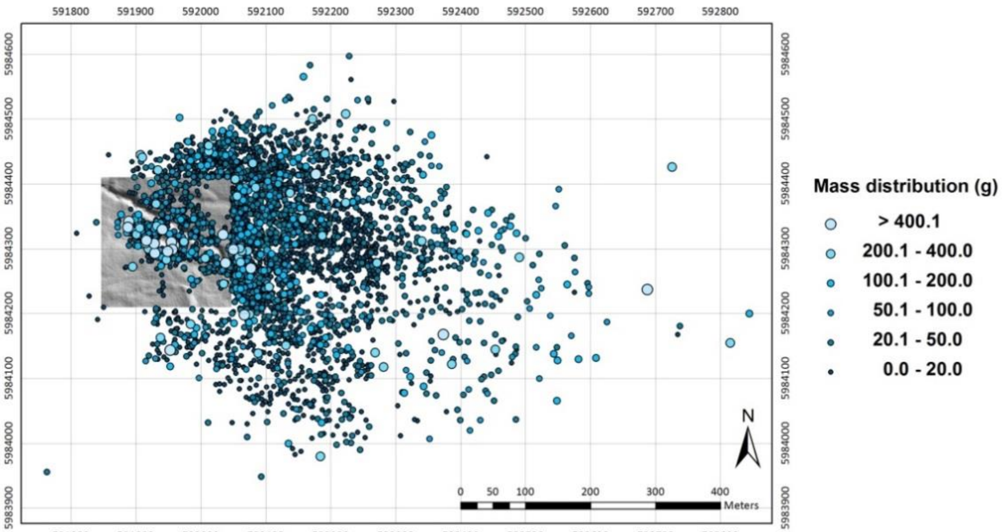

Figure 2-2: Shrapnel fragment mass distribution map. Protected zone is designated by the LiDAR image with the crater located at the center of this 200 x 200 m area. Grid spacing is 100 m.

to less than 10 pieces. Depth of meteorite recovery was recorded for over half of the samples on record (over 2600 samples). The depth at which shrapnel fragments are recovered range from surface to 25 cm below the surface, which accounts for 95% of the fragments found. The most common depth a meteorite was recovered from was 10 cm. Of the 5% of shrapnel fragments deeper than 25 cm the deepest recovered fragment was found at 46 cm.

The second and less defined distribution is that of the regmaglypted individuals (RIs). There are only 14 documented RIs; however, this group contains the largest recovered samples by weight, accounting for 47% of the current known weight of all meteorites (Fig. 2-3). RIs range in weight from 56 g to 31.5 kg. The longest axis in the distribution of these 14 pieces show a SW-NE trend which is about 1 km long and less than 600 m wide, and increases to just over 800 m wide when the ~1 m diameter crater-forming impactor is included as a member of this group. All but four RIs have been recovered within the shrapnel distribution. The recovery depth is known for 11 RIs and ranges from 8 cm to 61 cm.

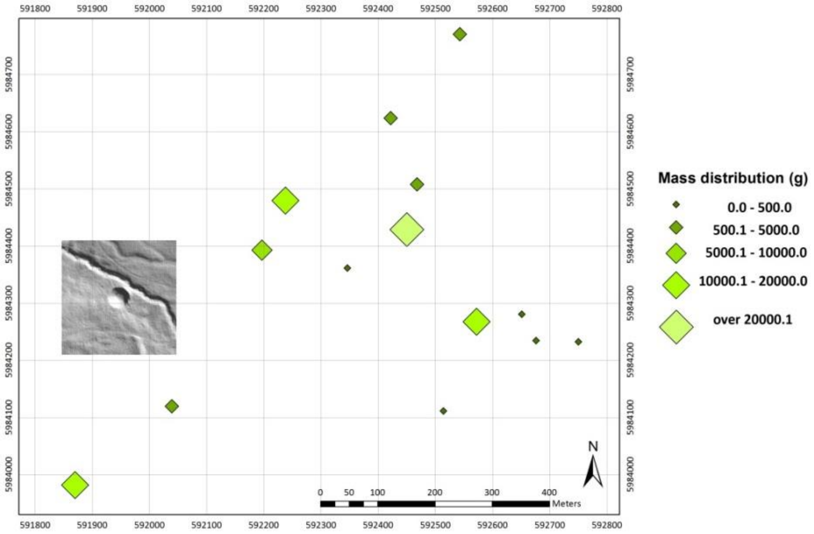

Figure 2-3: Regmaglypted individual mass distribution map. Protected zone is designated by the LiDAR image with the crater located at the center of this 200 x 200 m area. Grid spacing is 100 m.

2.3.2. Morphology and texture

Shrapnel-shaped Whitecourt fragments primarily have sharp angular edges, often curled, with relatively smooth convex surfaces (Fig. 2-4). Less common are fragments with very flat faces, where these faces are oriented in an octahedral arrangement. Octahedral structure is observed in many samples but is not always well-defined as edges have been deformed (Fig. 2-5). Smaller scale surface features such as ridges, grooves, or deformations are visible on samples

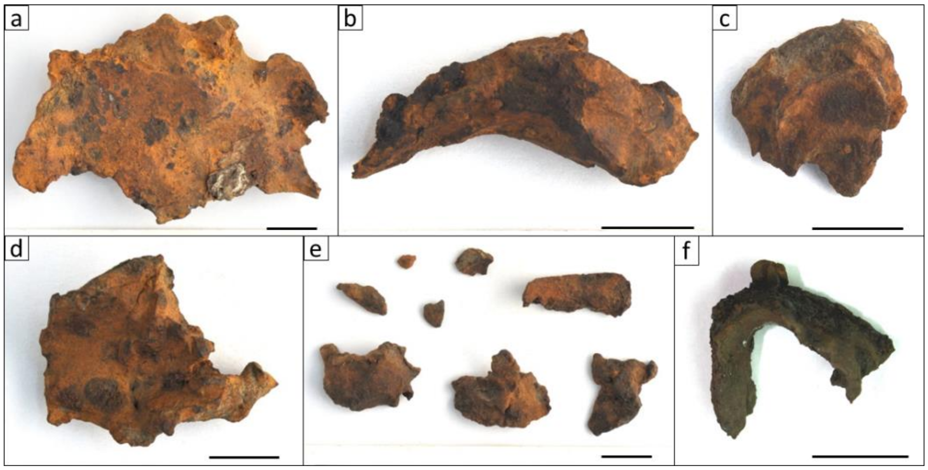

Figure 2-4: Shrapnel fragment morphologies. (a) Angular edges with smoother and slightly concave interior surface. (b) Fragment with a highly concave morphology. (c) Small fragment with top side displaying deformation on external surface. (d) Angular concave fragment with a vertical groove running through the middle. (e) Small fragments show angular and rounded edges and surfaces. (f) U-shaped fragment shows high degree of deformation. [scale bars = 1 cm]

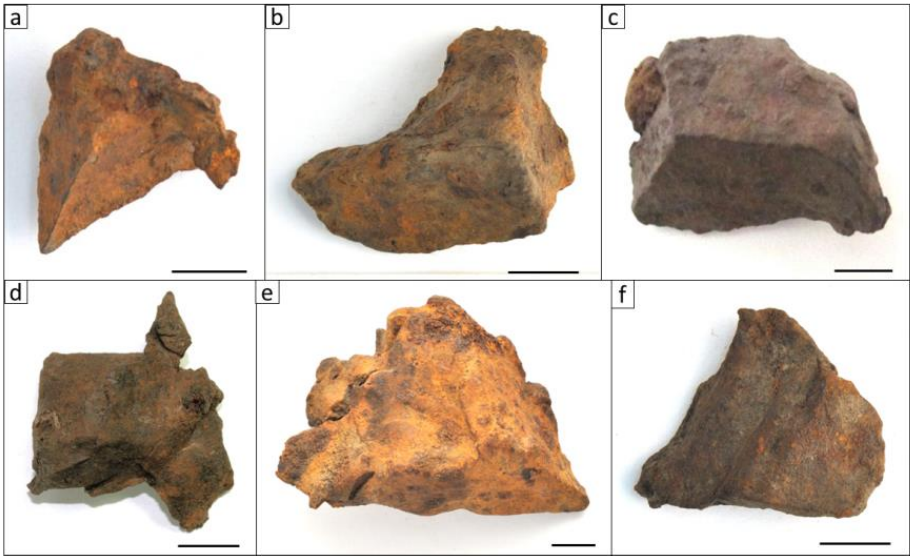

Figure 2-5: Shrapnel fragments displaying varying degrees of octahedral structure. (a) Fragment shows a sharp, well-defined octahedral edge with flat faces as well as backside having more angular and deformed edges. (b) Fragment has more rounded edges but still retains underlying octahedral angles with low deformation. (c) Strong display of octahedral structure throughout fragment with slight deformation at the right end. (d) Two edges are straight while rest of fragment shows typical shrapnel characteristics. (e) Larger fragment with octahedral features at one corner with faces becoming much more angular. (f) Fragment with "steps" corresponding to the same octahedral angle at each rise. [scale bars = 1 cm]

with low degrees of weathering. Weathered surfaces are rusty in appearance but the extent and depth of weathering varies between samples. Other variations in shrapnel morphology include very thin fragments, thicker blocky pieces, and some that have more rounded edges.

Individuals are characterized as having thumbprint-like depressions present on most surfaces called regmaglypts (Buchwald, 1975). The regmaglypts are rounded depressions but can also be more angular, especially when edges are angular and blocky (Fig. 2-6). The size of the

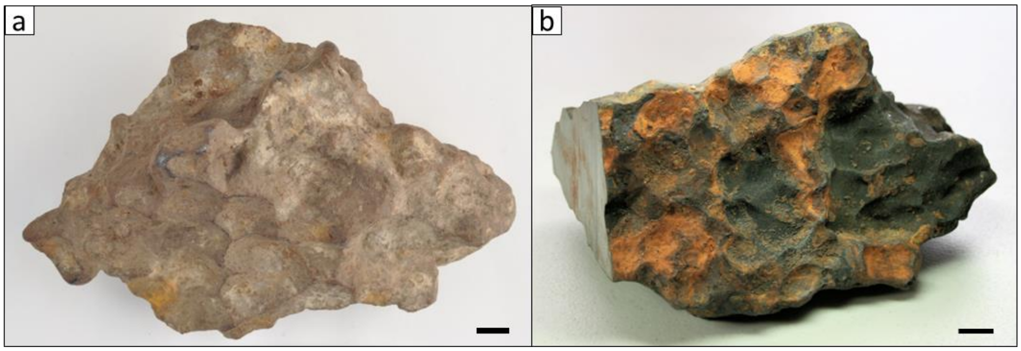

Figure 2-6: Individuals with regmaglypted external surfaces. (a) 1177.6 g individual with well-defined regmaglypts 1-3 cm in diameter (b) 6510.0 g (mass before cut) individual with angular regmaglypts 1-3 cm in diameter and a higher degree of terrestrial weathering. [scale bars = 1 cm]

regmaglypts also varies where the larger individuals have larger depressions and the small pieces have small well-defined regmaglypts. Regmaglypts are absent from shrapnel pieces. Regmaglypted individuals (RIs) retain some of the octahedral angles that are observed in the shrapnel fragments; however, faces are not flat but are masked by the regmaglypts. The degree to which the octahedral structure remains corresponds to how angular or rounded the RI is.

The internal structure of both meteorite types was examined by looking at etched samples. Shrapnel fragments show some deformation in the Widmanstätten pattern (Fig. 2-7), previously described by Herd et al. (2008) and Kofman et al. (2010). Deformation of the pattern

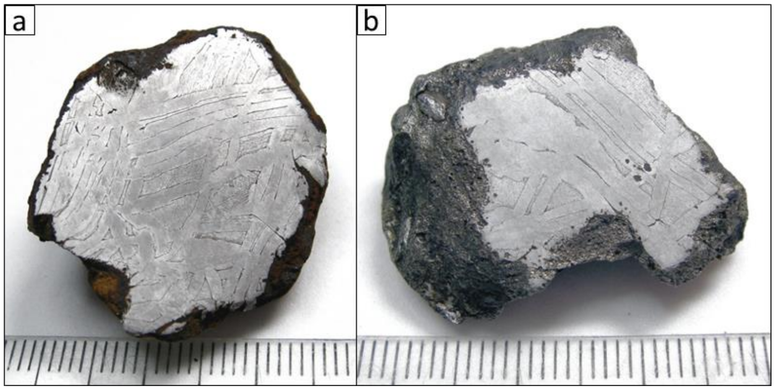

Figure 2-7: Nitol-etched shrapnel fragments. (a) Slight deformation of Widmanstätten pattern throughout fragment, greater near edges. (b) Deformation as well as some recrystallized kamacite.
[scale divisions = 1 mm]

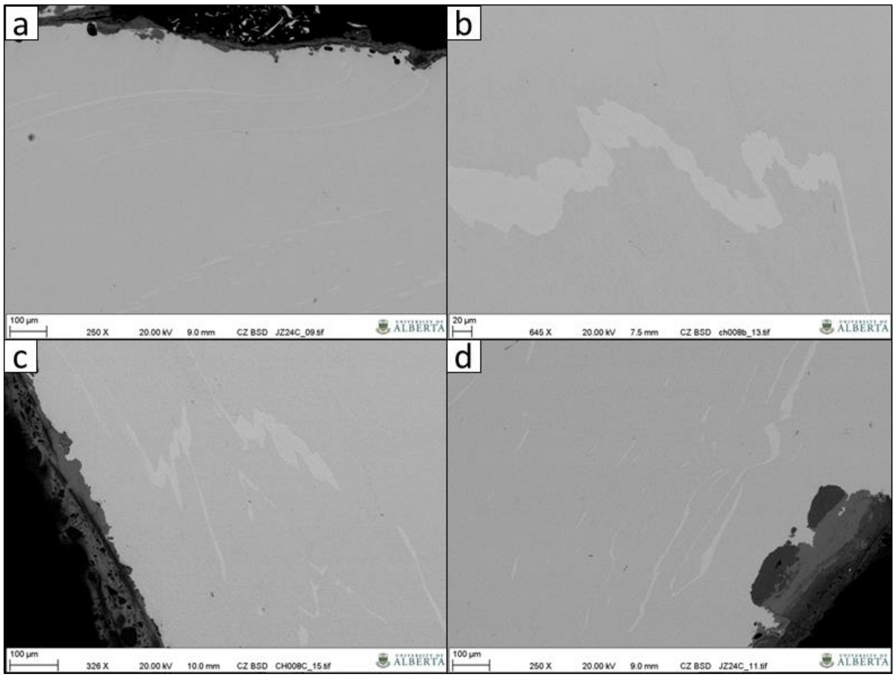

Figure 2-8: Internal deformation of shrapnel by examining taenite lamellae (light grey) within kamacite (grey) and darker colours near black edge is terrestrial weathering. (a) Large scale and matching deformation along the outer edge of fragment. (b) Shear deformation and compression of taenite. (c) Shear deformation of a group of taenite lamellae near the edge of a fragment. (d) Less disrupted taenite lamellae with only a small area showing shearing. All are BSE images of polished unetched surfaces.

is present at both the macro and micro scale as shown with SEM backscattered and secondary electron imagery (Fig. 2-8, Fig. 2-9). At the macro scale the Widmanstätten pattern is easily seen and varies from straight parallel lamellae to curved and distorted lamellae; these variations often mimic the external morphology (Fig. 2-8a, Fig. 2-9a). Shrapnel pieces frequently have distortions to the Widmanstätten pattern along edges, where curved edges often correspond to a similarly curved lamellae and straight portions to flat external faces. Shear deformations and compression of taenite lamellae are more prevalent near the edges of shrapnel fragments. Distortions may simply be a change in direction of the lamellae or in more extreme cases show recrystallization and merging of adjacent lamellae. At the micro scale distortions of lamellae appear as minute dislocations. These are observed along the outer edge of taenite lamellae of etched samples using secondary electron imaging.

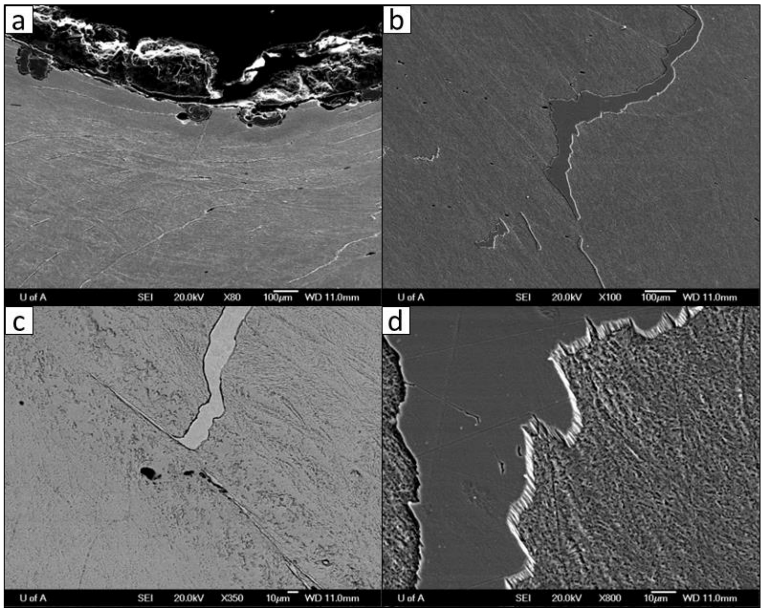

Figure 2-9: Internal deformation of shrapnel by examining taenite lamellae (light grey) in BSE images (a and c) and darker grey taenite lamellae in SE images (b and d). (a) Deformation along edge mimics the contour of the external surface. (b) Deformation of taenite. (c) Shear deformation truncating a taenite lamella. (d) Higher magnification image of b) showing minute dislocations along lamella. All surfaces have been nitol-etched.

A slice from a 6.5 kg recovered RI was etched and its Widmanstätten pattern was examined (Fig. 2-10). The macro scale reveals straight parallel lamellae throughout the slice with no curving or distortion of lamellae along external edges. The RI slice contains several thicker recrystallized kamacite lamellae in localized areas on the right side of the slice but remain parallel to the rest of the kamacite lamellae. At the micro scale the lamellae are free of the minute dislocations observed in some distorted taenite lamellae in shrapnel fragments. Several areas along the edge of the RI slices show a recrystallized heat alteration zone (Fig. 2-10b). A heat alteration zone was not observed in any of the shrapnel fragments examined by SEM.

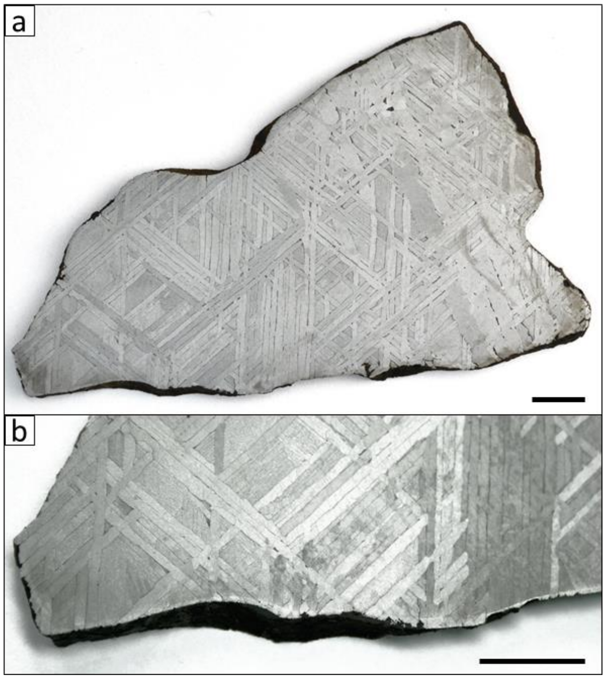

Figure 2-10: Nitol-etched slice from a regmaglypted individual. (a) Slice displaying interior Widmanstätten pattern. (b) Magnified image of lower left corner of slice showing a narrow heat alteration zone (bright area along bottom edge of slice) not destroyed by terrestrial weathering. [scale bars = 1 cm]

2.3.3. Composition

Whitecourt meteorites are type IIIAB iron meteorites and are composed primarily of two iron alloys, the nickel-poor kamacite, α-(Fe,Ni), and nickel-rich taenite, γ-(Fe,Ni). Kamacite is the most common metallic component of the Whitecourt meteorites having an average Fe content of 92.1 ± 0.4 wt% and average Ni content of 7.1 ± 0.3 wt% (Table 2-1). Taenite has a slightly wider Ni range of 31.3 ± 1.8 wt% and Fe content of 68.0 ± 1.8 wt% (Table 2-1). Small isolated areas 1-10 µm in size with a Ni content around 50 wt% are found as grain boundary precipitates around some accessory mineral inclusions. A third metallic component, plessite, is also present (Fig. 2-11). Plessite has an intermediate composition between kamacite and taenite as it is a mixture of the low and high Ni phases. Plessite can develop many different forms, of which two are observed in the meteorites examined and include net and comb (Buchwald, 1975). These forms are best observed in nitol-etched samples where the relief between phases is easily recognized. Some wider wedge-shaped taenite lamellae exhibit a martensitic texture (Fig. 2-11e), also best observed after etching, which forms by decomposition of the Ni-rich alloy. The pattern of the martensitic texture mimics the orientation of the bulk Widmanstätten pattern (Buchwald, 1975; Bartoschewitz and Spettel, 2001). Unetched kamacite is relatively featureless and is interspersed by thin taenite lamellae and larger plessitic areas associated with the underlying Widmanstätten structure.

Table 2-1: Mineral compositions in the Whitecourt meteorite determined by electron probe microanalysis (EPMA)

	n	Fe (wt%)	Ni (wt%)	S (wt%)	Cr (wt%)	P (wt%)	Cu (wt%)	Zn (wt%)	Co (wt%)	Ti (wt%)	N (wt%)	total (wt%)
Major minerals												
kamacite	12	92.1 ± 0.4[1]	7.1 ± 0.3	0.0 ± 0.1	0.2 ± 0.4	0.1 ± 0.0	0.0 ± 0.0	0.0 ± 0.0	0.4 ± 0.0	0.0 ± 0.0	n.d.[2]	98.6 to 100.8
taenite	13	68.0 ± 1.8	31.3 ± 1.8	0.0 ± 0.0	0.0 ± 0.0	0.0 ± 0.0	0.0 ± 0.0	0.0 ± 0.0	0.0 ± 0.0	0.0 ± 0.0	n.d.	98.6 to 99.8
plessite	3	78.3 ± 3.3	21.3 ± 3.4	0.0 ± 0.0	0.0 ± 0.0	0.0 ± 0.0	0.0 ± 0.0	0.0 ± 0.0	0.1 ± 0.1	0.0 ± 0.0	n.d.	99.6 to 99.8
Accessory minerals												
troilite	10	61.9 ± 2.3	0.1 ± 0.1	37.2 ± 0.6	1.0 ± 1.8	0.0 ± 0.0	0.2 ± 0.1	0.0 ± 0.0	0.0 ± 0.0	0.0 ± 0.0	n.d.	99.3 to 101.4
daubréelite	18	20.0 ± 0.8	0.1 ± 0.2	43.9 ± 0.1	35.8 ± 0.7	0.0 ± 0.0	0.3 ± 0.1	0.1 ± 0.1	0.0 ± 0.0	0.0 ± 0.0	n.d.	98.3 to 101.0
zincian daubréelite	7	18.2 ± 0.9	0.1 ± 0.1	44.1 ± 0.7	35.3 ± 0.4	0.0 ± 0.0	0.2 ± 0.0	2.3 ± 0.7	0.0 ± 0.0	0.0 ± 0.0	n.d.	99.7 to 101.2
high Fe daubréelite	4	30.0 ± 3.4	0.8 ± 0.9	38.8 ± 2.2	27.4 ± 2.8	0.0 ± 0.0	0.6 ± 0.6	0.8 ± 1.2	0.0 ± 0.0	0.0 ± 0.0	n.d.	97.2 to 100.3
schreibersite	5	44.1 ± 0.4	40.2 ± 0.2	0.1 ± 0.0	0.6 ± 0.1	12.6 ± 0.3	0.0 ± 0.0	0.0 ± 0.0	0.0 ± 0.0	0.0 ± 0.0	n.d.	95.5 to 96.6
nickelphosphide	4	37.4 ± 0.7	46.6 ± 0.5	0.1 ± 0.0	0.0 ± 0.0	12.2 ± 0.4	0.0 ± 0.0	0.0 ± 0.0	0.0 ± 0.0	0.0 ± 0.0	n.d.	97.3 to 97.9
carlsbergite	5	2.0 ± 0.7	0.1 ± 0.0	n.d.	76.7 ± 0.8	n.d.	n.d.	0.0 ± 0.0	0.0 ± 0.0	n.d.	19.8 ± 0.5	98.0 to 99.3
copper	1	5.6	1.6	2.1	1.0	0.0	93.4	0.0	0.0	0.0	n.d.	103.6

[1] Average of n analyses with standard deviation provided

[2] n.d. = not determined

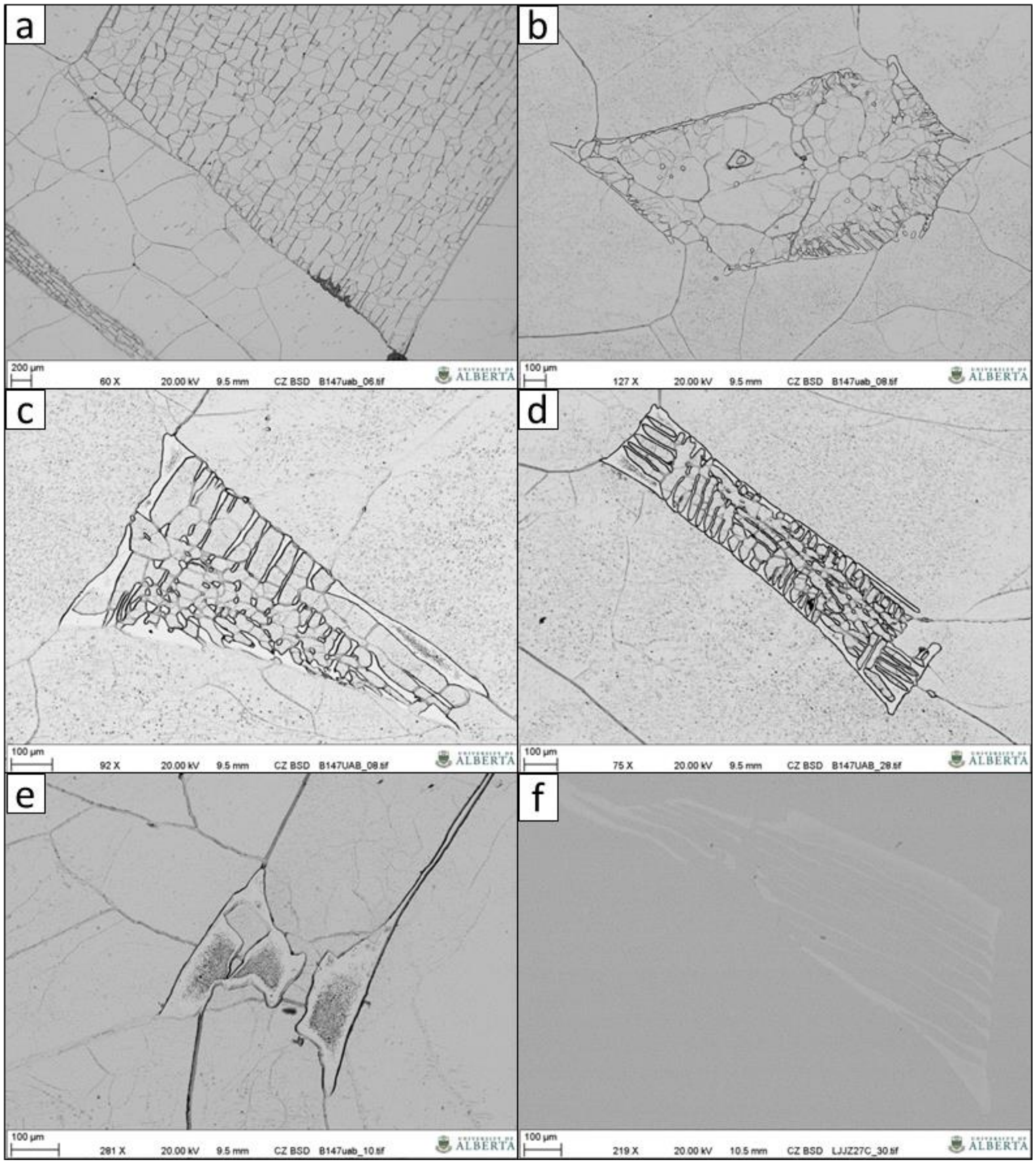

Figure 2-11: Plessite types. (a) Well-developed large net plessite field. (b) Net plessite which is slightly degenerated in the center of the field. (c) Plessite field displays net plessite form along the bottom transitioning to comb plessite in the upper half; slightly degenerated. (d) Dominant plessite form is comb with minor net areas. (e) Martensitic texture (darker areas) present in the center of these wider taenite lamellae. (f) Partially degenerated comb plessite. All are BSE images with nitol-etched surfaces except for f), which is unetched.

Along the outermost edge of 2-3 mm thick slices of the 6.5 kg regmaglypted individual there are sections where the terrestrial weathering has not penetrated deep enough into the meteorite to have completely removed the entire heat-affected zone (Fig. 2-10). The heat affected zone has been found up to 1 mm wide. These recrystallized areas are absent in all examined shrapnel fragments, and are only visible in etched samples. The SEM images of the etched RI slice in Figure 2-12 show the subtle transition between the original and recrystallized metal along the edge of the sample.

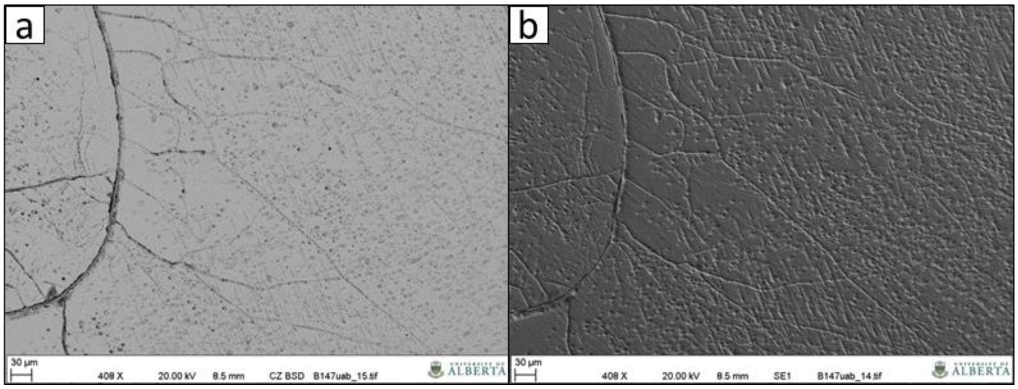

Figure 2-12: Partially recrystallized kamacite located in the heat alteration zone (right half of image) of nitol-etched surface. Short parallel dendrites oriented NNW to SSE are visible in (a) BSE image and in (b) SE image of the same area.

Non-metallic accessory minerals present in the Whitecourt meteorites examined include daubréelite, troilite, iron-nickel phosphides, chromite, and carlsbergite. Small grains of native copper are also found. Most accessory mineral inclusions are spherical or rounded in shape but in rare cases euhedral forms are present (Fig. 2-13).

The sulfides daubréelite ($FeCr_2S_4$) and troilite (FeS) are the most common of the accessory minerals. They are present in inclusions showing clear parallel exsolution lamellae (Fig. 2-13c,e,g), as single composition grains (Fig. 2-13d), or as an intermediate of these (Fig. 2-13a,b,h). Troilite forms the largest inclusions observed; these inclusions range in size from 910 to 3400 µm. Daubréelite inclusions are smaller in size (33 to 248 µm) but are more numerous. In some daubréelite inclusions the substitution of Fe by Zn up to 2.3 ± 0.7 wt% and Cu up to 0.6 ± 0.6 wt% was detected whereas in troilite the only substitution detected for Fe was by Cu with a value of 0.2 ± 0.1 wt% (Table 2-1). The troilite component in these sulfides show minute fractures which are absent in daubréelite. These small fractures are commonly observed with exsolution lamellae where these fractures form perpendicular to the alternating troilite and daubréelite lamellae (Fig. 13e,f).

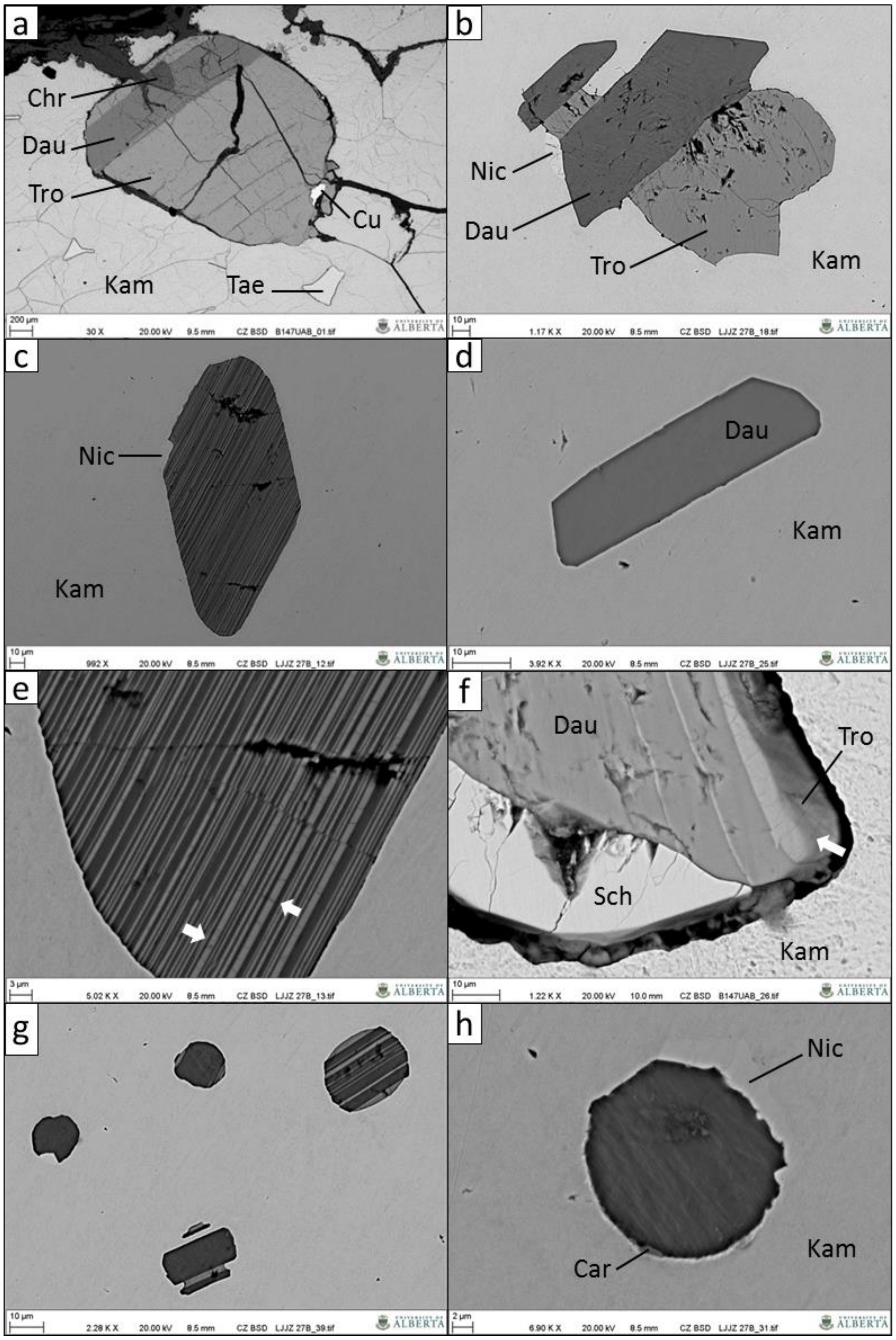

Figure 2-13: Sulfide mineralogy. (a) Large sulfide inclusion located near the edge of sample so some weathering is present (darker areas near top of image). Mineral phases present include chromite (Chr), daubréelite (Dau), troilite (Tro), kamacite (Kam), taenite (Tae), and copper (Cu). (b) Wide bands of daubréelite and troilite are present in this sulfide as well as a grain boundary precipitate of nickelphosphide (Nic). (c) Euhedral sulfide inclusion showing fine parallel exsolution lamellae of troilite (light lamellae) and daubréelite (dark lamellae) with a small grain boundary precipitate of nickelphosphide. (d) Inclusion presents a single mineral phase (daubréelite). (e) Higher magnified image of c) displaying exsolution of troilite (light lamellae) and daubréelite (dark lamellae). Thermal fractures within troilite are visible perpendicular to lamellae orientation (white arrows) and at center right of inclusion a shock fracture has slightly offset some lamellae. (f) Etching reveals thermal fractures (indicated by white arrow) within troilite are continuous and extend through the lamellae of this sulfide and schreibersite (Sch) inclusion. (g) Cluster of small sulfides showing orientation of exsolution lamellae is not uniform throughout a sample; dark mineral phase is daubréelite and lighter lamellae are troilite. (h) A daubréelite inclusion associated with nickelphosphide and small grain boundary precipitates of carlsbergite (Car). All have polished unetched surfaces except a) and f) which are nitol-etched; all BSE images.

Iron-nickel phosphides are also common. The two minerals in this group are very similar with the only distinction being the amount of nickel present; nickel-poor schreibersite ($(Fe, Ni)_3P$) and nickel-rich nickelphosphide ($(Ni, Fe)_3P$). These phosphides are present as grain boundary precipitates with sizes ranging from 23 to 280 µm (Fig. 2-14); grain boundary precipitates are found along the outside edge of a larger sulfide inclusion. Only one phosphide was found that was not a grain boundary precipitate, which was a 100 µm schreibersite grain near the center of a net plessite region (Fig. 2-11b).

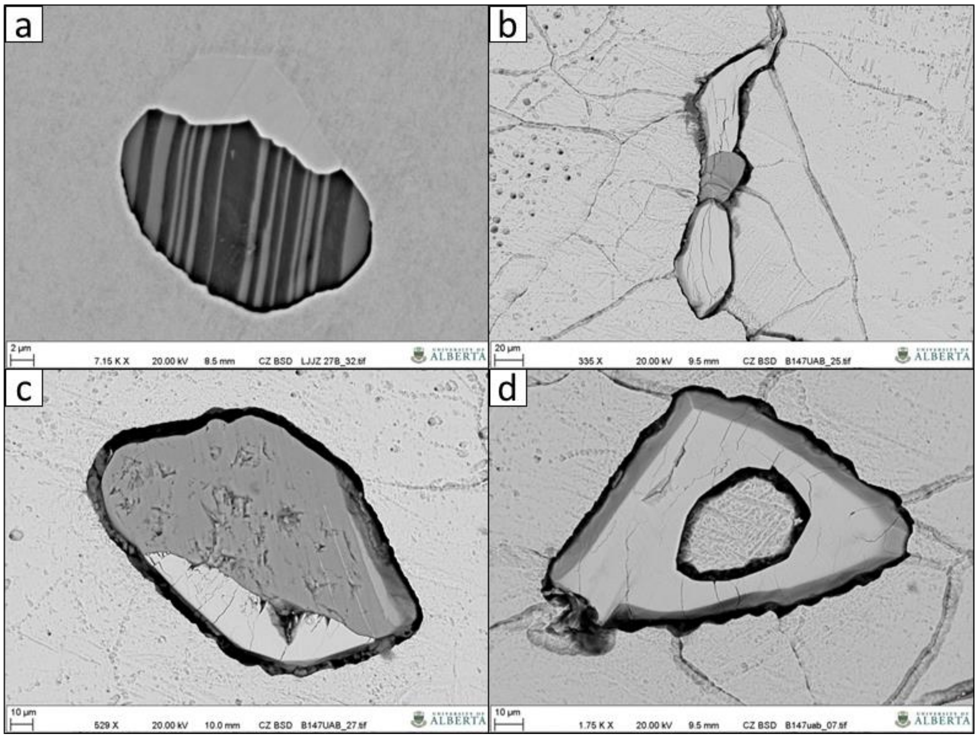

Figure 2-14: Phosphide mineralogy. (a) Grain boundary schreibersite (light grey) on top edge of a sulfide (grey troilite and darker grey daubréelite) showing clear exsolution. (b) Small daubréelite inclusion surrounded by dual elongated schreibersites. (c) Larger daubréelite inclusion with narrow troilite exsolution lamellae and large grain boundary schreibersite (white) at bottom. (d) Triangular schreibersite with central kamacite is located within the net plessite region shown in Figure 2-11b. All are BSE images; a) has a polished unetched surface and b-d) are nitol-etched.

The least common accessory minerals found are chromite ($FeCr_2O_4$) and carlsbergite (CrN). Chromite is usually found associated with large troilite-daubréelite inclusions (Fig. 2-13a, Fig. 2-15a) and range in size from 220 to 480 µm. Only one isolated chromite grain was found, with a size of 176 µm (Fig. 2-15b). Chromite inclusions have a nearly pure composition with occasional Zn substitution, as determined by SEM (Table 2-2). Compositional analysis for chromite was only obtained by SEM because the samples prepped for EPMA did not contain chromite; the same samples could not be used for both machines due to the way the samples were prepared. Carlsbergite is usually found as <1 to 2 µm grain boundary precipitates around daubréelite inclusions (Fig. 2-13h, Fig. 2-15e,f). Carlsbergite grains are slightly larger in size when they are isolated inclusions, ranging from 8 to 17 µm. Isolated inclusions have more of a subhedral shape, showing some cubic elements but lacking a perfect cubic mineral shape (Fig. 2-15c,d).

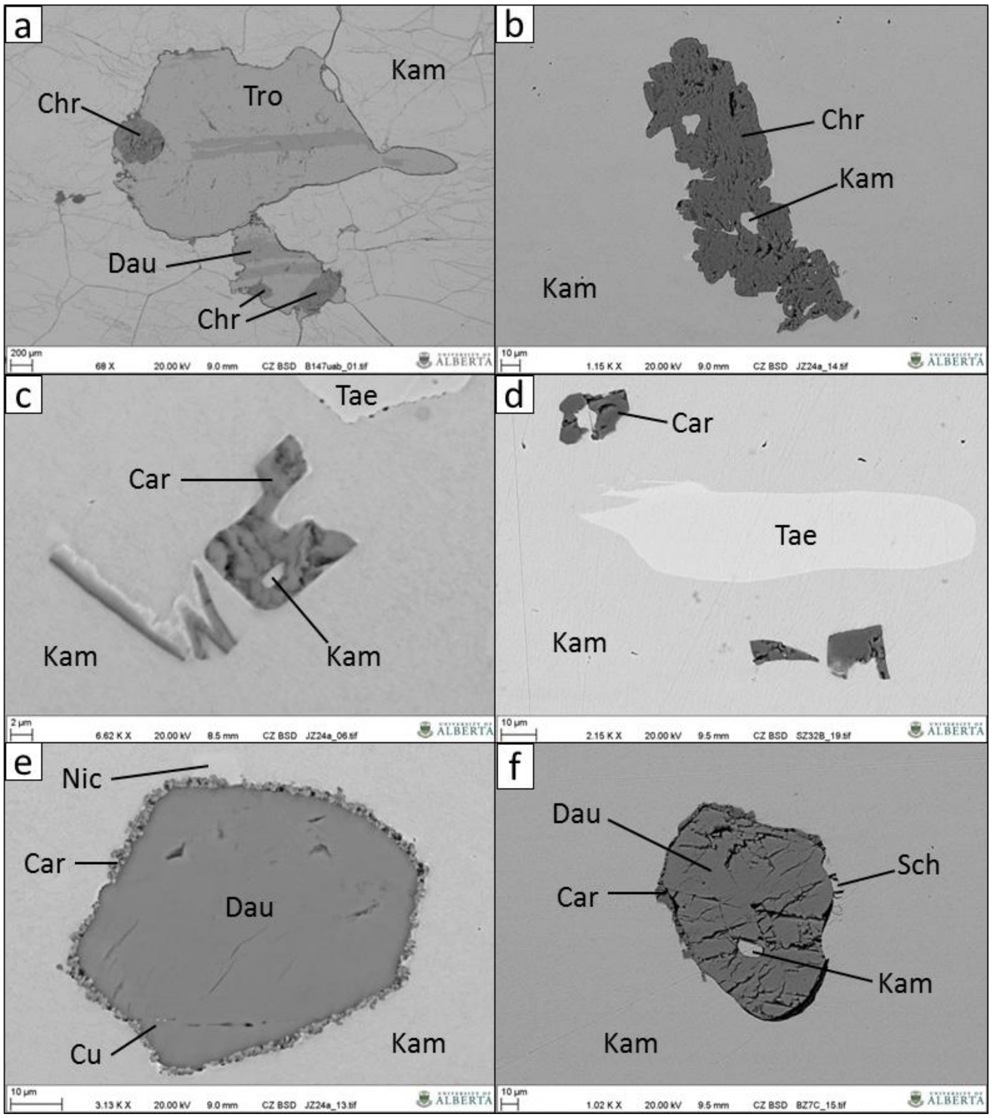

Figure 2-15: Chromium bearing minerals. (a) Three rounded chromite grains within a large sulfide inclusion; mineral phases include chromite (Chr), daubréelite (Dau), troilite (Tro), and kamacite (Kam). (b) Only chromite occurrence not associated with sulfides. Light-coloured kamacite phase occurs within chromite inclusion as well as surrounding it. (c) Subhedral carlsbergite (Car) inclusions located near a taenite (Tae) lamella. (d) Three small carlsbergite inclusions. (e) Small grain boundary precipitates of carlsbergite surrounding the chromium-sulfide daubréelite; other mineral phases present include nickelphosphide (Nic) and two tiny copper (Cu) grains. (f) Daubréelite with grain boundary precipitates of carlsbergite and schreibersite (Sch). All are BSE images; a) has been nitol-etched and b-f) are polished and unetched.

Table 2-2: Mineral compositions in the Whitecourt meteorite determined by scanning electron microscopy (SEM)

		n	Fe (wt%)	Ni (wt%)	S (wt%)	Cr (wt%)	P (wt%)	O (wt%)	N (wt%)	Cu (wt%)	Zn (wt%)
Major	kamacite	6	93.3 ± 0.2[1]	6.6 ± 0.2	n.d.[2]	n.d.	n.d.	n.d.	n.d.	n.d.	n.d.
minerals	taenite	9	62.9 ± 8.0	37.1 ± 8.0	n.d.	n.d.	n.d.	n.d.	n.d.	n.d.	n.d.
	plessite	1	78.3	21.7	n.d.	n.d.	n.d.	n.d.	n.d.	n.d.	n.d.
Accessory	troilite	17	63.5	3.2	34.4 ± 7.9	2.5 ± 2.8	n.d.	n.d.	n.d.	n.d.	n.d.
minerals	daubréelite	22	21.1 ± 0.8	n.d.	42.2 ± 1.0	36.8 ± 0.7	n.d.	n.d.	n.d.	n.d.	n.d.
	zincian daubréelite	7	19.4 ± 1.9	n.d.	42.0 ± 1.4	35.8 ± 0.9	n.d.	n.d.	n.d.	n.d.	2.8 ± 0.3
	high Fe daubréelite	4	27.2 ± 1.8	n.d.	41.5 ± 1.0	31.1 ± 1.3	n.d.	n.d.	n.d.	n.d.	n.d.
	schreibersite	7	47.0 ± 3.4	38.7 ± 3.4	n.d.	n.d.	14.2 ± 0.7	n.d.	n.d.	n.d.	n.d.
	nickelphosphide	10	35.9 ± 3.0	50.3 ± 3.1	n.d.	n.d.	13.3 ± 0.5	n.d.	n.d.	n.d.	n.d.
	chromite	5	24.1 ± 0.8	n.d.	n.d.	45.2 ± 0.5	n.d.	30.0 ± 0.9	n.d.	n.d.	0.6 ± 0.7
	carlsbergite	3	4.4 ± 2.0	n.d.	n.d.	78.0 ± 4.1	n.d.	n.d.	15.8 ± 2.4	n.d.	n.d.
	copper	4	7.2 ± 5.8	1.2 ± 0.2	5.7 ± 3.9	2.2 ± 0.6	n.d.	n.d.	n.d.	85.5 ± 5.1	n.d.

[1] Average of n analyses (norm wt%) with standard deviation provided

[2] n.d. = not determined

Native copper is associated with four sulfide inclusions. The largest copper grain is 200 µm and found within a large troilite, daubréelite, and chromite inclusion (Fig. 2-13a). The largest occurrence of copper is found surrounding half of a sulfide inclusion with daubréelite-troilite exsolution lamellae (Fig. 2-16a). The side of the inclusion surrounded by native copper also has small Cu-rich flecks visible through the daubréelite and troilite lamellae (Fig 2-16b). Smaller grains have also been identified within other sulfides and range in size from 1 to 16 µm (Fig. 2-16c,d).

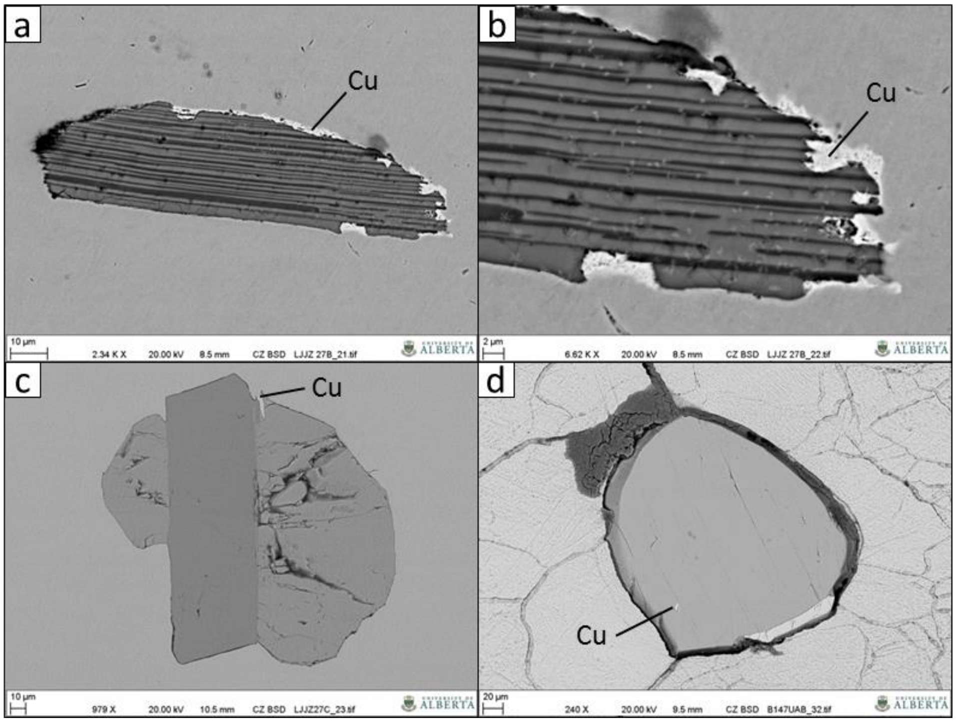

Figure 2-16: Occurrences of native copper (Cu). (a) Sulfide (troilite with darker daubréelite lamellae) partially rimmed with copper (white in colour). (b) Magnified view of a) revealing small light-coloured flecks of copper within the exsolution lamellae. (c) Narrow vertical copper vein along the top edge of the sulfide (troilite is highly fractured on left and right of inclusion with slightly darker grey daubréelite in middle). (d) Minute grain of copper within troilite inclusion. All BSE images; a-c) have polished unetched surfaces and d) is nitol-etched.

Terrestrial weathering is present on the exterior surfaces of all Whitecourt meteorites. The same weathering has also penetrated to the interior of some samples by way of cracks and fractures in the structure (Fig. 2-13a) or by the preferential corrosion of less-resistant minerals. Corrosion of the metal pieces produces iron oxyhydroxides and oxides. The most common secondary minerals are goethite/limonite ($FeO(OH)/FeO(OH)\cdot nH_2O$), akaganéite ($FeO(OH,Cl)$), and magnetite/hematite (Fe_3O_4/Fe_2O_3). Due to the presence of Ni within the meteorites Ni is

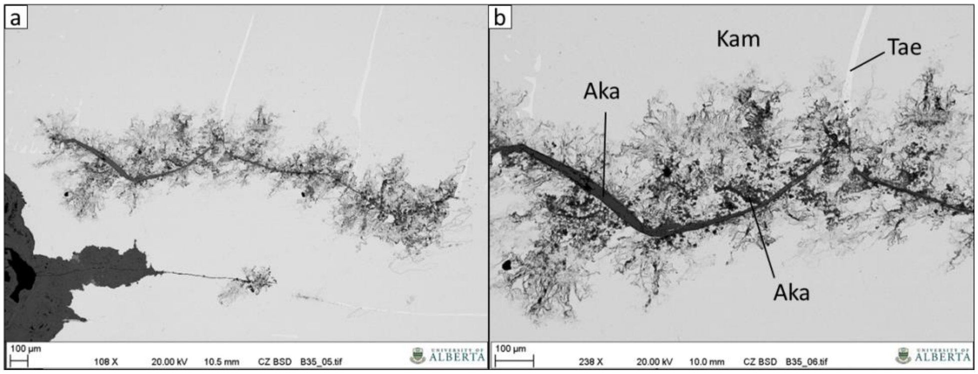

Figure 2-17: Terrestrial weathering. (a) Weathering on the polished surface of a shrapnel fragment. Dark colours at bottom left are secondary minerals have formed along the outer edge of the fragment. A non-uniform active corrosion front is present in center of image (medium grey area). (b) Higher magnified image of the left area of corrosion front containing akaganéite (Aka), kamacite (Kam), and taenite (Tae).

also incorporated into secondary minerals but only in low amounts. Akaganéite was detected on a freshly cut and polished surface along an active corrosion front (Fig. 2-17). Terrestrial soil components (Al, Si, Mg, K, Ca, and Na) also combine with the secondary minerals sometimes with mm-sized silicate grains being completely assimilated into the weathered rind.

2.4. Discussion

2.4.1. Distribution

Initial study of the Whitecourt meteorite distribution was reported by Kofman et al. (2010) which included over 2500 shrapnel fragments and a single regmaglypted individual for a total mass of about 70 kg. Since then the number of recorded shrapnel fragments has almost doubled, the number of individuals increased from one to fourteen, and the cumulative mass has more than tripled. This increase in sample size provides a more comprehensive meteorite distribution. Not only are the locations of the meteorites known within this distribution but over 99% are reported with a mass. The specimen masses can also be mapped as a distribution which provides an indication of the distances various mass ranges were ejected.

The shrapnel fragments do not have a normal strewnfield distribution; although the lateral distribution is approximately elliptical, the weight distribution is irregular, with meteorites of contrasting weight found close together. The shrapnel distribution (Fig. 2-2) is best explained through explosive dispersion upon impact (Kofman et al., 2010) as opposed to the atmospheric sorting which produces a typical weight-sorted, elliptical distribution (Norton, 2002). The lack of a large mass buried below the crater (Kofman et al., 2010) and the substantial amount of shrapnel fragments found around the crater support Kofman et al.'s (2010) conclusion of an explosive excavation event. Shrapnel fragments with a weight of 100 g or less account for 95% of reported finds having a reported weight. The largest weight subgroup with a weight <20 g has over 3100 fragments which account for 68% of the total number of meteorites with reported weights. Closer examination reveals 95% of the shrapnel fragments <20 g are within 350 m of the crater and 95% of fragments with weight between 20.1-100 g are within 500 m of the crater. This weight distribution suggests that shrapnel weight increases with distance away from the crater. Shrapnel pieces with weight >100 g decrease considerably in number so the same trend is not as defined. The lower shrapnel numbers for larger pieces is attributed to either the lack of shrapnel pieces generated from the impact (as larger pieces are more likely to be fragmented based on the high number of pieces <20 g) or their extent continues beyond the current search area. The more likely explanation is that fragments larger than 100 g are less stable and were more prone to fracturing during the impact event. This is also based on the documented meteorites, where the current distribution for shrapnel pieces should be close to their actual extent since searching has continued beyond the last discovered piece in most directions with no further finds. Some areas have a curious arrangement of shrapnel fragments found in a linear distribution very close together in an otherwise sparse dispersal in the surrounding area. This pattern was identified through personal searching experience and by other volunteers. This phenomenon was likely caused when shrapnel was expelled from the crater and embedded in the trunks of trees, which eventually fell and decomposed, leaving a row of fragments behind. Meteorites were found embedded in trees following the 1947 Sikhote-Alin fall (Krinov, 1966), which provides documented occurrences of this type of event.

RI size distribution is not typical of a strewnfield either and the extent of their distribution remains uncertain. The size sorting of known Whitecourt RIs does not adhere to a typical weight-sorted distribution of larger RIs located downrange (Fig. 2-3); rather, RIs have been recovered as close as 80 m apart with a difference in mass of 17 to 30 kg. The largest mass was the 1 m impactor that generated the crater, as there are no other craters present in the area. With most of the individuals located ENE of the crater the distribution is almost opposite to what is expected where the dispersion of smaller individuals is located in the downrange direction rather than uprange. With over 300 m separating some of the individuals their distribution is projected to continue well beyond the shrapnel field. Only 4 RIs are located beyond the shrapnel field so the recovery of RIs is biased to this region. It is unlikely that additional large RIs remain within the shrapnel distribution due to the extensive searching conducted within this area. The only individuals that may remain within the shrapnel field would be buried deeper than the limits small handheld metal detectors can detect. Recovery of further regmaglypted individuals will improve the knowledge regarding the atmospheric transit and break-up of this meteorite.

Overlap of these distributions indicates atmospheric break-up occurred low in the atmosphere. A small distribution area of 1.1 km by 0.75 km for the Whitecourt RIs is smaller but similar to the 2.1 km by 0.96 km distribution ellipse of Sikhote-Alin (Krinov, 1966). Notably, both Sikhote-Alin and Whitecourt have large individuals near smaller pieces. This pattern implies multiple small break-ups occurred; for the pieces to be close together the fragmentation would have happened late in the passage through the atmosphere. The duration of fragmentation was high enough for regmaglypts to form on the pieces but still low enough to preserve some of the more angular octahedral planes present on most pieces (Fig. 2-5). Preservation of octahedral planes suggests there may have been some orientation in flight as these planes were not as heavily ablated as the leading side. Alternatively, or in conjunction with low atmospheric break-up, the RI distribution could have been influenced by the crater-forming blast if they were falling close behind the impactor. In such a scenario the blast could have laterally transported RIs relative to where they would have otherwise fallen.

Impacts with preserved and recorded distributions are few but one that can be compared to Whitecourt is the Henbury crater field in Australia. The Henbury meteorite is a IIIAB iron meteorite which generated 13 confirmed impact craters and associated shrapnel fragments within a 1.0 km by 0.70 km area with individuals concentrated NE of the craters and extending for another 2 km in the same direction; the Henbury craters range from 6 to 145 m in diameter (Buhl and McColl, 2012). Similar to Whitecourt, Henbury meteorites show both the shrapnel fragment and RI morphologies. Henbury craters numbered 3 and 4 have diameters of approximately 40 m (Krinov, 1966), with shrapnel fragments concentrated to one side (west side), similar to the eastward concentration of fragments at Whitecourt. The number of Henbury meteorites recovered is much smaller than the number recovered from the Whitecourt site; this difference can be attributed to two main factors: the target material and the accuracy and detail of record keeping. Target material is a significant and controlling factor regarding the amount of shrapnel fragments produced. The Henbury site target material is Ordovician in age consisting of sandstones and quartzites (Alderman, 1932) whereas the Whitecourt crater formed in Quaternary glacial deposits overlain by fine-grained till (Kofman et al., 2010). Whitecourt's unconsolidated and more porous target material reduced pressures and forces during the impact, which would have intensified the fragmentation of the impactor leading to the survival of more shrapnel fragments (Howard, 2011). An impact into the harder and more consolidated target material found at the Henbury site would have decreased the amount of melt production

(Howard, 2011), and resulted in fewer shrapnel pieces surviving. Conflicting interpretations as to the fall direction of the Henbury meteorite as either SW to NE or the reverse, illustrates the limitations that exist regarding the knowledge of terrestrial impacts, possibly due to the fact that so few of this size exist to be studied in detail. Most commonly the Henbury fall direction is reported as going SW to NE, based on the size distribution of the craters (e.g. Krinov, 1966; Roddy et al., 1988); however, Henbury shrapnel is located to the west of the craters. If Henbury is used as a guide then Whitecourt's shrapnel should be distributed more towards the fall (in the WSW direction), which is not the case (Kofman et al., 2010). Another inconsistency regarding meteorite distribution for Henbury and Whitecourt is the location of RIs in relation to the associated crater(s). For both sites the RIs are downrange of the crater(s). The RIs are smaller than the masses that generated the craters, and since they were too small to form their own craters they should have lost their momentum first and have been found uprange of the crater(s). Differences in the distance RIs are found from the crater(s) between these impact sites could be attributed to different altitudes when fragmentation occurred; higher for Henbury and lower in the atmosphere for Whitecourt. A higher fragmentation altitude would explain the wider areal dispersion for Henbury than for Whitecourt. If the smaller individuals were caught in stronger prevailing winds or the jet stream then they would be carried farther east, which is a possibility for either location. The variations of shrapnel and RI distributions for two seemingly comparable impacts convey how dynamic terrestrial impacts are and the importance each impact contributes to our understanding of low-energy impact craters.

A definitive correlation between a Whitecourt meteorite's weight with either its recovery depth or its distance from crater is not evident. The size and orientation of a given fragment is more likely a factor in its recovery depth than its weight. If weight was the only determining factor then all small fragments would be near the surface and more massive samples would be found deeper. The impact site is located in an area having annual freeze-thaw cycles and since the meteorites are located within the soil's active layer there is potential for their vertical position to be affected. Frost heave experiments by Kolstrup and Thyrsted (2010, 2011) monitored vertical movements of 24 cm diameter globes and cubes composed of granite, concrete, and wood to determine whether the conductivity and specific gravity affected their movement in different sediment types over four and a half years; higher thermal conductivity causes the greatest vertical movements of buried objects. Frost heave also tends to rotate a body so the long axis is oriented perpendicular to the frost movement as shown in other experiments (e.g. Washburn, 1980; Johnson et al., 1977). These experiments also showed that more vertically oriented bodies experienced greater upward movement due to frost heave. Most recovered meteorites were not found in situ so their orientations cannot be verified, however, a large scale example using the two largest regmaglypted individuals can be used; those with weights of 31.5 kg and 19.7 kg. The top of the 31.5 kg individual and was found at a depth of 61 cm, with its long axis oriented vertically, whereas the 19.7 kg individual had a depth of only 8 cm but its longest axis was oriented horizontally. These documented large scale examples of RIs suggest that frost heave does not play a major role in meteorite recovery depth. If frost played a role in meteorite orientation and depth than the 19.7 kg individual would have been discovered more vertically and the 31.5 kg individual would have been found closer to the surface. Larger shrapnel fragments would also preferentially be found near the surface than smaller ones but this distribution is not observed. It is possible that localized saturation of the ground may have been a factor in vertical position in low lying areas or near stream beds. Saturation would cause the dense meteorites to sink deeper in the soil but direct evidence of this has not been detected. Based on observations for larger meteorites there has been little to no change in their orientation since the impact and thus have remained relatively undisturbed where they landed until recovered.

2.4.2. External morphology and internal texture

Nearly all shrapnel-shaped fragments have some angular and jagged edges often with smoother convex faces resulting from fragmentation and plastic deformation from the impact; this is most evident on larger fragments over 100 g. While the break-up of the impactor is the main influence on morphology the structural component to the Whitecourt meteorites in particular is also evident. The outward manifestation of the internal octahedral structure of Whitecourt meteorites can be recognized in many samples based on angles preserved between faces. Kamacite crystallization controls the octahedral structure and its fracturing would be easier along crystal planes rather than through them; even easier if pre-impact shocks weakened some of these planes. Forces during the terrestrial impact would have taken advantage of any planes of weakness. Most planes also display some degree of deformation which would have occurred almost immediately after fracturing while the fragment was still partially plastic. The rare fragments that have areas of nearly perfect or deformation-free octahedral structure (Fig. 2-5) clearly show the octahedral crystallization that occurred in the parent body that would otherwise have been lost to atmospheric ablation or plastic deformation generated by the impact.

Individual regmaglypted meteorites, which are much fewer in number, represent the pieces that broke off the main body in the lower and denser atmosphere at an altitude of several

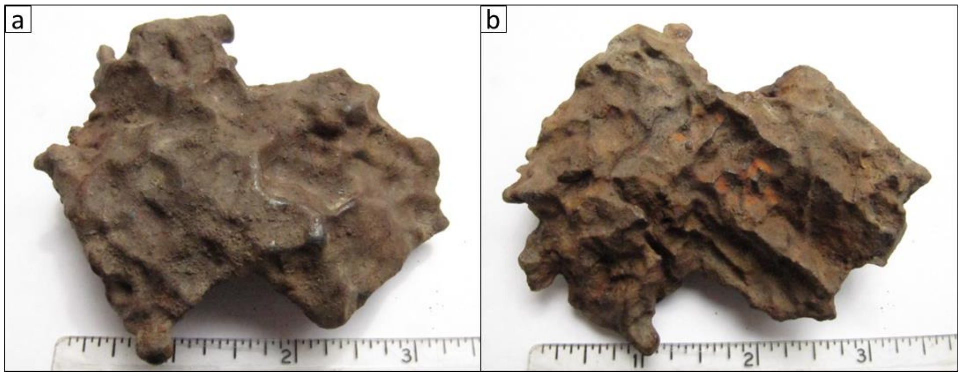

Figure 2-18: Different ablation patterns present on opposite sides of a regmaglypted individual. (a) Regmaglypts are rounded and well-developed on this side. (b) Surface on the reverse side is more angular with poorly developed regmaglypts and better defined octahedral fracture planes. [scales = in inches]

km (Krinov, 1966). This height is sufficient enough to keep the distribution area small and allow the development of regmaglypts but not high enough to completely obscure the angular fracture planes still visible on some of these pieces (Fig. 2-6). The etched RI slice in Figure 2-10a has external fracture planes (edges of the slice) with their orientation nearly parallel to the interior Widmanstätten pattern despite the overlaid ablation features. Since the fractured edges of this slice are close to being parallel to the Widmanstätten pattern the octahedral structure of the meteorite had a significant influence regarding how it broke apart from the larger mass. There is an absence of pronounced doming and orientation of Whitecourt individuals which supports a low altitude break-up where the formation of well-developed cones would be hindered. Pieces that experienced more substantial melting and ablation on the leading side due to partial orientation are rounder and have more pronounced regmaglypts whereas the reverse side was more protected from melting and thus retained more angular edges (Fig. 2-18). Individuals vary in mass and quality of regmaglypts since they would not all have separated from the main body at the same time and followed different flight paths. The heat alteration zone is almost absent on slices of the 6.5 kg individual except for several isolated areas along the edge of the slices (Fig. 2-10b). This is the only individual that has been sliced to expose the interior so the presence of a heat alteration zone on other RIs will depend on their state of terrestrial weathering. These narrow partially recrystallized areas confirm that RIs spalled off the main mass during atmospheric transit and were independently heated in order to generate this feature. Ablative effects on shrapnel fragments have not been identified.

The internal texture observed on the slice of the RI provides insight to the extent of pre-terrestrial shock or reheating events as this and other RIs were not involved in the crater-forming impact. The slice shows there was some localized heating and recrystallization after the formation of the Widmanstätten pattern but before its terrestrial impact, which can be attributed to a collision with at least one other body while in space. Most of the kamacite lamellae in the slice have roughly the same width with several that are more than twice this width (Fig. 2-10a). Thicker lamellae were likely melted then cooled too rapidly to re-form the Widmanstätten texture; these recrystallized lamellae are restricted to specific areas of the slice. Even though localized melting occurred there was no deformation associated as the orientation of the lamellae remains parallel so melting and recrystallization occurred in place.

Deformation of shrapnel-shaped fragments is also detected by examining the internal texture, the Widmanstätten pattern, and by comparison to the corresponding pattern present in an individual. In the studied Whitecourt fragments, the deformation is not extreme but when present it is usually localized to a specific area of the fragment. In unetched samples the distortion is best observed in the taenite lamellae which should be parallel based on the cooling and octahedral growth patterns of kamacite (Yang and Goldstein, 2005). The heat generated during the impact was not high enough to melt and recrystallize the metallic components or accessory minerals but the Fe-Ni alloys must have become plastic. In Figure 2-7 deformation resulting from the impact is visible along the edges and in the interior of shrapnel samples. In some fragments the distorted taenite lamellae have shear deformation or minute dislocations, which are visible at the micro-scale with high magnification (Fig. 2-9d).

The presence of two morphological groups is not unique as they have been documented at other iron meteorite impact sites such as Henbury, Kamil, and Sikhote-Alin (Buhl and McColl, 2012; Folco et al., 2011; Buchwald, 1975; Krinov, 1966). The shrapnel morphology is observed in iron meteorites of the same chemical and structural type (e.g., Henbury) or different types (e.g., Sikhote-Alin and Kamil) as Whitecourt. This morphology is influenced more by the catastrophic break-up of the body in the atmosphere (Sikhote-Alin) or by the impact with Earth's surface (Henbury, Kamil) than by the chemical type of iron meteorite. Either break-up mechanism produces fragments containing plastic deformation effects similar to those observed in Whitecourt fragments, apparently making this a common feature of fragmented iron meteorites. The morphology and ablation features of individuals from these impact sites are similar to Whitecourt where differences are attributed to the quality of preservation resulting from terrestrial weathering.

2.4.3. Composition

Fe-Ni alloys and their proportions influence trends in the presence and abundance of accessory minerals found in iron meteorites. For example low-Ni IIIAB meteorites, such as Whitecourt, have low P and S contents so smaller and fewer mineral inclusions containing these elements are likely to form (Scott and Wasson, 1975).

The most common accessory minerals in Whitecourt meteorites are the sulfides troilite and daubréelite. These mineral inclusions have diverse arrangements from inclusions that appear homogenous in composition from their cross-section to those that are more complex with exsolution of the two sulfides. Sulfide exsolution is present in 46% of the sulfide inclusions examined in Whitecourt meteorites. In these cases the daubréelite lamellae have exsolved from the parent mineral troilite and are oriented parallel to (0001) of the host troilite (Ramdohr, 1963). Exsolution textures are not constant between inclusions where the widths of lamellae vary from fine to thick; lamellar widths remain relatively constant within the same inclusion. The orientations of lamellae are not constant for sulfides within a sample (Fig. 2-13g). Sulfide inclusions that lack visible exsolution are <150 µm and are daubréelite in composition. Buchwald (1975) reports the ratio of daubréelite to troilite is inversely correlated with the size of the troilite inclusion and small inclusions (100 µm) contain up to 50% daubréelite. This observation appears to hold true for the sulfides examined in Whitecourt samples: inclusions comprised of only daubréelite range in diameter from 12 to 145 µm and when daubréelite coexists with troilite the apparent amount of daubréelite present decreases as the size of the inclusion and the amount of troilite increases. For inclusions where daubréelite appears as the only mineral phase, it cannot be determined with certainty if this is actually the case or if it is an exsolved inclusion where the cross-section coincides with the orientation of a wider lamella. All troilite present is associated with daubréelite and all troilite occurrences, except for one, have minute fractures which are absent in daubréelite. The fractures are a result of troilite's thermal expansion when it transitions from the β to α phase as it cools (Ramdohr, 1963; Tenailleau et al., 2005). Thermal expansion coefficients represent the amount of contraction a mineral undergoes and the higher the value, the more it contracts. Tenailleau et al. (2005) determined the thermal expansion coefficients for the β phase over the temperature range 873-573 K to be 7.4×10^{-5} K^{-1} and for the α phase from 573-373 K to be 14.1×10^{-5} K^{-1}. Troilite does not have cleavage planes on which these fractures would preferentially form, unlike with pyrrhotite, so they form perpendicular to (0001) of troilite. This is best observed in exsolution lamellae where the fractures are oriented relatively perpendicular to the alternating troilite and daubréelite lamellae (Fig. 2-13e). These fractures are more abundant in the sulfide inclusions with narrow exsolution lamellae so the confining nature of the lamellae enhances the effect of the thermal contraction when the other mineral, daubréelite in this case, does not contract the same amount. In larger sulfide inclusions, fractures are present but are farther apart and the fracture lines are more random since troilite is less confined (Fig. 2-13f). It is rare for fractures to develop in daubréelite but if present they develop parallel to (111) (Ramdohr, 1963). There is no evidence of reheating of the sulfides examined. The only modifications visible in the sulfides examined are the thermal fractures created during cooling and small shear dislocations and fractures within several inclusions. Some sulfides are located at and near the edge of shrapnel fragments, which would be the most likely to be melted as a result of the impact and fragmentation, but recrystallization in these areas is not observed. All troilite and daubréelite inclusions analyzed by EPMA have minor amounts of Cu substituting for Fe, ranging from 0.11 to 0.63 wt% for troilite and 0.07 to 1.64 wt% for daubréelite. Daubréelite also has Zn substituting for Fe which varies from 0.00 to 3.76 wt%. The detection of Zn in daubréelite was first reported by El Goresy (1967) where zincian daubréelite grains had up to 8 wt% Zn. Even though daubréelite and troilite are commonly associated in Whitecourt meteorites, Zn was detected in less than one third of analyzed troilite and when Zn was present it was only 0.01 wt%. This is a reflection of the differences in the crystal structures of these sulfides where daubréelite is able to accommodate Zn with its slightly smaller ionic radius while the tighter packed and distorted Fe bonds of troilite (Vaughan, 1978) inhibit this substitution. Other sulfides such as sphalerite (ZnS) and chalcopyrite ($CuFeS_2$) are rare but have been reported in other IIIAB iron meteorites (Scott and Wasson, 1975; Mittlefehldt et al., 1998) but have yet to be detected in Whitecourt meteorites.

The phosphorous content between the two Fe-Ni phosphides remains relatively constant around 12 wt% where the range of Fe and Ni for the two phosphides varies between 7 to 12 wt% respectively (Table 2-1). These trends in phosphide composition show that it is the amount of metal present that determines the phosphide and not the amount of P. This trend is was recently identified in another iron meteorite, Cheder - a group IID meteorite, by Agafonov et al. (2011) which also has a wide variation in the Fe and Ni content while the P content remains almost constant. Clarke and Goldstein (1978) proposed four types of Fe-Ni phosphides distinguished by type of nucleation and temperature; heterogeneous nucleation produces grain boundary or taenite border and massive schreibersite around 500°C and 800°C respectively and homogeneous nucleation produces microrhabdites and rhabdites at 400°C and 600°C respectively. The phosphides identified in Whitecourt samples fall into the grain boundary type except for one which crystallized within net plessite. The size of the grain boundary phosphides is determined by the rate of P diffusion which is a function of temperature. Phosphide size is correlated with its Ni content where smaller sizes typically have the higher Ni value (Goldstein and Ogilvie, 1963). This corresponds to Whitecourt grain boundary nickelphosphides with Ni content between 46-55 wt% and a ratio of the size of nickelphosphide to its associated sulfide inclusion of less than 0.4. Another observed trend is when the size of the phosphide is similar to, or larger than, its associated sulfide then schreibersite forms rather than the Ni-rich nickelphosphide. It remains unclear if this trend occurs in other iron meteorites as reports of this specific association could not be found, due in part to the fact that not all Ni-rich phosphides are labeled as nickelphosphide but instead referred to as high Ni schreibersite (Goldstein and Ogilvie, 1963; Clark and Goldstein, 1978) or taenite border schreibersite (Miler and Gosar, 2011). The case where a distinction between the phosphides is made is in Agafonov's (2011) citation of Britvin et al. (1999) which reports nickelphosphide as having a Ni content of at least 43.4 wt% Ni. Only 39% of sulfide inclusions examined in Whitecourt meteorites are associated with Fe-Ni phosphides and when the association exists the phosphide is often very small compared to the whole sulfide. Phosphides do not completely surround sulfides so this value is biased to the specific sections of inclusions examined. Larger sulfides have more surface area not visible in these sections so all phosphide-sulphide associations were likely not observed.

Chromite is the only oxide detected in Whitecourt meteorites and while it is considered a common minor mineral which is present in many meteorites but in small amounts (Mittlefehldt et al., 1998); only five occurrences were identified in examined Whitecourt samples using SEM analysis. These five occurrences have diameters of about 200-500 µm, consistent with the observation that larger chromite grains (>2 mm diameter) in IIIAB iron meteorites are rare (Wasson et al., 1999). All these occurrences, except for one, are associated with large troilite inclusions. The cross-section of chromite is visible in Fig. 2-13a is consistent with its isometric crystal structure; chromite is equant and rounded in the remaining troilite-associated occurrences. The solitary occurrence in kamacite is smaller in size and has an irregular shape. Mittlefehldt et al. (1998) report that chromite associated with metal, as opposed to silicate inclusions which are absent in Whitecourt, are close to pure $FeCr_2O_4$ in composition. Semi-quantitative analysis indicates this is also true for Whitecourt samples but due to the size and shape of chromite-bearing samples EPMA could not be performed.

The nitride carlsbergite, CrN, is not known as a terrestrial mineral but is a common minor mineral in iron meteorites (Mittlefehldt et al., 1998). Carlsbergite forms small grains between the sizes of 8-17 µm within kamacite and as ≤2 µm grains so its presence may be overlooked in samples when high magnification is not used. The results from the electron microprobe show the composition obtained for carlsbergite in Whitecourt is nearly the same as the composition first reported for this mineral (Buchwald and Scott, 1971). The composition for carlsbergite inclusions is fairly consistent and where deviations are present it is in the amount of Cr, where several wt% Fe substitute for Cr, with trace amounts of Ni and Co.

Native copper can be found in Whitecourt meteorites and is associated with troilite and daubréelite inclusions. Copper in sulfides can develop as small or large native Cu grains (1 to 200 µm), throughout a specific area within in the sulfide (Fig. 2-16b), or along the sulfide-metal interface (Fig. 2-16c,d). Native Cu was not found as isolated grains within the metal matrix. The sulfides with these Cu grains have the highest Cu concentrations and would be the most likely location for Cu-containing sulfides such as chalcocite (Cu_2S), chalcopyrite ($CuFeS_2$) or cubanite ($CuFe_2S_3$) to occur, but none were detected in Whitecourt meteorites. From EPMA analysis Cu was only detected in the sulfides troilite and daubréelite and ranged from 0.2 to 0.6 wt% (Table 2-1) and in kamacite and taenite Cu was <0.07 wt%.. Copper is absent from all phosphides analyzed and was not analyzed in carlsbergite or chromite.

Based on these observations the inferred order of precipitation of accessory minerals observed in Whitecourt meteorites is chromite followed by troilite, since sulfides are not present in the chromite grains and troilite surrounds chromite. Further cooling leads to the precipitation of daubréelite, carlsbergite, and then phosphides. Copper precipitates after the formation of troilite and daubréelite and their exsolution from one another since Cu does not appear to affect the development of exsolution lamellae (Fig. 2-16b). Copper grains have not been found in close proximity to carlsbergite or phosphide inclusions. Phosphides are the last accessory mineral to form as they border all other accessory phases and not found within them. Carlsbergite precipitates after daubréelite and before phosphides by the same reasoning and this sequence is illustrated in Figure 2-15e. Troilite and chromite came directly from the melt whereas the remaining minerals nucleated after the taenite to kamacite transformation. The relationship between the octahedral structure of the Widmanstätten pattern and troilite is not easily observed in the Whitecourt meteorites examined due to the lack of large troilite inclusions.

Terrestrial weathering has affected all Whitecourt meteorites but has not affected them all to the same extent. When some meteorites were recovered they were also reported with a generalized soil type; there appears to be a rough correlation between the extent of weathering to the meteorite's exterior surface and the type of soil it was recovered from. The estimated amount of weathering is based on the thickness of the weathered rind that has accumulated on the outer surface of the meteorite. The least weathered meteorites were located in sand-rich sediment and the most heavily weathered were in more clay-rich sediment. This observation corresponds with the ability of sediment to retain moisture and the more moisture present, the higher the surface alteration of the metal fragments. Often the extent of weathering is not consistent around the edge of the meteorite suggesting that the orientation of the meteorite may have a role in the rate of weathering in addition to the type of soil it is found in. The shape of the meteorite may trap moisture due to its orientation or the top edge might be in contact with more moisture if its shape shelters the bottom edge from such contact. Weathering is mostly confined to the outermost surface of Whitecourt meteorites, although fractures that penetrate into the interior of a fragment can provide additional weathering sites (Fig. 2-19). These fractures are highly susceptible to alteration, which was observed in some of the samples that were cut to expose their interior composition, as they allow groundwater entry into the interior and act as an initiation site for terrestrial weathering. Some components of meteorites are more susceptible to weathering than others, which reflect their stability on Earth's surface.

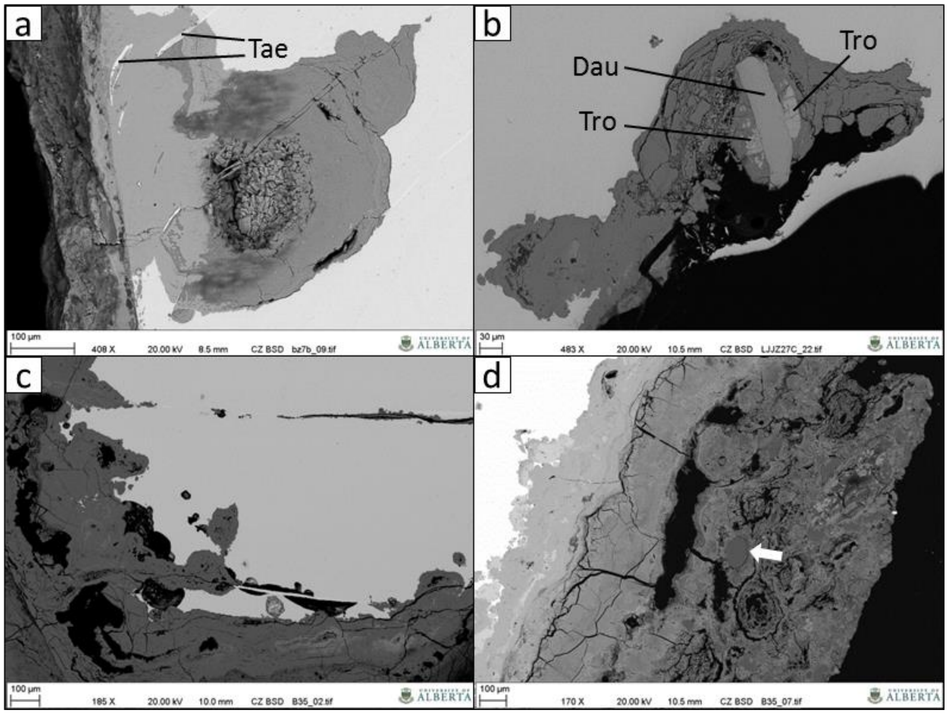

Figure 2-19: Terrestrial weathering. (a) Deep corrosion along the edge of a fragment with taenite (Tae) present. (b) Weathering around a sulfide inclusion containing daubréelite (Dau) and troilite (Tro). (c) Layers of weathering products formed along the outer surface of a fragment and its penetration into the interior by the corrosion front or along cracks. (d) Highly weathered outer surface of a fragment showing different oxidation layers. A small quartz grain has been incorporated into the weathered crust (arrow). All are polished unetched surfaces and BSE images.

In Antarctic weathering conditions Gooding (1986) observed that troilite is less susceptible than Fe-Ni metals and taenite is less susceptible than kamacite. In some cases where terrestrial weathering has penetrated into the fragment taenite can remain unaffected (Fig. 2-19a). Even between sulfides there are differences in their terrestrial stability where daubréelite is not easily affected by oxidation unlike troilite (Ramdohr, 1963), which has been observed by several inclusions which are near the outer edges of some Whitecourt fragments (Fig. 2-19b). These observations also hold true for Whitecourt meteorites, although the overall amount of weathering would be higher for Whitecourt than Antarctica since half their terrestrial life has been in warmer weather during wetter summers. Only several locations in Whitecourt samples examined was the corrosion product akaganéite detected. Akaganéite forms along the corrosion front in iron meteorites and over time its Cl is lost and it decomposes to goethite and maghemite making it a minor corrosion product (Buchwald and Clarke, 1989). Akaganéite was found on the freshly cut and polished surface of improperly stored samples, providing ideal conditions for corrosion to re-initiate. Any Ni that was incorporated into akaganéite is preserved in the decomposition products, allowing initial meteoritic compositions to be deduced: Ni may be incorporated into akaganéite and if the ratio of Fe to Ni is around 4 then it formed from taenite. More commonly the ratio is closer to 16 indicating it formed from kamacite, the more susceptible alloy (Buchwald and Clarke, 1989).

Trends observed by Scott and Wasson (1975) for low Ni IIIAB meteorites correspond well with Whitecourt. Table 2-3 shows specific and average bulk composition values for IIIAB meteorites for comparison with Whitecourt. Values for Whitecourt fall near or slightly below the average values obtained, except for Ir, demonstrating that Whitecourt has an average bulk IIIAB composition. Iron meteorites are grouped by bulk Ni content and Whitecourt's bulk Ni content, as determined by Herd et al. (2008), of 8.11 ± 0.13 wt% places it near the low Ni-content end. Large iron meteorite groups, including IIIAB, have a peak frequency in low Ni members which

Table 2-3: Trends in IIIAB meteorites

Name	Ni wt%	Co wt%	Ir µg/g	Ga µg/g	Ge µg/g	Au µg/g	Reference
Henbury	7.51	0.45	13.60	17.4	34.6	n/a	Buchwald (1975)
Bagnone	7.80	0.51	8.30	20.8	36.6	0.54	D'Orazio et al. (2004)
Javorje	7.83	0.48	7.60	25.0	47.0	0.47	Miler and Gosar (2011)
Alatage	7.89	0.47	11.33	18.2	34.0	0.51	Bartoschewitz and Spettel (2001)
Shişr 043	8.07	0.50	3.92	18.8	37.3	0.59	Al-Kathiri et al. (2006)
Whitecourt	**8.11**	**0.50**	**10.30**	**19.0**	**<40**	**0.66**	Herd et al. (2008)
Franceville	8.39	0.47	0.38	20.4	42.4	n/a	Olsen et al. (1974)
Gnowangerup	8.59	0.53	1.00	20.0	44.0	n/a	Laeter (1982)
Pozo Almonte	8.86	0.51	0.24	23.3	43.9	1.08	Wasson and Canut de Bon (1998)
Sychevka	9.10	0.57	0.37	23.6	n/a	1.10	Krot et al. (1992)
average	8.22	0.50	5.70	20.65	39.97	0.71	
IIIA	7.1-9.3	n/a	0.17-19	17-23	32-47	n/a	Scott et al. (1973)
IIIB	8.4-10.5	n/a	0.014-0.17	16-21	27-46	n/a	Scott et al. (1973)
n	157	83	133	134	133	n/a	IIIAB meteorite data compiled from Buchwald (1975)
average	8.31	0.51	3.15	22.51	54.99	n/a	

decreases with higher Ni (Scott and Wasson, 1975). Iron meteorite groups form continuous sequences when plotted on a Ga-Ni logarithmic plot (Fig. 1-2) and by looking closer at just the IIIAB group, the composition for Whitecourt falls within the IIIAB field (Fig. 2-20). The bulk Ni content of iron meteorites, and more specifically the IIIAB group, have associated trends which affect the frequency of other minerals, such as phosphides and Cr-bearing minerals. Accessory minerals reported for the IIIAB group and Whitecourt's average bulk composition are comparable (Scott and Wasson, 1975; Mittlefehldt et al., 1998). At austenitic temperatures in octahedrites (>700-800°C) the only phases present in iron meteorites are troilite, chromite, and taenite (Uhlig, 1954; Buchwald, 1975). As these phases cool taenite transforms to kamacite and the remaining minerals (schreibersite, daubréelite, carlsbergite) precipitate. These cooling relations demonstrate why most minerals are closely associated with troilite and why they are located within kamacite or at kamacite-taenite interfaces. Mineral grains not associated with troilite are small and generally small particles precipitate at lower temperatures (Axon, 1968). Cr-bearing minerals found in the Whitecourt meteorite include carlsbergite, daubréelite, and chromite. Carlsbergite is plentiful in irons with ≤8 wt% Ni and decreases in frequency as the bulk Ni content increases (Scott and Wasson, 1975, Wasson et al., 1999). Whitecourt's low bulk Ni agrees with this trend and the small sizes of carlsbergite found correspond to sizes reported for isolated

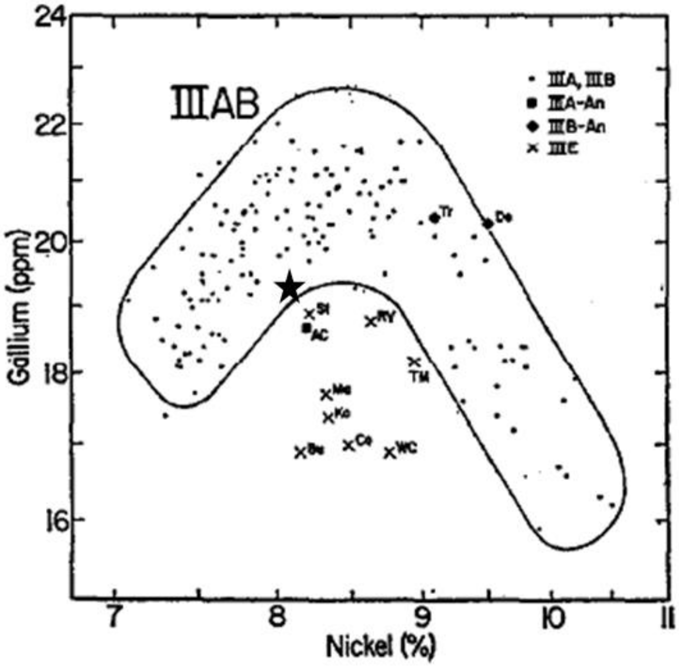

Figure 2-20: Logarithmic plot of gallium (Ga) vs. nickel (Ni) for the IIIAB iron meteorite group. The Whitecourt meteorite corresponds to the location indicated by the black star. [from Scott et al., 1973]

grains in kamacite and grain boundary precipitates by Buchwald and Scott (1971). Once bulk Ni content is greater than 9 wt% the presence of daubréelite and carlsbergite is not recorded in IIIAB meteorites (Wasson et al., 1999). This has implications for the occurrence of chromite. Chromite is very sparse in Whitecourt samples compared to the other Cr-bearing minerals carlsbergite and daubréelite suggesting its presence is not directly correlated to the bulk Ni or Au content. Chromite has lithophile tendencies and is more incompatible than daubréelite or carlsbergite and large chromite grains >500 µm are usually associated with troilite inclusions >1 mm. Large troilite inclusions are considered to be trapped melt and contain higher Cr contents than in the surrounding metal (Wasson et al., 1999), which matches the observation in the Whitecourt meteorites that many Cr-minerals are associated with sulfides. The two largest sulfide inclusions are the ones that contain chromite and fall into this category. The final accessory phase identified in Whitecourt meteorites is copper. Native copper is considered a rare occurrence in iron meteorites as a group and type IIIAB are known to be very low in Cu (Buchwald, 1975). There are some IIIAB meteorites, like Cape York, where the occurrence of native Cu is abundant in troilite inclusions (Kracher et al., 1977). Copper is in solid solution with kamacite and sulfides and is one of the last phases to form as it was observed in troilite-daubréelite exsolution lamellae with no apparent influence on their development.

2.5. Conclusions

Recent analysis of the Whitecourt Meteorite Impact Crater site has built upon previous studies and expanded the knowledge of the distribution as well as providing detailed compositional information on the Whitecourt meteorites. Although Whitecourt is a typical IIIAB iron meteorite, knowledge of its mineralogy and petrology is important when combined with the deformational effects of the impactor's fragmentation. An expanded distribution map provides a clearer picture of how the meteorites were dispersed out of the crater as shrapnel-shaped fragments or distributed through atmospheric processes. With fewer than 20 terrestrial impacts associated with meteorites (Earth Impact Database, University of New Brunswick, 2013) the examination and documentation of meteorites at Whitecourt makes it an important resource to future discoveries of small terrestrial impact craters. Expanding the knowledge of small low-energy impact events on Earth could help realize the potential effects such an impact would have in modern times as iron meteorites similar in size to Whitecourt are predicted to arrive at Earth's surface about once every 50 years (Bland and Artemieva, 2006).

Bibliography

Agafonov L. V., Popov V. A., Anoshin G. N., Pospelova L. N., Zabelin V. I., and Kudryavtsev V. I. 2011. The Cheder iron meteorite (Tuva): mineral composition, structure, and PGE and REE contents. *Russian Geology and Geophysics* 52:620-630.

Alderman A. R. 1932. The meteorite craters at Henbury, Central Australia. *Mineralogical Magazine* 23:19-32.

Al-Kathiri A., Hofmann B. A., Gnos E., Eugster O., Welton K. C., and Krähenbühl U. 2006. Shişr 043 (IIIAB medium octahedrite): The first iron meteorite from the Oman desert. *Meteoritics & Planetary Science* 41:A217-A230.

Artemieva N. and Pierazzo E. 2011. The Canyon Diablo impact event: 2. Projectile fate and target melting upon impact. *Meteoritics & Planetary Science* 46:805-829.

Axon H. J. 1968. The metallurgy of meteorites. *Progress in Materials Science* 13:183-228.

Bartoschewitz R. and Spettel B. 2001. The Alatage meteorite, China. *Meteoritics and Planetary Science* 36:A237-A239.

Bland P. A. and Artemieva N. A. 2006. The rate of small impacts on Earth. *Meteoritics & Planetary Science* 41:607-631.

Buchwald V. F., 1975. Handbook of iron meteorites. Los Angeles: University of California Press. 1418 p.

Buchwald V. F. and Clarke R. S. 1989. Corrosion of Fe-Ni alloys by Cl-containing akaganéite (β-FeOOH): The Antarctic meteorite case. *American Mineralogist* 74:656-667.

Buchwald V. F. and Scott E. R. D. 1971. First nitride (CrN) in iron meteorites. *Nature Physical Science* 233:113-114.

Buhl S. and McColl D. 2012. *Henbury craters & meteorites, their discovery, history and study*, 1st ed. Hamburg: Reimer GmbH & Co.KG. 166 p.

Clarke R. S. and Goldstein J. I. 1978. Schreibersite growth and its influence on the metallography of coarse-structured iron meteorites. *Smithsonian Contributions to the Earth Sciences* 21:1-80.

D'Orazio M., Folco L., and Perchiazzi N. 2004. The Bagnone iron meteorite (Tuscany, Italy): History, mineralogy, and chemical classification. *Meteoritics & Planetary Science* 39:A133-A138.

El Goresy A. 1967. Quantitative electron microprobe analyses of coexisting sphalerite, daubréelite and troilite in the Odessa iron meteorite and their genetic implications. *Geochimica et Cosmochimica Acta* 31:1667-1676.

Folco L., Di Martino M., El Barkooky A., D'Orazio M., Lethy A., Urbini S., Nicholosi I., Hafez M., Cordier C., van Ginneken M., Zeoli A., Radwan A. M., El Khrepy S., El Gabry M., Gomaa M., Barakat A. A., Serra R., and El Sharkawi M. 2011. Kamil Crater (Egypt): Ground truth for small-scale meteorite impacts on Earth. *Geology* 39:179-182.

Goldstein J. I. and Ogilvie R. E. 1963. Electron microanalysis of metallic meteorites Part 1 - Phosphides and sulfides. *Geochimica at Cosmochimica Acta* 27:623-637.

Gooding J. L. 1986. Weathering of stony meteorites in Antarctica. In *Lunar and Planetary Institute International Workshop on Antarctic Meteorites*, LPI Tech Rpt 86-01:48-54.

Herd C. D. K., Froese D. G., Walton E. L., Kofman R. S., Herd E. P. K., and Duke M. J. M. 2008. Anatomy of a young impact event in central Alberta, Canada: Prospects for the missing Holocene impact record. *Geology* 36:955-958.

Howard K. T. 2011. Volatile enhanced dispersal of high velocity impact melts and the origin of tektites. *Proceedings of the Geologists' Association* 122:363-382.

Johnson D. L., Muhs D. R., and Barnhardt M. L. 1977. The effects of frost heaving on objects in soils II: Laboratory experiments. *Plains Anthropologist* 22:133-147.

Kofman R. S., Herd C. D. K., and Froese D. G. 2010. The Whitecourt meteorite impact crater, Alberta, Canada. *Meteoritics & Planetary Science* 45:1429-1445.

Kolstrup E. and Thyrsted T. 2010. Stone heave field experiment in clayey silt. *Geomorphology* 117:90-105.

Kolstrup E. and Thyrsted T. 2011. Stone heave field experiment in sand. *Geomorphology* 129:361-375.

Kracher A., Kurat G., and Buchwald V. F. 1977. Cape York: The extraordinary mineralogy of an ordinary iron meteorite and its implication for the genesis of IIIAB irons. *Geochemical Journal* 11:207-217.

Krinov E. L. 1966. *Giant meteorites,* 1st English ed. New York: Pergamon Press. 39 p.

Krot A. N., Zaslavskay N. I., Petaev M. I., Kononokova N. N., Kolesov G. M., and Barsukova L. D. 1992. The Sychevka IIIAB iron meteorite: A new find from Russia. *Meteoritics* 27:465-466.

Laeter J. R. 1982. Two new iron meteorites from Western Australia. *Meteoritics* 17:135-140.

Miler M. and Gosar M. 2011. Mineral and chemical composition of the new iron meteorite Javorje from Slovenia. *Meteoritics & Planetary Science* 46:1939-1946.

Mittlefehldt D. W., McCoy T. J., Goodrich C. A., and Kracher A. 1998. Non-chondritic meteorites from asteroidal bodies. In *Planetary materials*, edited by Papike J. J. Washington: Mineralogical Society of America. pp. 4-1--4-195.

Norton O. R. 2002. The Cambridge encyclopedia of meteorites, 1st ed. Cambridge: Cambridge University Press. 354 p.

Olsen E. J., Huss G. I., and Pearl R. M. 1974. The Ellicott meteorite. *Meteoritics* 9:263-269.

Ramdohr P. 1963. The opaque minerals in stony meteorites. *Journal of Geophysical Research* 68:2011-2036.

Roddy D. J., Shoemaker E. M., Shoemaker C. S., and Roddy J. K. 1988. Aerial photography and geologic studies of impact structures in Australia (abstract #1501). 19th Lunar and Planetary Science Conference.

Scott E. R. D., Wasson J. T., and Buchwald V. F. 1973. The chemical classification of iron meteorites – VII. A reinvestigation of irons with Ge concentrations between 25 and 80 ppm. *Geochimica et Cosmochimica Acta* 37:1957-1983.

Scott E. R. D. and Wasson J. T. 1975. Classification and properties of iron meteorites. *Reviews of Geophysics and Space Physics* 13:527-546.

Tenailleau C., Etschmann B., Wang H., Pring A., Grguric B., and Studer A. 2005. Thermal expansion of troilite and pyrrhotite determined by in situ cooling (873 to 373 K) neutron powder diffraction measurements. *Mineralogical Magazine* 69:205-216.

Uhlig H. H. 1954. Contribution of metallurgy to the origin of meteorites Part I - Structure of metallic meteorites, their composition and the effect of pressure. *Geochimica et Cosmochimica Acta* 6:282-301.

University of New Brunswick, 2013, Earth Impact Database: http://www.passc.net/EarthImpactDatabase/index.html. Accessed 6 July 2013.

Vaughan D. J. and Craig J. R. 1978. *Mineral chemistry of metal sulfides*. Cambridge: Cambridge University Press. 493 p.

Washburn A. L. 1980. *Geocryology - A survey of periglacial processes and environments*. New York: John Wiley & Sons. 406 p.

Wasson J. T. and Canut de Bon C. 1998. New Chilean iron meteorites: Medium octahedrites from Northern Chile are unique. *Meteoritics & Planetary Science* 33:175-179.

Wasson J. T., Lange D. E., Francis C. A., and Ulff-Møller F. 1999. Massive chromite in the Brenham pallasite and the fractionation of Cr during the crystallization of asteroidal cores. *Geochimica et Cosmochimica Acta* 63:1219-1232.

Wickman F. E. 1970. The Muonionalusta meteorites, when and where did they fall? *Geologiska Föreningen I Stockholm Förhandlingar* 992:404-405.

Yang J. and Goldstein J. I. 2005. The formation of the Widmanstätten structure in meteorites. *Meteoritics & Planetary Science* 40:239-253.

CHAPTER 3: Discovery of amorphous carbonaceous spherules and their link to the WMIC, a low-energy impact event

3.1. Introduction

Low energy impacts are not commonly preserved in Earth's terrestrial impact record so limited information exists for them. The absence of impact melt and large scale shock features, such as shattercones, in these types of impact craters may contribute to the lower detection rate of these statistically more frequent events (Bland and Artemieva, 2006). Low-energy impact craters with younger ages are more likely to preserve any melt or shock features as less time would pass for surface processes, such as erosion or infilling, to degrade or conceal them. The significance of the Whitecourt Meteorite Impact Crater (WMIC) discovery is that it has a young age, providing an opportunity to investigate the presence of shock features and impact generated melt in a low-energy event.

Previous research of the WMIC found that the impact event generated limited small scale shock effects which included planar microstructures in quartz, meteorite dust, and rare Fe-Ni oxide spherules recovered from within the crater fill (Kofman et al., 2010). Subsequent examination of the meteorites that survived the impact revealed the presence of small black spherules adhered to the exterior surface of some meteorites (Fig. 3-1). Further investigation of these dark spherules found they were a small component of the soil surrounding the crater and did not have a uniform distribution. The spherules are composed primarily of amorphous carbon and are generally spherical with a few rare morphologies identified. If the carbonaceous spherules are impact generated then this is the first report of such spherules found directly associated with a terrestrial impact crater.

Figure 3-1: Carbonaceous spherule adhered to shrapnel meteorite surface. (a) Small meteorite with spherule indicated by dashed box. (b) Close-up of spherule which is half embedded into the terrestrial weathering rind. [scale divisions = in mm]

Meteorite impacts are rare and sudden events where all effects and processes involved may not be well understood. In a highly vegetated area a pyrolytic reaction may occur at the time of impact; pyrolysis is a process where organic matter is thermally decomposed in the absence of air or oxygen or in oxygen-deficient conditions (Graham et al., 1984). Various rates of pyrolysis are possible. Wildfires utilize slow pyrolytic reactions (Pyne, 1984) whereas conditions related to a meteorite impact would involve a more rapid reaction rate based on the scale, magnitude, and energy generated by such an event. Pyrolytic reactions are categorized based on heating rate, temperature reached, and vapour residence time. Using these parameters Graham et al. (1984) define two rapid pyrolytic reactions as follows: flash pyrolysis has a heating rate of 10-1000°C/s, temperatures around 400-600°C, and vapour residence times less than 2 s while fast pyrolysis has a higher heating rate of 1000-10000°C/s, temperatures higher than 600°C, and vapour residence times less than 0.5 s. For the purposes of this study any rapid high temperature heating rate processes will be simply referred to as fast pyrolysis to contrast with slow pyrolysis which occurs when the heating rate is on the order of 20°C/s.

3.2. Methods

Soil samples were collected from the impact site in all four directions from the crater at various distances within and beyond the known shrapnel meteorite distribution; coordinates were recorded with a GPS device (Table 3-1). At each location a profile of the soil was exposed and a sample collected from the modern surface to a depth around 25 to 30 cm. Effort was made to keep the collected soil samples intact as a continuous profile and three samples were collected with Whitecourt meteorites in situ. In the lab small subsamples of soil were examined under a stereo microscope and any spherules identified were carefully removed with tweezers.

The small size and delicate nature of the spherules requires high resolution non-destructive characterization of their structure, in this case using a SkyScan 1172 micro-computed tomography (CT) scanner. To prepare the spherules for micro-computed tomography (micro-CT) scans they were mounted on small stands of soft colourless wax with as little of the spherule in contact with the wax as possible. For other analyses, some spherules were mounted in epoxy and polished by hand using wet to dry sandpaper and finished by using a grinding wheel with alumina suspended fluids. For comparison, a piece of charcoal and a frothy charcoal-like fragment that had been removed from examined soil samples were also mounted in epoxy. Epoxy mounted spherules were initially coated with carbon for analysis. Later this coating was removed and a thin coat of Cr was applied for electron probe microanalyzer (EPMA) analysis.

Table 3-1: Soil sample locations

Soil sample	Easting	Northing	Distance from crater (m)	Direction from crater	Meteorite depth (cm)	Meteorite mass (g)
1	591768	5984311	178	west	n/a	n/a
2	591950	5984488	170	north	n/a	n/a
3	591952	5984142	176	south	n/a	n/a
4	593125	5984189	1180	east	n/a	n/a
5	592521	5984292	574	east	10	38.7
6	592520	5984252	576	east	18	91.6
7	592150	5984398	218	northeast	7	8.9
8	591679	5983971	439	southwest	n/a	n/a
9	592553	5984760	750	northeast	n/a	n/a
13	594035	5984248	2000	east	n/a	n/a
14	591512	5983348	1000	southwest	n/a	n/a
15	591469	5984676	595	northwest	n/a	n/a
16	591436	5985186	1000	northwest	n/a	n/a
pit 1	591963	5984307	crater rim	east	n/a	n/a

A Zeiss EVO MA 15 scanning electron microscope (SEM) was primarily used to obtain backscattered and secondary electron images. Energy dispersive spectrometry (EDS) analyses were also utilized to provide semi-quantitative elemental data for determining the composition of the spherules. Once coated with Cr a JEOL 8900 EPMA was used to obtain wavelength dispersive spectrometry (WDS) quantitative analyses of the spherules. Analytical conditions operated at a 15 kV accelerating voltage and a 30 nA probe current. Analyzed elements and their standards were K (sanidine MAD), Na (tugtupite), C (diamond), Si (tugtupite), Mn (Mn Cu), Ca (dolomite BAY), Mg (dolomite BAY), O (Cr_2O_3), Al (tugtupite), Fe (Fe metal), P (apatite), and Ni (Ni metal). Sixteen spherules were cleaned then crushed into a powder using a mortar and pestle for analysis with a Rigaku Geigerflex Powder Diffractometer (XRD) by mounting on a zero-background plate. The powder was analyzed using both X-ray diffraction (XRD) and X-ray fluorescence (XRF).

3.3. Results

3.3.1. Distribution

The distribution of spherules seems to mirror the distribution of shrapnel fragments, but with a slightly wider dispersal, with the higher concentrations of spherules located downrange from the crater (Fig. 3-2). Carbonaceous spherule concentrations were determined by the number of spherules found per gram of soil examined. The dispersal of spherules does not cease at the edge of the known shrapnel distribution, but continues beyond this point. Spherules have been identified in soil at least 2 km east of the crater and 1 km away in both the northwest and southwest directions. The highest concentration of spherules detected was near the northeast corner of the protected zone with a concentration of 5.2 spherules per gram of soil. The spherule concentration decreases with increasing distance from the crater; the northwest and southwest directions have the lowest overall concentrations detected of 0.0 and 0.3 spherules per gram respectively. The distribution of spherules directly associated with meteorites is limited as their discovery occurred after the meteorites were processed, as they are easily removed. At least 92 meteorites are directly associated with having carbonaceous spherules adhered to their external weathered surface, which amounts to approximately 0.02% of documented meteorite finds. Looking at soil samples in 5 cm depth increments shows spherules are concentrated in the upper portions of the soil; 66% of spherules collected are found 0 to 10 cm below the surface.

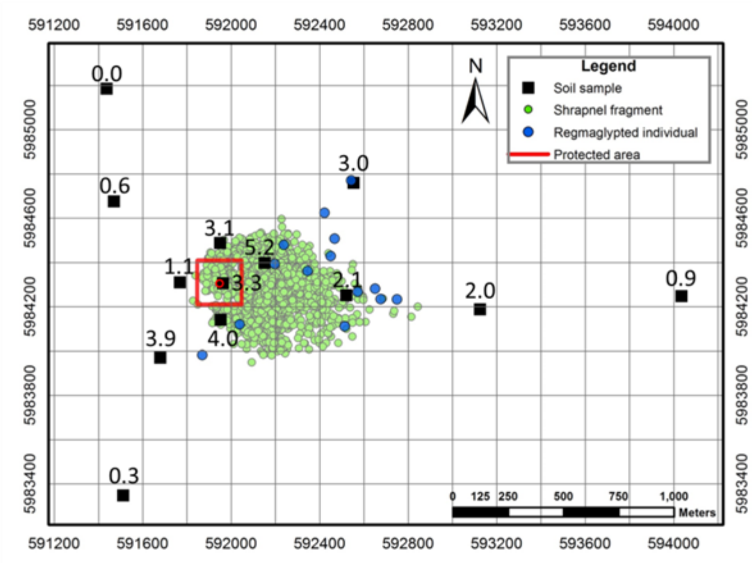

Figure 3-2: Soil locations and spherule concentration determined for each site. Values are given in # spherules/g. Crater location is indicated by red circle at the center of the protected area; grid spacing is 200 m.

3.3.2. Morphology and structure

Spherules range in size from about 0.1 to 1.5 mm in diameter. They are non-magnetic and highly spherical. The majority of spherules are black in colour with a small portion being darker brown (Fig. 3-3). A few of the collected spherules resemble perfect spheres while the rest have sphere-like shapes with rounded and smooth surfaces but additional small bumps or minor imperfections may exist on some surfaces. A small portion of the imperfect spherules have more pronounced features creating more complex shapes such as teardrops, rods, and fused spherules (Fig. 3-4). Fused spherules are the most common complex shapes where the two spherules may be of similar size or may be quite dissimilar in size but all complex shapes are considered to be rare in abundance. All spherules have highly porous interiors with isolated micropores, 8-20 µm in diameter, which are observable through SEM or EPMA imaging or by using micro-CT data.

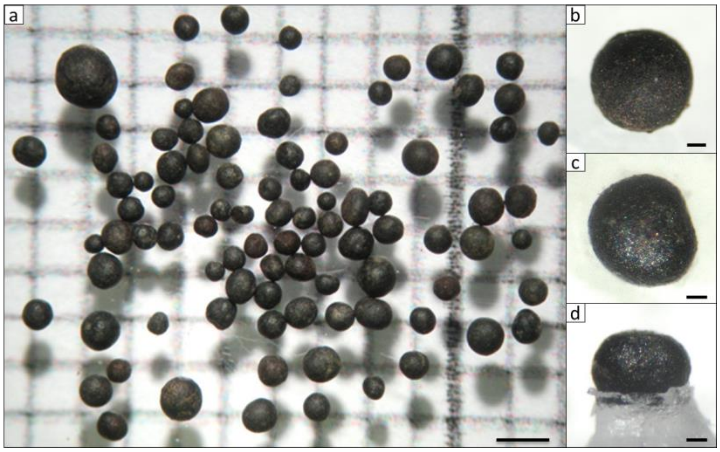

Figure 3-3: Typical carbonaceous spherule morphologies. (a) Group of spherules with sphere-like shapes including the largest spherule recovered with a diameter of 1.5 mm. [scale bar = 1 mm] (b) Top view of a spherule resembling a perfect sphere. [scale bar = 200 µm] (c) Top view of a spherule with minor imperfections to its overall shape. [scale bar = 100 µm] (d) Side view of the spherule in c) showing more of its oval shape; mounted on wax. [scale bar = 100 µm]

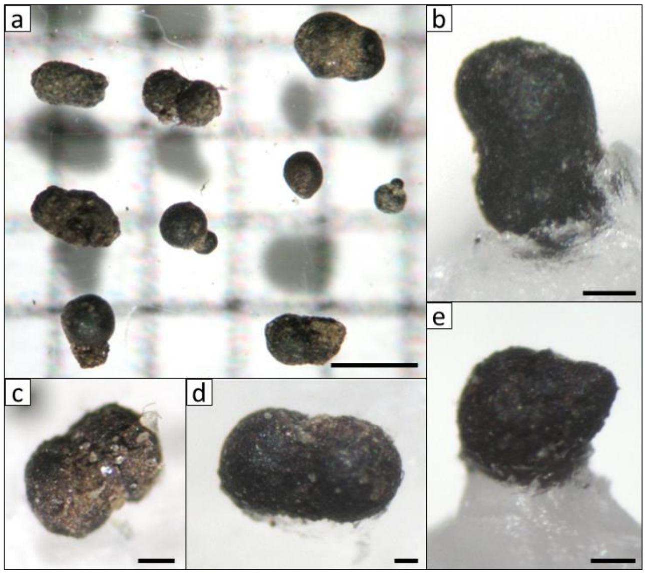

Figure 3-4: Complex carbonaceous spherule morphologies. (a) Group of rare forms including rods and fused spherules of varying sizes. [scale bar = 1 mm] (b) Rod-shaped spherule mounted in wax. [scale bar = 200 µm] (c) Fused spherules of similar size with terrestrial grains present on outer surface. [scale bar = 200 µm] (d) Another example of fused spherules of similar size and more fused together than in c). [scale bar = 100 µm] (e) Teardrop-shaped spherule mounted in wax. [scale bar = 100 µm]

Most spherules are less dense than water since they float when placed in water. Only a few spherules immediately sink in water and these tend to be very black and have a stronger structure that is more resistant to crushing. This contrasts with the less dense spherules which are more delicate and easily broken when a little pressure is applied. The dark brown spherules fall within the less dense category and are the easiest to crush. Structures of the high and low density spherules remain the same, where both have highly porous interiors with a less porous crust. Crusts with low porosity are common to all spherules but the thickness of the crust is not consistent, ranging from 5 to 65 µm (Fig. 3-5 and Fig. 3-6).

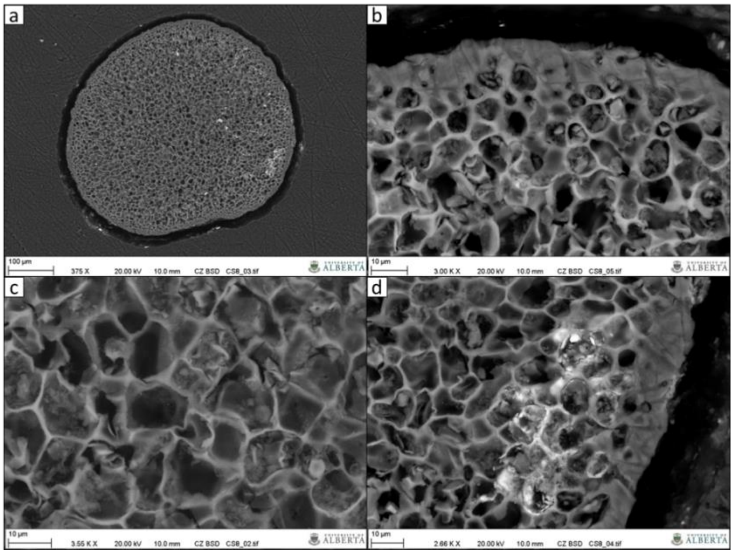

Figure 3-5: (a) Cross-section of the carbonaceous spherule shown in Figure 3-3c. (b) Thin crust along the top edge of the spherule. (c) Higher magnification of the spherule interior. (d) Lower right crust area. BSE images from SEM.

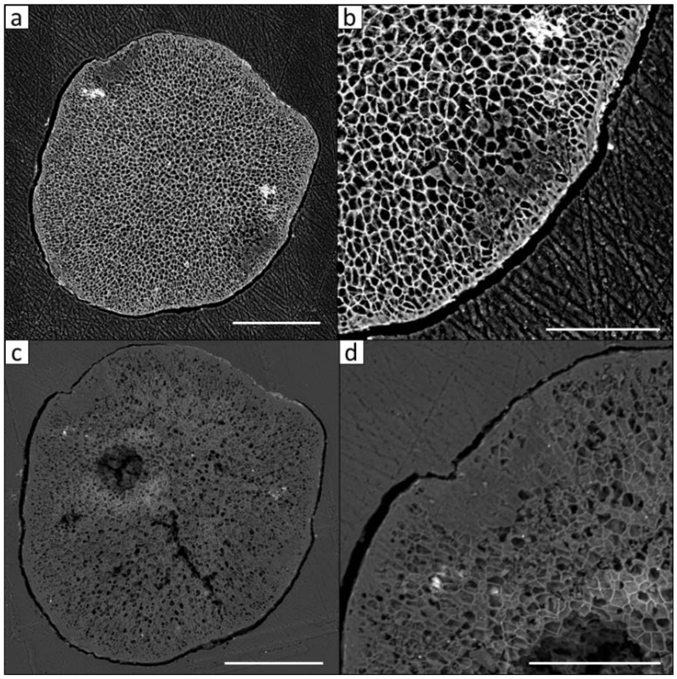

Figure 3-6: (a) Cross-section of a rod-shaped spherule. [scale bar = 200 µm] (b) Bottom right edge shows thin crust. Dark area is less porous than surrounding interior. [scale bar = 100 µm] (c) Same spherule as a) which now has a broken interior after a light re-polishing to remove C-coating before Cr-coating was applied. [scale bar = 200 µm] (d) Upper left edge with a thicker area of the crust with low porosity. [scale bar = 100 µm] Images are a combination of BSE and SE taken by an EPMA.

The high resolution of the SkyScan 1172 micro-CT acquired data show most of the scanned spherules have a similar internal morphology while several have a few additional features such as inclusions or enlarged pores (Table 3-2). Spherule size does not appear to cause any difference in the quality of the scanned data; diameters range from 0.259 to 1.161 mm. The crust thickness varies between spherules and is not always constant within a single spherule. The thickness of the crust cannot be determined by the diameter of the spherule or its shape so an imaging method is required to determine this characteristic. The high porosity of the spherules contributes to them being easily broken so micro-CT imaging is ideal to identify internal features. The cs11 spherule has a hollow upper half and retains enough of the porous interior in the bottom half to show its similarity to the completely porous spherules (Fig. 3-7). Spherule cs12 has a distinctive morphology of 11 enlarged pores ranging from 0.07 to 0.1 mm in diameter (Fig. 3-8).

Table 3-2: Descriptions of micro-CT scanned spherules[1]

Sample ID	Spherule height (mm)	Soil sample # removed from	Shape	Crust thickness	Additional features
cs1	0.870	2	sphere-like	thick	n/a
cs2	1.133	3	teardrop	thick	n/a
cs3	0.725	4	sphere-like	thin to med	n/a
cs4	0.815	1	rod	thin to med	enlarged pores (x6)
cs5 [L]	0.503	7	fused	thin	n/a
cs5 [R]	0.567	7	fused	thin	n/a
cs6	0.963	6	rod	thin	inclusions (x2)
cs7	0.978	7	sphere-like	med	terrestrial surface grains
cs8	0.463	7	sphere-like	thin to med	inclusions (x2)
cs9	0.664	1	sphere-like	thin to med	n/a
cs10	0.690	8	sphere-like	med	n/a
cs11	0.259	4	sphere-like	thick	partially hollow
cs12	0.878	3	sphere-like	thin to med	enlarged pores (x11)
cs13	0.528	3	sphere-like	thin	cracks, inclusions (x2)
cs14	0.799	5	sphere-like	med to thick	chip/void at surface
cs15	0.559	1	teardrop	thin	n/a
cs16	0.243	2	sphere-like	med	inclusion (x1)
cs17 [L]	0.479	unknown	fused	med	n/a
cs17 [R]	0.463	unknown	fused	med	n/a
cs18	1.161	8	sphere-like	med to thick	n/a

[1] determined using SkyScan's CT-Analyser and DataViewer programs

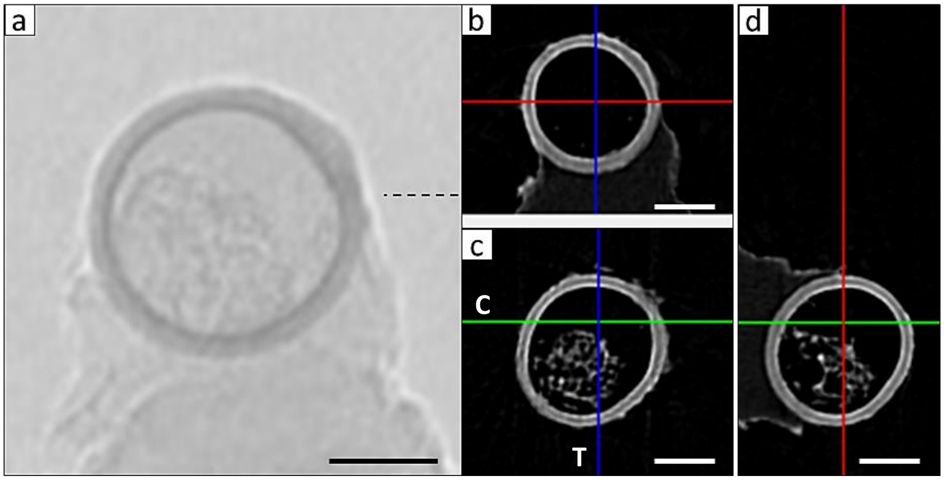

Figure 3-7: (a) X-ray transmission image of spherule showing a thick and dense crust of uneven thickness. Interior of spherule is partially hollow (upper half) and the rest is porous; mounted in wax. Dashed line indicates the position of the transaxial image. (b) Coronal view corresponds to the location of the green line (horizontal line C) in the transaxial image. (c) Transaxial view showing porosity as well as hollow areas; hollow area shows as black. (d) Sagittal view also shows porous and hollow areas and corresponds to the location of the blue line (vertical line T) in the transaxial image. Part a) image generated by SkyScan 1172 micro-CT scanner and part b-d) image series obtained using DataViewer program. [scale bars = 100 µm]

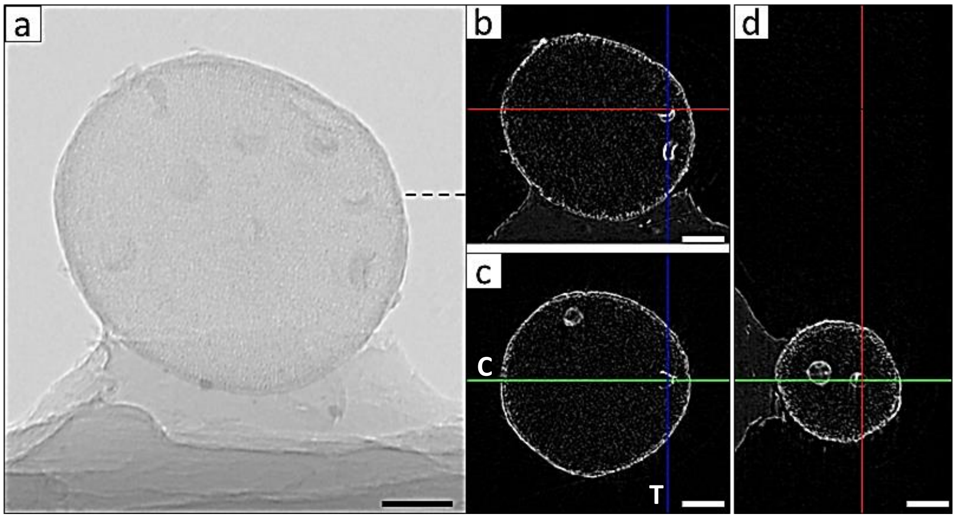

Figure 3-8: (a) X-ray transmission image of spherule with multiple enlarged pores and a relatively thin outer crust; mounted in wax. Dashed line indicates the position of the transaxial image. (b) Coronal view corresponds to the location of the green line (horizontal line C) in the transaxial image. (c) Transaxial view showing two of the eleven enlarged pores. (d) Sagittal view showing two of the pores and corresponds to the location of the blue line (vertical line T) in the transaxial image. Part a) image generated by SkyScan 1172 micro-CT scanner and part b-d) image series obtained using DataViewer program. [scale bars = 200 µm]

Charcoal is more common in some soil samples than others and are often confined to specific depths in the soil. Charcoal pieces range from 1 to 10 mm in length, are black in colour, slightly vitreous, and have a cellular structure (Fig. 3-9). Frothy charcoal-like samples are rare in the examined soil samples and are black, highly vitreous, brittle, and have a foam or bubble-like structure of large pores (Fig. 3-10). The few frothy samples found lack the characteristic cellular structure of the charcoal samples and are termed charcoal-like due to their similar colour, lustre, and brittleness as the charcoal pieces.

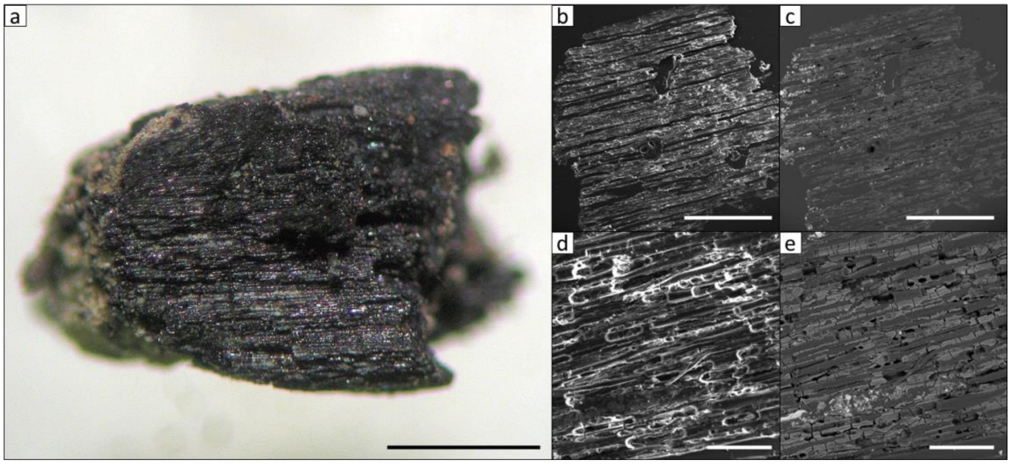

Figure 3-9: Representative piece of charcoal found in the soil surrounding the crater. (a) Charcoal is black and slightly vitreous with a cellular structure clearly visible. [scale bar = 1 mm] (b) Overview of a cross-section of the charcoal piece shown in a) taken using a combination of BSE and SE images. [scale bar = 1000 μm] (c) Same view as part b) but imaged using BSE only. [scale bar = 1000 μm] (d) Detail of charcoal plant structure with some cell structures visible; image taken using a combination of BSE and SE images. [scale bar = 100 μm] (e) Same view as part d) but imaged using BSE only. [scale bar = 100 μm]

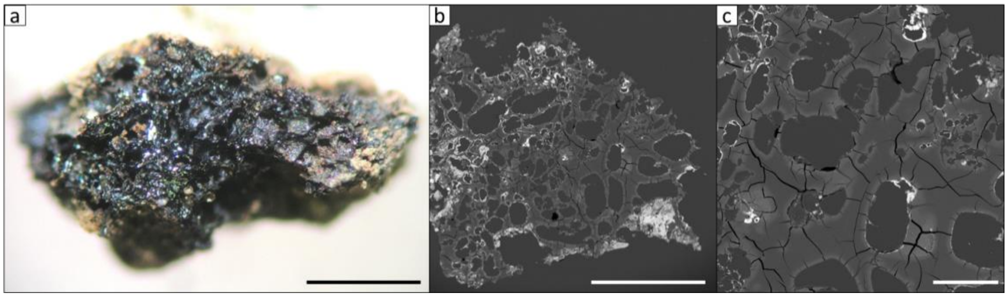

Figure 3-10: Rare piece of frothy charcoal-like material found in the examined soil surrounding the crater. (a) Highly vitreous and frothy charcoal-like fragment covered with soil and sand grains (light-coloured material). [scale bar = 1 mm] (b) Overview of a cross-section showing frothy nature of sample. [scale bar = 1000 μm] (c) Detail of frothy structure with prominent fractures throughout and between the pores, which are filled with epoxy. [scale bar = 200 μm] Part b-c) are BSE images.

3.3.3. Composition

Spherules removed from the soil are mainly composed of C and O with minor amounts of Ca, Al, Fe, and Mg. The composition is generally consistent within a spherule showing no compositional difference between the porous interior and thicker less porous crust. The crust composition for a given spherule is relatively constant but varies in average carbon content between spherules from 55.28 to 74.53 wt% (Table 3-3) The composition of a spherule (J527s1) found adhered to a meteorite was also examined. Its interior composition is similar to the spherules found in soil but with a lower C content and higher Fe, Ni, and Na. The totals for the three spherules removed from the soil (CS1, CS6, and CS8) and J527s1 indicate few, if any, volatiles present.

Table 3-3: Carbonaceous spherule compositions determined by electron probe microanalysis (EPMA)

sample	n	C (wt%)	O (wt%)	Ca (wt%)	Fe (wt%)	Al (wt%)	Mg (wt%)	Na (wt%)
CS1	6	68.94 ± 4.23[1]	30.20 ± 1.64	1.69 ± 0.17	0.03 ± 0.02	0.02 ± 0.01	0.10 ± 0.02	0.04 ± 0.00
CS6	5	74.53 ± 2.24	21.52 ± 2.24	1.05 ± 0.26	0.08 ± 0.07	0.05 ± 0.03	0.06 ± 0.01	0.05 ± 0.01
CS8	1	66.16	27.28	3.30	0.63	0.76	0.33	0.01
J527s1	7	55.28 ± 5.61	29.54 ± 3.74	0.53 ± 0.09	10.77 ± 4.33	0.72 ± 0.87	0.03 ± 0.01	0.33 ± 0.16
charcoal	3	43.83 ± 6.48	15.26 ± 5.64	2.99 ± 0.42	0.21 ± 0.02	0.36 ± 0.29	0.11 ± 0.06	0.04 ± 0.03
frothy-looking fragment	4	66.05 ± 0.71	17.44 ± 0.37	1.93 ± 0.05	0.04 ± 0.02	0.15 ± 0.12	0.05 ± 0.00	0.02 ± 0.00

sample	n	Si (wt%)	Mn (wt%)	K (wt%)	P (wt%)	Ni (wt%)	Ti (wt%)	Total (wt%)
CS1	6	0.01 ± 0.00	0.01 ± 0.00	0.06 ± 0.01	0.02 ± 0.01	0.00 ± 0.01	0.01 ± 0.00	92.92 to 102.99
CS6	5	0.04 ± 0.02	0.06 ± 0.08	0.04 ± 0.01	0.01 ± 0.01	0.01 ± 0.01	0.02 ± 0.01	92.89 to 103.14
CS8	1	0.12	0.01	0.03	0.21	0.01	0.02	98.97
J527s1	7	0.15 ± 0.07	0.00 ± 0.00	0.05 ± 0.01	0.01 ± 0.01	0.44 ± 0.19	0.04 ± 0.01	90.51 to 109.85
charcoal	3	0.10 ± 0.02	0.00 ± 0.01	0.07 ± 0.02	0.02 ± 0.01	0.00 ± 0.00	0.06 ± 0.01	48.18 to 76.02
frothy-looking fragment	4	0.02 ± 0.00	0.01 ± 0.02	0.04 ± 0.01	0.01 ± 0.01	0.00 ± 0.01	0.06 ± 0.01	84.89 to 86.38

[1] Average of n analyses with standard deviation provided

XRD was run to determine the crystallinity of the spherules. XRD analysis only identified the minerals birnessite, quartz, albite, sanidine, and siderite. Peaks for carbon associated with graphite or other crystalline carbon forms are absent; however there is a bump in the spectrum corresponding to glass, indicating that the spherules are amorphous (Fig. 3-11).

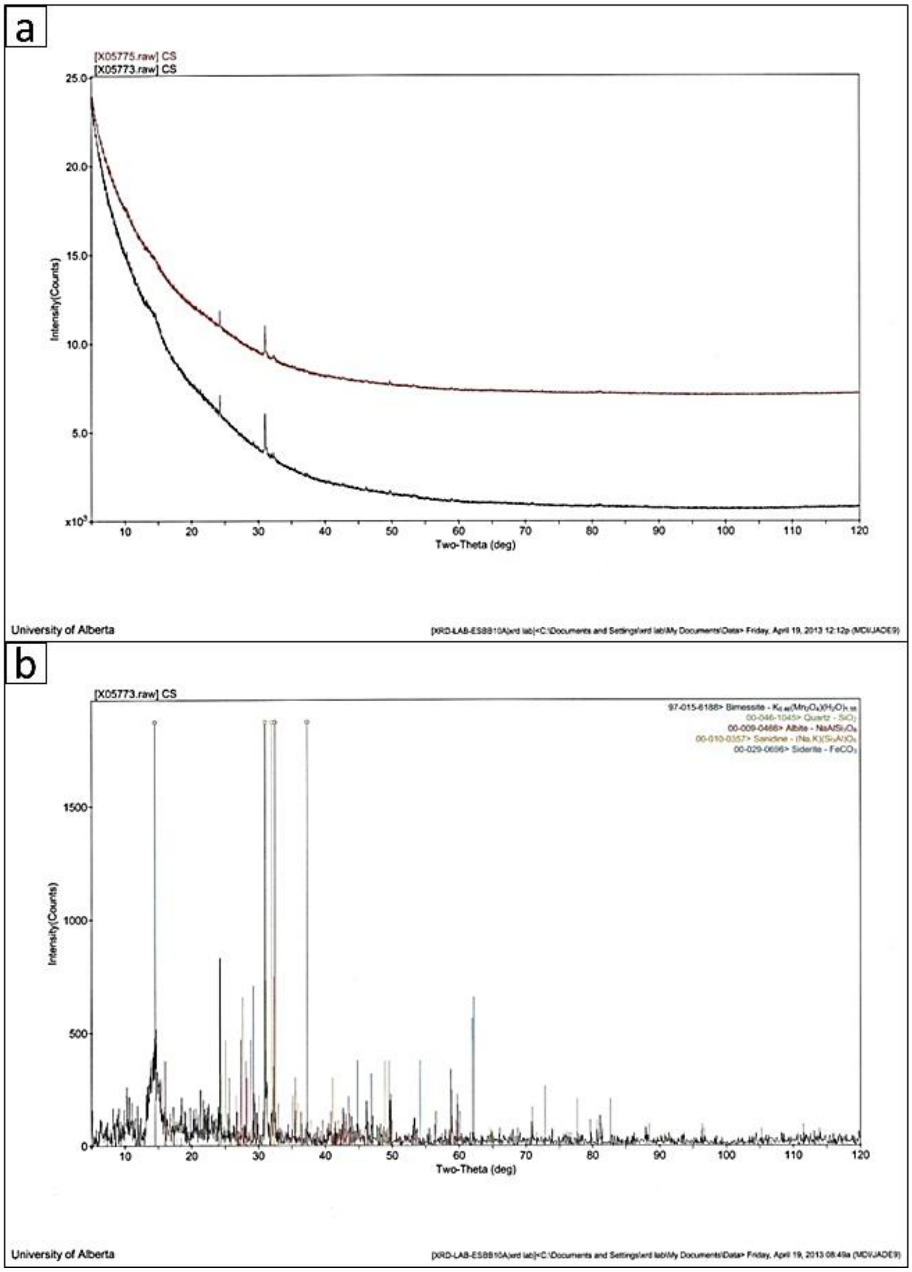

Figure 3-11: Results of the XRD analysis of a group of 16 carbonaceous spherules removed from soil samples. (a) Comparison of two analyses on the same sample first by XRD (black-lower line) then by XRF (red-upper line). (b) Minerals present in sample as determined by XRD.

Several potential inclusions within the spherules were identified after reviewing the micro-CT data (Fig. 3-12). The inclusions inside the spherules appear similar in size and density to silicate grains present on the outer surface of several scanned spherules (e.g. Fig. 3-4c). Two of these spherules were mounted in epoxy with the goal being to grind the spherule to expose the inclusion in situ and then determine its composition. Unfortunately the delicate structure of the spherules could not keep the inclusions in place and they were plucked out and lost. There was one small scanned spherule that had a grain partially embedded in the spherule's outer crust which was visible upon closer examination with a stereo microscope. After observing the presence of these grains in the micro-CT data undamaged spherules were broken to locate additional grains to investigate further. Nine grains recovered from the spherules were found to be silicate in composition. Each grain has a different appearance and range in size from 48 to 160 µm (Fig. 3-13). The grains are translucent and mostly colourless with three grains being slightly yellow or orange in colour.

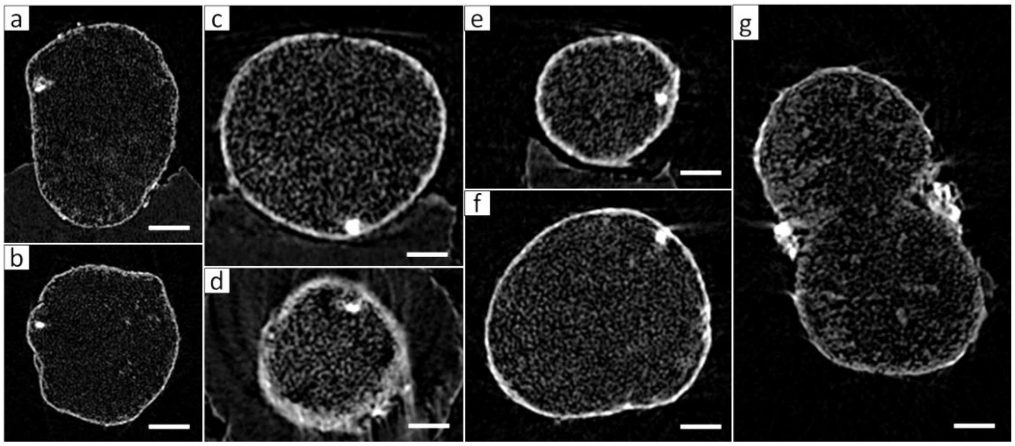

Figure 3-12: Inclusions within spherules identified using micro-CT data. (a) Rod-shaped spherule with an inclusion (bright spot along upper left side of spherule). (b) Different view of the same rod-shaped spherule as in part a) showing inclusion. (c) Inclusion located near the bottom of a spherule with minor imperfections to its shape (also see Figure 3-3c-d) for other views of this spherule). (d) A different view of inclusion shown in c). (e) Another inclusion within the same spherule as in c-d). (f) Alternate view of the second inclusion from e) found in this spherule. (g) Fused spherules with sand-like grains on its exterior surface for comparison to the inclusions identified within other spherules. All images obtained using DataViewer and part a) and c) are coronal views, part e) is a sagittal view, and part b), d), f), g) are transaxial views. [scale bars = 200 µm in a-b) and 100 µm in c-g)]

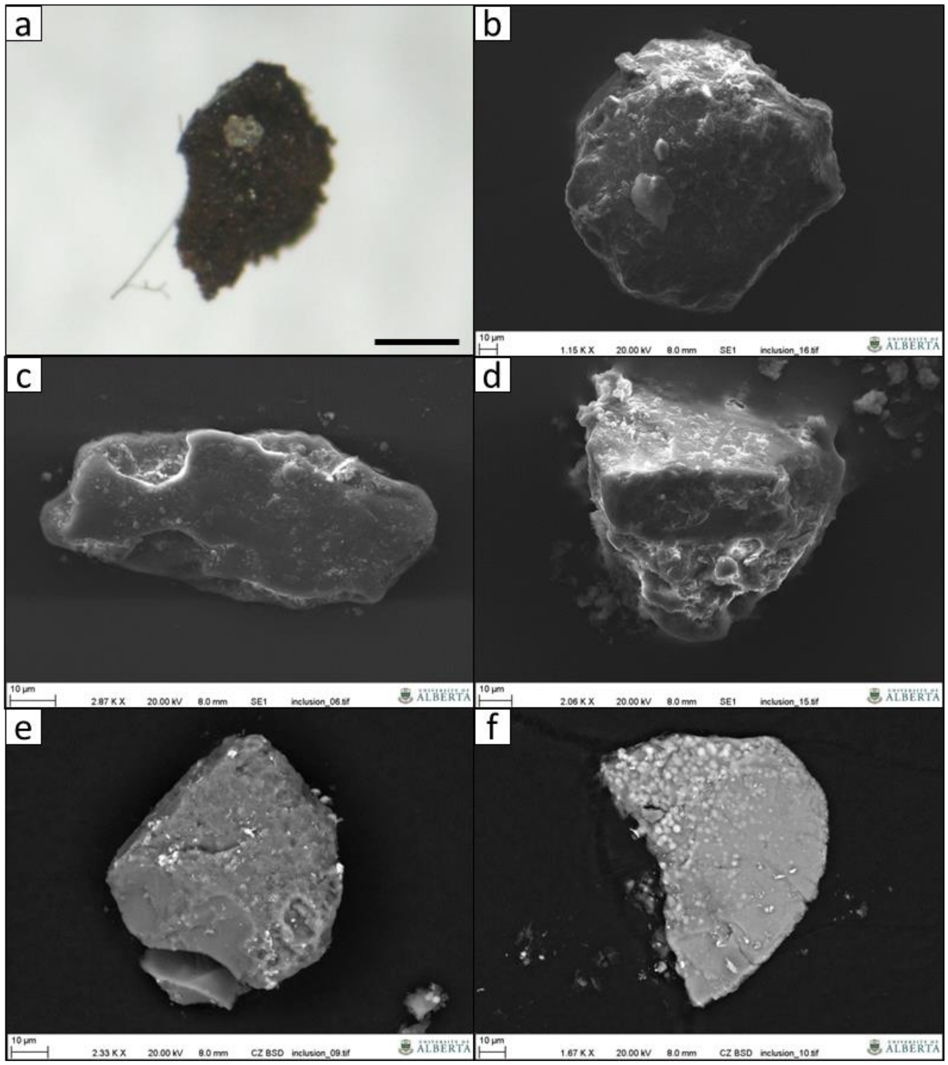

Figure 3-13: Inclusions removed from spherules. (a) An in situ inclusion in a small piece of a carbonaceous spherule that was broke open. [scale bar = 500 µm] (b) Same inclusion as shown in a) which was the largest inclusion found. (c) A flat elongate inclusion. (d) A thick tapered inclusion. (e) A small, flat, and partially fractured inclusion. (f) Another thin flat inclusion. Part b-d) are SE images and e-f) are BSE images obtained using SEM.

3.4. Discussion

3.4.1. Distribution

The distribution of amorphous carbonaceous spherules identified in soil samples from 12 key locations around the WMIC show some similarity with the shrapnel-shaped meteorite fragments. No correlation with the regmaglypted individual (RI) distribution was observed. Both the spherules and shrapnel originate from the crater and like the shrapnel the spherule distribution is not uniform in all directions. Over half of the spherules collected from the soil samples are found 0 to 10 cm below the modern soil surface, which is a similar depth from where many of the meteorite shrapnel fragments have been recovered. Similar to the shrapnel the direction with the farthest sample is east of the crater with few found west of the crater. With only a dozen locations examined minor fluctuations and precise contours within the distribution cannot be determined; however, other information such as extent can be resolved from these data. The low density of the spherules would have permitted them to be suspended in the air longer and therefore be transported further away from the crater. The limit of spherule distribution may represent the extent of the expansion plume created by the impact (Artemieva and Pierazzo, 2011). Spherules would have been dispersed following the advance of the shock wave and the winds generated by the impact (Kring, 1997). Other spherules would have been directed upward by the impact and more gradually dispersed from prevailing winds of the area, which are from the west. Kring (1997) investigated the parameters of the air blast that would have been generated from the collision that created Barringer Crater in Arizona and found they likely exceeded hurricane force winds at around 260 km h^{-1}. The Barringer Crater collision was much larger than Whitecourt, having a diameter of 1.18 km, but the effects following the event would be expected to be similar on a smaller scale.

3.4.2. Morphology

The high sphericity of the carbonaceous spherules suggests that they were molten at one point during their formation. Comparisons of the carbonaceous spherules to microtektites can be made in regards to the shapes formed. Microtektites are impact-generated spherules which are generally <1 mm in diameter and spherical in shape (Glass and Simonson, 2012) with some having similar shapes as the carbonaceous spherules e.g. Australasian microtektites and Darwin glass (Cassidy et al., 1969; Howard, 2011). The majority of both spherule types are sphere-shaped with less common rotational forms generated; rotational forms of microtektites include teardrops, dumbbells, and discs (Glass and Simonson, 2012). The teardrop-shaped carbonaceous spherules are the most similar rotational form to microtektites. The rod-shaped and fused spherules are the most comparable to the microtektite dumbbell form, with minor variations; rods lack the slight pinching in the middle and the fused spherules are not quite as elongated as the dumbbells. The fused spherule shape is where two spherules have combined in the molten state, as opposed to a large piece being stretched apart by rotational forces. Plasticity of their respective compositions may also be a factor of the resulting shapes. For the fused carbonaceous spherules most of the original spherule shape remains intact with only one side of the two spherules merging. In order for this shape to form, the two spherules would need to make contact shortly after their formation, while both spherules are still at least partially molten. Micro-CT data shows a continuous porous interior between the centers of both spherules (Fig. 3-12g), with a non-porous crust along the exterior surface of both spherules, further supporting this contention.

3.4.3. Composition

Carbonaceous spherules that were directly removed from the soil (CS1, CS6, and CS8) have an average composition of 70 wt% C and 26 wt% O (Table 3-3). The composition varies slightly between spherules indicating there could have been a variation in the source composition or variation during the formation process. The most probable carbon source for the carbonaceous spherules is the biomass present at the crater's location at the time of impact. The compositional analysis also included a spherule (J527s1) that was adhered to the external surfaces of a shrapnel meteorite fragment. This meteorite-adhered spherule showed a higher Fe and Ni content than any other soil removed spherule, which corresponds to its proximity to the weathered external surface of Whitecourt meteorites. Prolonged contact with weathered meteorites apparently leaches FeNi oxides into the spherule over time. Backscattered electron images show the outer pores the meteorite-adhered spherule filled with oxides (Fig. 3-14).

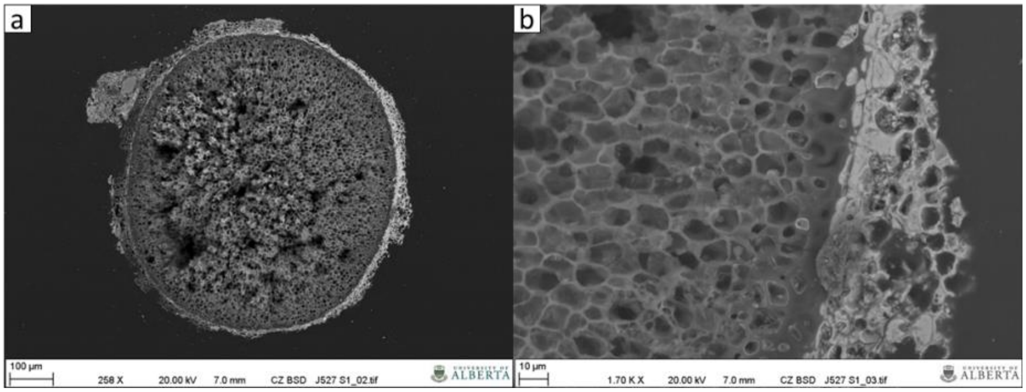

Figure 3-14: Spherule removed from weathered meteorite rind; right side was adhered to meteorite. (a) Cross-section of spherule with slightly broken interior. (b) Higher magnification of outer crust along the right edge in the center.

The grains removed from broken spherules had silicate compositions with no apparent shock features. Minor variation in the colour of inclusions is likely due to a higher portion of iron resulting in an orange colour; viewed under normal light conditions the inclusion shown in Figure 3-13f is a translucent orange colour, and is likely feldspar.

The average carbon content reported for various tree and plant matter is 50 wt% (Table 3-4). There is not a noticeable difference in major elemental compositions between hard and soft wood and the similarity in bulk composition between species are likely due to the homogeneity of components such as cellulose and lignin. The high carbon content in the Whitecourt spherules' composition suggests there is a connection with biomass. The closest carbon value from Table 3-4 that matches the Whitecourt spherules is charcoal. The carbon content of the Whitecourt charcoal and frothy fragment gave the poorest totals (Table 3-3); the cellular structure of the charcoal did not provide a wide enough area for a proper analysis and the more consistent totals for the frothy fragment suggest the presence of volatiles. The frothy fragment has no biological structure and is relatively featureless except for fractures and 20 to 400 µm sized pores throughout its structure (Fig 3-10). Neither the charcoal nor frothy fragment found in the soil around the crater are identical morphologically to the carbonaceous spherules as significant differences exist between them.

Table 3-4: Carbon content and composition for assorted vegetation and other carbon-rich objects

	C (wt%)	O (wt%)	H (wt%)	N (wt%)	S (wt%)	Other (wt%)	Reference
Vegetation sources							
soft wood	40-45	n/a	n/a	n/a	n/a	55-60 (volatiles)	Rodriguez-Reinoso (2002)
hard wood	40-42	n/a	n/a	n/a	n/a	55-60 (volatiles)	Rodriguez-Reinoso (2002)
radiata pine	49.3	45.2	6.42	0.04	0.09	n/a	Cetin et al. (2005)
pine	49.7	43.5	6.3	0.1	0.0022	n/a	Dall'Ora et al. (2008)
beech	49.5	43.4	6.1	0.13	0.0011	n/a	Dall'Ora et al. (2008)
beech	50.8	42.9	5.9	0.3	0.02	n/a	Septien et al. (2012)
poplar	48.4	45.2	5.9	0.07	n/a	n/a	Piskorz et al. (1986)
Pinus sylvestris	52.2	41	6.3	0.5	n/a	n/a	Luik et al. (2007)
grape seed	49.7	42.9	5.9	1.4	0.07	n/a	Jimenez-Cordero et al. (2013)
Carbon-rich objects							
sclerotium grains	47.6	30.2	3.32	0.79	n/a	11.6 (ash), 6.57 (water)	Watanabe et al. (2007)
charcoal	60-90	n/a	n/a	n/a	n/a	n/a	Scott (2010)
soft coal	65-80	n/a	n/a	n/a	n/a	20-30 (volatiles)	Rodriguez-Reinoso (2002)
hard coal	85-95	n/a	n/a	n/a	n/a	5-10 (volatiles)	Rodriguez-Reinoso (2002)
YDB spherules	>75	n/a	n/a	n/a	n/a	n/a	Firestone et al. (2007)
YDB carbon spherules (from Carolina Bay)	86	n/a	5.6	1.9	0.4	2.3 (SiO_2), 2.1 (Al_2O_3)	Firestone (2009)
YDB glass-like carbon (From Carolina Bay)	90	n/a	3	0.66	0.03	2.1 (SiO_2), 1.0 (Al_2O_3)	Firestone (2009)
carbon spherules	>87	n/a	n/a	n/a	n/a	(minor Si, Al, Fe)	Israde et al. (2012)

Charcoal forms from the incomplete combustion of plant matter, often during wildfires, and the charring process preserves the plant's anatomy (Scott, 2010) and cellular structure, which is clearly visible in BSE imagery (Fig. 3-9e). The frothy charcoal-like fragment has a porous or foam-like morphology but its pores are much larger and lack an overall spherical shape compared to the spherules. Charcoal, which is charred biomass, would have had a starting composition similar to the vegetation sources in Table 3-4 showing that a heating event such as a wildfire increases the carbon content. In an experiment studying the structure and morphology of chars from grape seeds, an increase in temperature resulted in an increased carbon content in the char (Jimenez-Cordero et al., 2013); the starting material had a carbon content of 50 wt% and rose to 90 wt% by the final temperature level of 1000°C. Char is the solid residue left after the thermal decomposition (pyrolysis) and loss of gases of biomass (Pyne, 1984; Scott, 2010). As the temperature rises the carbon content increases as volatiles are released and the overall char yield decreases (Jimenez-Cordero et al., 2013). The heating process of the grape seeds created a low density carbon foam-like material which replaced the albumen and embryo of the original seed due to their high volatile content (Jimenez-Cordero et al., 2013). Since spherules lack the same cellular structure and plant anatomy preserved in charcoal the heating event is not simply a wildfire. The range in carbon content of the spherules may represent different temperatures experienced since there is not as much variation in C wt% within the same spherule as there is between them (Table 3-3). The elevated carbon content of the carbonaceous spherules are worth noting since most vegetation has about 50 wt% C or less, indicating a high temperature heating event has likely taken place.

3.4.4. Potential non-impact origins for carbonaceous spherules

Potential non-impact origins of the carbonaceous spherules, with various degrees of plausibility, based on size and find locations, include pollen grains, fungal sclerotia, volcanic accretion lapilli, and fly ash (Table 3-5). Fly ash (Fig. 3-15a) is a product of coal combustion and is usually found as small, mainly spherical, particles 10-100 µm in size, and variable in colour: tan, brown, dark grey or black colours are possible depending on chemical composition (American Coal Ash Association, 2003). Fly ash is composed of silicon, aluminum, iron, and calcium oxides with minor amounts of magnesium and sulfur (American Coal Ash Association, 2003). Fly ash may be common in industrial areas, which are common in Alberta, but their nearly carbon-free composition rules them out as a source of the carbonaceous spherules found at the WMIC.

Pollen is another type of small particle commonly found in vegetated areas. Pollen ranges in size from 5-200 µm with most falling between 20-50 µm and have intricate shapes and surface structures (Kapp, 1969). Pollen usually have apertures in their outer surface either as grooves or pores of varying shapes which are used in identification (Fig. 3-15b,c). Spines may also protrude from the surface of some pollen. The overall shape of pollen grains is typically ellipsoidal but some may be spheroidal, oblate, or further divided into lobes. Pollen also have

Table 3-5: Terrestrial spherule features and compositions

Spherule type	Size (µm)	Shape	Interior	Colour	Primary composition	Magnetic	Reference
fly ash	10-100	spherical	solid	tan, brown dark grey, black	silicate	no	American Coal Ash Association (2003)
pollen	5-200	ellipsoidal, spheroidal, oblate; most have furrows/pores in exine	n/a	varies (brown, yellow, green, orange)	carbonaceous/ organic	no	Kapp (1969)
fungal sclerotia (*Sclerotium* spp.)	73-2000	spherical	densely packed hyphae/fibres	black, brown	carbonaceous/ organic	no	Watanabe (2010)
fungal sclerotia (*Cenococcum geophilum*)	1000-2000	spherical	thick transverse wall with hollow center	black	carbonaceous/ organic	no	Watanabe et al. (2006)
accretionary lapilli	2000-10000	spherical	concentric layers	light brown-grey	silicate	no	Moore and Peck (1961)

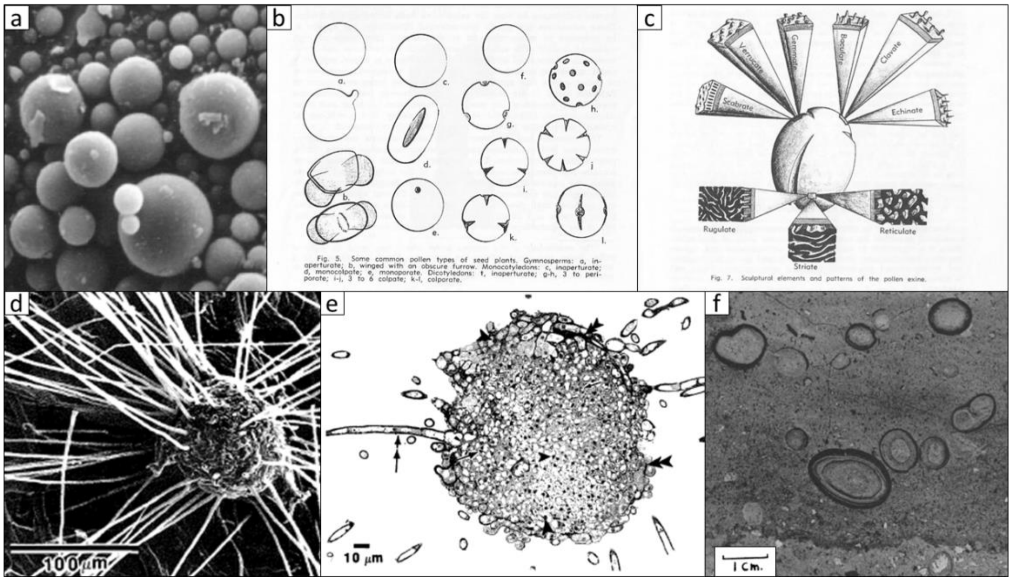

Figure 3-15: (a) Fly ash particles at 2000x magnification. [from American Coal Ash Association, 2003] (b) Common pollen types. (c) Various patterns of pollen outer walls (exine). [(b-c) from Kapp, 1969] (d) Sclerotium outer rind with radiating hyphae. (e) Transverse section of a sclerotium with hyphae. [(d-e) from Massicotte et al., 1992] (f) Accretionary lapilli showing concentric layers. [from Moore and Peck, 1962]

well-defined layers found in their outer wall which appear to be absent in the carbonaceous spherules, as well as apertures or spines. Diverse vegetation is present in the Whitecourt area; however, the absence of specific structures indicative of pollen eliminates it as a source for the carbonaceous spherules.

Fungal sclerotia are also common in forest soils and fall within the same size range as the carbonaceous spherules of about 70-2000 µm, depending on fungal genus (Table 3-5). Sclerotia morphology ranges from having a hollow center to an interior densely packed by hyphae, surrounded by a hard resistant shell (Watanabe et al., 2007; Watanabe, 2010). Some sclerotia have filamentous hyphae connected to the external surface (Fig. 3-15d,e), sometimes creating a hyphal mat containing multiple sclerotia (Massicotte et al., 1992). Their C content (about 48 wt%) is very similar to the vegetation sources given in Table 3-4 and are not amorphous which separates them from having a similar composition to the spherules. Watanabe et al. (2007) characterized major and trace elements in sclerotia and did not detect any silicates within the fungal structures; major elements included C, H, N, O, and Al and trace elements of Ti, Cr, Mn, Cu, Zn, Br, and Pb. Even though the colour and size of the fungal sclerotia are similar to the carbonaceous spherules found near the WMIC, their lower C content, differing morphologies, and the lack of silicate inclusions can rule this out as an origin.

A fourth type of spheroid found in some volcanic pyroclastic flow and surge deposits is accretionary lapilli (Fig. 3-15f), which are small volcanic ash and mud pellets which often have concentric layers visible in cross-section (Moore and Peck, 1962). Accretionary lapilli located more proximal to the volcano have concentric layers, or rims, while more distal lapilli have a distinct core without rims (Schumacher and Schmincke, 1991). Most of these lapilli are 2-10 mm in diameter with some rock fragments and volcanic glass scattered throughout the matrix (Moore and Peck, 1962). The interiors of lapilli vary as some have a more vesicular texture while others are denser. Accretionary lapilli form during volcanic eruptions where there is abundant ash, mud, and water vapour and within pyroclastic flows. These components become entrained in pyroclastic flows and the layers accrete, similar to hailstones, where movement through different parts of the flow have slightly different compositions (Moore and Peck, 1962; Schumacher and Schmincke, 1991). The composition of lapilli in each deposit is specific to the source volcano so variations between each location would exist. However, accretionary lapilli are mainly siliceous and contain very little to no carbon, so these are quite dissimilar to the carbonaceous spherules. Furthermore, there is no current or past source for these accretionary lapilli in the target material of the WMIC.

The most obvious comparison is to the carbon spherules associated, by some, with the Younger Dryas Boundary (YDB). A key difference is that Whitecourt spherules can be directly linked to an impact site while the YDB event has not been localized within North America. The scale of the two events differs with Whitecourt being limited to the crater impact site whereas the YDB event is proposed to have distributed material across North America and possibly Europe as well (Firestone et al., 2007). The size, colour, interior porous structure, and composition to some extent is similar in both cases (Fig. 3-16) but there has not been a report of terrestrial silicate grains being found within the YDB spherules like those found in Whitecourt spherules. The concentration of spherules is higher for the Whitecourt site than the YDB values; highest Whitecourt concentration is 5.2 spherules/g and the peak YDB concentration is 0.68

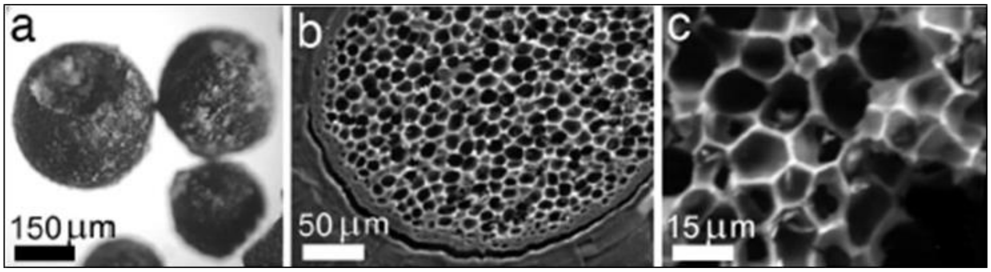

Figure 3-16: Younger Dryas Boundary spherules. (a) Whole spherules. (b) Cross-section of one of a carbon spherule. (c) Higher magnification of internal structure. [from Firestone et al., 2007]

spherules/g (Israde-Alcántara et al., 2012). A piece of glass-like carbon from the YDB layer at Carolina Bay appears similar to the frothy charcoal-like fragment found in the Whitecourt soil. The origin of the glass-like carbon sample (Fig. 3-17) from Carolina Bay is proposed to be from a high temperature shockwave that only affected one side of this sample; the non-thermally decomposed portion of the wood was identified as Yellow Pine (Firestone, 2009). With only one comparable sample from Whitecourt further testing would be necessary to determine if the frothy sample is truly glass-like carbon. Glass-like carbon is not naturally produced and it is argued that it would need temperatures around 3200°C to thermally decompose the cellulose with a slow heating rate is 20°C/min (Kaburagi et al., 2005; Firestone, 2009). The rate of heating could play a more important role on biomass rather than the maximum temperature as other studies have demonstrated, and is discussed in more detail in section 3.4.6 below. Some similarities between YDB carbon spherules and glass-like carbon exist but further examination of both would be required for a definitive conclusion. Both cases employ an impact (Whitecourt) or supposed impact (YDB) origin but to generate the YDB spherules a wildfire is stated as the heating source, which has its problems, as noted in Chapter 1 and discussed in section 3.4.6, so a common origin remains unclear.

Figure 3-17: Piece of glass-like carbon recovered from the YDB layer at Carolina Bay. The bottom portion of sample has not been thermally decomposed and is identified as Yellow Pine. Scale of this piece is not provided but pieces up to several cm in diameter are reported found. [from Firestone, 2009]

3.4.5. Terrestrial impact processes

An impact on Earth involving an iron projectile has not been directly observed in modern time and as a result the immediate effects that accompany such an event are not precisely known. In spite of diverse target environments on Earth, some common features among impact craters are expected. The impact that created the WMIC was small but still produced an explosive event, which would be common to all hypervelocity impacts. The Whitecourt explosion was catastrophic to the iron impactor which fragmented on impact and was energetic enough to scatter shrapnel-shaped shards to at least 900 m eastward of the crater.

Artemieva and Pierazzo (2011) modeled the Barringer crater impact and found fragments centimeter to decimeter in size become engulfed in the expanding plume with the highest concentration located in the downrange direction. This distribution is comparable to the data acquired for Whitecourt meteorites where most shrapnel fragments are located downrange and very few have been recovered uprange of the impact (Fig. 3-2). Metallic iron spherules are also found around Barringer crater, which differ from Whitecourt spherules as they were initially molten droplets of impactor material rather than molten biomass. Spherule dispersion was also modeled by Artemieva and Pierazzo (2011) which showed the same trend direction-wise but with an overall wider dispersal relative to the shrapnel. The Whitecourt spherules have a wider relative areal distribution when taking into account the size of the crater relative to the distal extent of Barringer spherules due to their differences in density. The less dense Whitecourt spherules could be carried farther and higher to be dispersed by both impact generated winds as well as by local prevailing winds.

The young impact age for the Whitecourt crater dictates that the climate and landscape at the time would have been similar to the forested landscape that is presently found. Therefore, there is a strong possibility the impact occurred during at a time when there was a high amount of moisture present. Modeling by Artemieva and Pierazzo (2011) show that an impact into a water-saturated target has the potential to produce a more intense impact. Howard (2011) discusses the effect a water-rich surface layer has on impact melt formation and why its presence can explain how a small simple crater can produce more melt than a larger complex crater. Howard also points out that theoretical studies indicate an impact into ice would generate melt and vapour an order of magnitude higher than an equivalent sized impact into a non-frozen target. Winter conditions, including snow cover and frozen ground, are present in the Whitecourt area for up to 6-7 months of the year which would increase the moisture content and the potential for volatile production at the time of impact. Even though there has not been a lot of melt products found around the Whitecourt crater, an increase in volatile production resulting from the presence of snow and ice could increase the explosiveness of the impact by increasing the size and the distance the impact plume expands to. The scale of craters examined by Howard (2011) is kilometers in diameter; however, similar reasoning could be used to not only explain the wide distribution of spherules but also the shrapnel meteorite distribution at Whitecourt.

Age may be a determining factor in locating carbonaceous spherules around terrestrial impact craters as the carbon could breakdown over time. Where an impact occurs is likely a prime factor in determining if carbonaceous spherules are even generated. If an impact occurs in an arid desert environment there is not a significant source of vegetation, and therefore carbon, from which the spherules can be generated. The recently-discovered 47 m diameter Kamil crater in Egypt was generated by an iron meteorite impact and no carbonaceous spherules were reported from this site (D'Orazio et al., 2011). Impacts in forested areas such as the Whitecourt area are ideal locations for having the necessary precursors for carbonaceous spherule generation due to the high amount of biomass present. A final factor related to carbonaceous spherules does not relate to crater-forming conditions but rather to post-impact conditions. A well-preserved crater is required to keep the delicate carbonaceous spherules intact if all other necessary conditions for their formation were met. This would not only include low anthropogenic ground disturbance but favourable chemical and mechanical weathering conditions as well.

3.4.6. Whitecourt carbonaceous spherule formation

Since carbonaceous spherules have not been reported as being directly associated with any other terrestrial impact crater, their formation process in relation to the Whitecourt crater is proposed here. The formation process is based on experimental studies that obtained products and structures that are comparable to what is observed with the Whitecourt spherules. Experimental studies have not yet produced spherules completely identical to Whitecourt as small-scale simulations of the conditions created during this low-energy hypervelocity impact would be difficult to re-create especially since the exact, but presumable, conditions of high temperature, pressure, and heating rate of the impact are not precisely known. Nevertheless, rapid heating was one of the main factors explored by Cetin et al. (2004), Dall'Ora et al. (2008), Kurosaki et al. (2008), and Commandré et al. (2011) in their pyrolysis experiments. Cetin et al. (2004) found that high heating rates removed any trace of a former cell structure. The cell structure no longer exists because of the transition of the biomass particles through a liquid state before devolatilization of the melted particle occurs. Cetin et al. (2005) looked at the effects of pressure on pyrolysis of their biomass particles. They were able to video capture the transition of their particles into the liquid phase at 1 and 20 bars and observed that at 1 bar the molten spherical droplet ruptured with the release of volatiles whereas no rupturing occurred at higher pressure (Fig. 3-18). Using a drop tube furnace chars produced at 1000°C with a high heating rate of 10^4 to 10^5°C/s demonstrate that even at short residence times melting still occurs (Cetin et al., 2005). Pressure may have played a role in the formation of the Whitecourt spherules in a similar manner. Preventing the catastrophic release of volatiles as observed in the experiment at

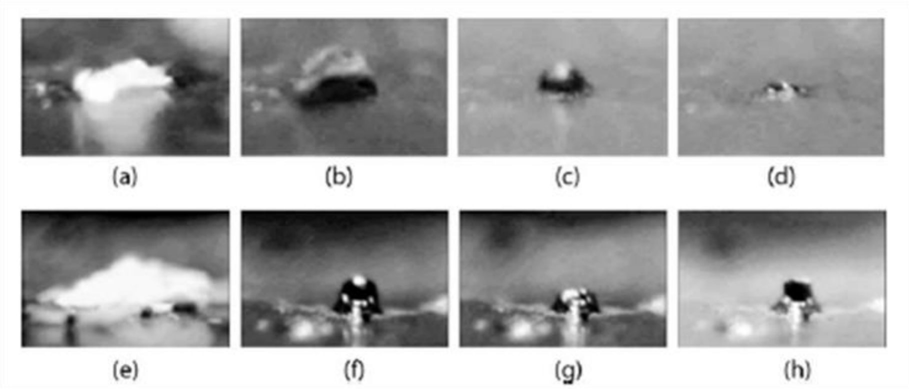

Figure 3-18: The formation of a liquid intermediate is a crucial step in fast pyrolysis as the liquid phase is responsible for the loss of cell structures and resulting amorphous state. Part a-d) 300°C/s at atmospheric pressure and part e-h) 300°C/s at 20 bar. Size of particles in a) and e) are approximately 300 µm. [from Cetin et al., 2005]

atmospheric pressure by Cetin et al. (2004) is required for forming the Whitecourt spherules since they are found intact and not in a ruptured state. This was likely accomplished by the increased pressures associated with an impact event counteracting the outward force of volatiles within the droplets; alternatively, molten spherules were quenched rapidly enough by their ejection from the crater that the volatiles did not have a chance to escape. In either case rapid quenching would be expected and would support the preservation of the smooth spherical nature of the carbonaceous spherules. Rapid quenching of molten droplets would inhibit the formation of the complex teardrop shape as rotation or high speed would be necessary to preserve its form as it is quenched. An area with a large quantity of spherules generated would be more likely to see a higher number of the fused shape form since the two spherules would be quenched at nearly the same time and could even be slightly adhesive as they cool, further increasing the odds of remaining fused. Spherule quenching may be the reason why there is a thickened crust on the spherules as the outer surface would have cooled first, preventing the escape of volatiles and preserving the interior porous structure observed. Some spherules may have ruptured but without a thickened crust to protect the delicate framework they are unlikely to be preserved. Several spherules examined with the micro-CT scanner display larger pores or are nearly hollow; these uncommon features make the spherules more delicate and less likely to be preserved. Another observation by Cetin et al. (2004) was that the spherical particles could grow to a larger size when increased pressure was applied as opposed to particle formation at atmospheric pressures. The amount of moisture present in the biomass does not influence the amount of gases produced during pyrolysis (Commandré et al., 2011). If this was a factor then it could have made a difference for the Whitecourt impact as seasonal changes in the moisture content of biomass exist. Dall'Ora et al. (2008) looked at the effect temperature had on the morphology of their spherical char particles and found that changing the pyrolysis temperature did not affect morphology and all their particles were spherical and porous with a smooth exterior surface. The observation that morphology is not limited to a narrow range shows promise of carbonaceous spherules being discovered for a range of conditions rather than conditions specific only to those that formed the Whitecourt crater.

Spherules are not likely the result of a wildfire because the burning and combustion from the fire would cause biomass to preferentially be converted to charcoal or ash and would not form porous carbonaceous spherules. The slower heating rate of wildfires prevents structural change in the biomass so a liquid phase is not achieved. If the spherules were generated by wildfires then their presence should be commonly observed; however, reports of such occurrences could not be identified. The distribution and concentration of Whitecourt spherules also does not suggest a wildfire origin as they should have a more uniform concentration and be more widespread than what is observed. Furthermore, a wildfire cannot explain how silicate grains were incorporated into some of the Whitecourt spherules since the discovery of these grains were connected to spherules with intact crusts so they were not simply incorporated via a fracture. Given these selection parameters the best explanation to support this occurrence is that the grains were incorporated into the spherule while it was molten. This is supported by micro-CT data (Fig. 3-12) that show these higher density grains inside some spherules without any breaks in its outer crust.

3.5. Conclusions

The small size of the WMIC and low shock pressures may not have been conducive to extensive shock effects and target melt production but may have generated a previously unknown component: millimeter- to sub-millimeter-sized amorphous carbonaceous spherules. The most probable origin of these spherules is fast pyrolysis where during a rapid rate of temperature increase, such as an impact, biomass has the potential to be converted briefly to a molten phase. Terrestrial processes exist which can generate similar sized spherules to the ones associated with the WMIC but based on composition, location, or structure can be ruled out as potential origins leaving the impact as the most likely source. Parameters of the Whitecourt impact including the small crater size, young age, and availability of biomass all contributed to the generation and preservation of amorphous carbonaceous spherules at this site. Future low-energy impact discoveries may uncover comparable spherules following this initial detection of these objects.

Bibliography

American Coal Ash Association. 2003. *Fly ash facts for highway engineers*. Federal Highway Administration Technical Report #FHWA-IF-03-019. 74 p.

Artemieva N. and Pierazzo E. 2011. The Canyon Diablo impact event: 2. Projectile fate and target melting upon impact. *Meteoritics & Planetary Science* 46:805-829.

Bland P. A. and Artemieva N. A. 2006. The rate of small impacts on Earth. *Meteoritics & Planetary Science* 41:607-631.

Boslough M. B. E. and Crawford D. A. 2008. Low-altitude airbursts and the impact threat. *International Journal of Impact Engineering* 35:1441-1448.

Cassidy W. A., Glass B., and Heezen B. C. 1969. Physical and chemical properties of Australasian microtektites. *Journal of Geophysical Research* 74:1008-1025.

Cetin E., Moghtaderi B., Gupta R., and Wall T. F. 2004. Influence of pyrolysis conditions on the structure and gasification reactivity of biomass chars. *Fuel* 83:2139-2150.

Cetin E., Gupta R., and Moghtaderi B. 2005. Effect of pyrolysis pressure and heating rate on radiata pine char structure and apparent gasification reactivity. *Fuel* 84:1328-1334.

Chernogor L. F. and Rozumenko V. T. 2013. The physical effects associated with Chelyabinsk meteorite's passage. *Problems of Atomic Science and Technology* 4:136-139.

Commandré J. M., Lahmidi H., Salvador S., and Dupassieux N. 2011. Pyrolysis of wood at high temperature: The influence of experimental parameters on gaseous products. *Fuel Processing Technology* 92:837-844.

Dall'Ora M., Jensen P. A., and Jensen A. D. 2008. Suspension combustion of wood: Influence of pyrolysis conditions on char yield, morphology, and reactivity. *Energy & Fuels* 22:2955-2962.

D'Orazio M., Folco L., Zeoli A., and Cordier C. 2011. Gebel Kamil: The iron meteorite that formed the Kamil crater (Egypt). *Meteoritics & Planetary Science* 46:1179-1196.

Firestone R. B., West A., Kennett J. P., Becker L., Bunch T. E., Revay Z. S., Schultz P. H., Belgya T., Kennett D. J., Erlandson J. M., Dickenson O. J., Goodyear A. C., Harris R. S., Howard G. A., Kloosterman J. B., Lechler P., Mayewski P. A., Montgomery J., Poreda R., Darrah T., Que Hee S. S., Smith A. R., Stich A., Topping W., Wittke J. H., and Wolbach W. S. 2007. Evidence for an extraterrestrial impact 12,900 years ago that contributed to the megafaunal extinctions and the Younger Dryas cooling. *Proceedings of the National Academy of Science* 104:16016-15021.

Firestone R. B. 2009. The case for the Younger Dryas extraterrestrial impact event: Mammoth, megafauna, and clovis extinction 12900 years ago. *Journal of Cosmology* 2:256-285.

Glass B. P. and Simonson B. M. 2012. Distal impact ejecta layers: Spherules and more. *Elements* 8:43-48.

Graham R. G., Bergougnou M. A., and Overend R. P. 1984. Fast pyrolysis of biomass. *Journal of Analytical and Applied Pyrolysis* 6:95-135.

Howard K. T. 2011. Volatile enhanced dispersal of high velocity impact melts and the origin of tektites. *Proceedings of the Geologists' Association* 122:363-382.

Israde-Alcántara I., Bischoff J. L., Dominguez-Vázquez G., Li H-C., DeCarli P. S., Bunch T. E., Wittke J. H., Weaver J. C., Firestone R. B., West A., Kennett J. P., Mercer C., Xie S., Richman E. K., Kinzie C. R., and Wolbach W. S. 2012. Evidence from central Mexico supporting the Younger Dryas extraterrestrial impact hypothesis. *Proceedings of the National Academy of Science* 109:E738-E747.

Jimenez-Cordero D., Heras F., Alonso-Morales N., Gilarranz M. A., and Rodriguez J. J. 2013. Porous structure and morphology of granular chars from flash and conventional pyrolysis of grape seeds. *Biomass and Bioenergy* 54:123-132.

Kaburagi Y., Hosoya K., Yoshida A., and Hishiyama Y. 2005. Thin graphite skin on glass-like carbon fiber prepared at high temperature from cellulose fiber. *Carbon* 43:2817-2833.

Kapp R. O. 1969. *How to know pollen and spores*, 1st ed. Dubuque: Wm. C. Brown Company Publishers. 249 p.

Kring D. A. 1997. Air blast produced by the Meteor Crater impact event and a reconstruction of the affected environment. *Meteoritics & Planetary Science* 32:517-530.

Kurosaki F., Koyanaka H., Tsujimoto M., and Imamura Y. 2008. Shape-controlled multi-porous carbon with hierarchical micro-meso-macro pores synthesized by flash heating of wood biomass. *Carbon* 46:850-857.

Luik H., Johannes I., Palu V., Luik L., and Kruusement K. 2007. Transformations of biomass internal oxygen at varied pyrolysis condition. *Journal of Analytical and Applied Pyrolysis* 79:121-127.

Massicotte H. B., Trappe J. M., Peterson R. L., and Melville L. H. 1992. Studies on *Cenococcum geophilium*. II. Sclerotium morphology, germination, and formation in pure culture and growth pouches. *Canadian Journal of Botany* 70:125-132.

Moore J. G. and Peck D. L. 1962. Accretionary lapilli in volcanic rocks of the Western Continental United States. *The Journal of Geology* 70:182-193.

Piskorz J., Radlein D., and Scott D. S. 1986. On the mechanism of the rapid pyrolysis of cellulose. *Journal of Analytical and Applied Pyrolysis* 9:121-137.

Pyne S. J. 1984. *Introduction to wildland fire*. New York: John Wiley & Sons, Inc. 455 p.

Rodriguez-Reinoso F. 2002. Production and applications of activated carbons. In *Handbook of porous solids, e*dited by Schüth F., Sing K. S. W., and Weitkamp J. Weinheim: Wiley VCH. pp. 1766-1827.

Schumacher R. and Schmincke H. 1991. Internal structure and occurrence of accretionary lapilli - a case study at Laacher See Volcano. *Bulletin of Volcanology* 53:612-634.

Scott A. C. 2010. Charcoal recognition, taphonomy and uses in paleoenvironmental analysis. *Palaeogography, Palaeoclimatology, Palaeoecology* 291:11-39.

Scott A. C., Pinter N., Collinson M. E., Hardiman M., Anderson R. S., Brain A. P. R., Smith S. Y., Marone F., and Stampanoni M. 2010. Fungus, not comet or catastrophe, accounts for carbonaceous spherules in the Younger Dryas "impact layer". *Geophysical Research Letters* 37:L14302, doi: 10.1029/2010GL043345.

Septien S., Valin S., Dupont C., Peyrot M., and Salvador S. 2012. Effect of particle size and temperature on woody biomass fast pyrolysis at high temperature. *Fuel* 97:202-210.

Watanabe M., Inoue Y., Sakagami N., Bolormaa O., Kawasaki K., Hiradate S., Fujitake N., and Ohta H. 2007. Characterization of major and trace elements in sclerotium grains. *European Journal of Soil Science* 58:786-793.

Watanabe T. 2010. *Pictorial atlas of soil and seed fungi*, 3rd ed. Boca Raton: CRC Press. 404 p.

CHAPTER 4: General discussion and conclusions

The results of this study further develop the understanding of low-energy impact processes from the examination of meteorite fragments and the soil surrounding the Whitecourt Meteorite Impact Crater (WMIC). If a similar impact were to occur today in or near a populated area the effects in the immediate area could be severe, especially if the impactor is composed predominantly of Fe-Ni metal. If the impactor fragments upon impact, as was the case for the WMIC, shrapnel can be ejected at least 900 m away even if the impactor was only 1 m in diameter.

Iron meteorites with a diameter of 2.5 m are predicted to reach Earth's surface once every 50 years and as meteorite diameters increase their frequency decreases (Bland and Artemieva, 2006). Earth's atmosphere plays a significant role in disrupting objects when Earth and their orbits intersect leading to low-altitude airbursts if the incoming meteor has a non-metal composition. Boslough and Crawford (2008) concluded low-altitude airbursts are the most common events to impact the ground and predicted that the next event to cause damage on Earth's surface would be such an airburst. February 2013 saw this event unfold over Russia with the Chelyabinsk meteorite with injuries and building damage resulting from 0.2 Megatons of energy released at an altitude of 25 km (Chernogor and Rozumenko, 2013). The impact event that created Barringer Crater has been considered a low-altitude airburst which also involved a low velocity crater forming impact (Boslough and Crawford, 2008).

Impact spherules are associated with some large terrestrial impacts and are usually composed of melted target or impactor material. The small size and young age of the WMIC are important factors associated with the carbonaceous spherules found in the soil surrounding the crater. The size range of the carbonaceous spherules falls within the range of confirmed impact spherules from other impact sites around the world (Table 1-1). This study is the first to find this type of spherule directly associated with an impact crater so there are additional areas that can be explored in the future. Further study of the spherules associated with the WMIC could reveal the extent of the expansion plume generated by the impact to better determine the area affected by the impact. One other aspect that could be explored regarding the spherules is to determine their age by ^{14}C dating. Determining the carbon date of the spherules could better constrain when the impact event occurred.

Bibliography

Bland P. A. and Artemieva N. A. 2006. The rate of small impacts on Earth. *Meteoritics & Planetary Science* 41:607-631.

Boslough M. B. E. and Crawford D. A. 2008. Low-altitude airbursts and the impact threat. *International Journal of Impact Engineering* 35:1441-1448.

Chernogor L. F. and Rozumenko V. T. 2013. The physical effects associated with Chelyabinsk meteorite's passage. *Problems of Atomic Science and Technology* 4:136-139.

APPENDIX:

Appendix 1 – Detailed methodology

A.1.1. Meteorite collection

Sample collection of Whitecourt meteorites has continued throughout the years since the discovery and confirmation of the Whitecourt Meteorite Impact Crater (WMIC) in 2007. Meteorites available for analysis include several hundred recovered out of nearly 4000 documented finds outside the protected area in addition to over 500 recovered fragments collected within the protected area with required permission from Alberta Historic Resources. The meteorites recovered outside the protected area were primarily recovered by diligent volunteers and residents of the local region, so the information provided for these finds is invaluable as most samples found belong to private collections.

Whitecourt meteorites are buried beneath the surface and therefore are located using handheld metal detectors calibrated for recognizing iron targets; some detectors used include Minelab 3000, Garrett ACE250, Garrett GTI 2500, Garrett Pro-Pointer, Fisher F75, and Goldbug II. Once a target was localized the meteorite was excavated and the removed soil was searched by hand with the aid of a small accurate pin pointing metal detector, but more commonly a rare earth magnet was used. Most of the information regarding a meteorite find is documented immediately including, most importantly, the GPS coordinates from a handheld device and if possible the depth the meteorite was recovered from, type of soil it was in, and any other interesting features or notes regarding its collection. Details regarding searching techniques have not been widely disclosed, but from what has been shared techniques range from random searching to systematic grid searching. Areas with minimal ground cover have been searched most thoroughly due to the ease of access; some areas are currently inaccessible due to fallen trees or dense bushes. Searching is suspended during the winter months as the frozen ground and snow accumulation prevent the detection and collection of samples.

A.1.2. Meteorite processing and preparation

Meteorite samples from the WMIC were processed in the lab by giving their surface a gentle scrub with a soft brush to remove excess dirt and debris using deionized water followed by an acetone wash to eliminate residual water. Once dry, the weight of the meteorite was measured followed by an examination and documentation of the exterior surface using a stereo microscope. Features such as fragment morphology, the relative amount of terrestrial weathering, and any other surface characteristics were noted. Morphologic features include if the fragments are thin, thick, flat, twisted, blocky, angular, or rounded. The amount of terrestrial weathering is a relative estimate based primarily on the thickness of the buildup of secondary minerals on the surface and the ability to recognize details on the surface of the meteorite; terrestrial buildup levels were designated as low, moderate, high, and very high. Additional features noted include whether octahedral crystal planes were observed as part of the fragment's shape, if any edges or faces showed potential areas of deformations, or any other interesting characteristics that were observed.

After processing, meteorites were selected for further analysis based on their different morphological features. Further analysis involved examining the interior of the meteorites and therefore they were required to be cut apart. Due to limitations of size and weight that could be handled by our Buehler's Isomet low speed saw, small meteorites less than about 50 g were chosen for a given morphological feature. Sample weight lost was minimal, ranging from 1.6 to 5.2 % with an average loss of 2.8% (Table A-1). For two meteorites when the blade dressing stick was not used the cuttings were collected. The cuttings were collected in the saw's holding tray in DI water and were removed with a magnet and set aside to dry. When the weight of the cuttings was added to the weight of the meteorite pieces, the total sample loss dropped to <0.4%.

Table A-1: Meteorite weight lost during cutting

Sample	Starting weight (g)	Weight after cut (g)				Weight lost (g)	Weight lost (%)	Cutting weight collected (g)	Net weight lost with cuttings (%)	Dressing used
		piece a	piece b	piece c	total					
SZ44.14	13.6131	7.3872	5.8603	0	13.2475	0.3656	2.69	0	0	yes
BZ7	5.2745	3.4769	1.6137	0	5.0906	0.1839	3.49	0	0	yes
BZ7	3.4563	2.9366	0	0.4153	3.3519	0.1044	3.02	0	0	no
Ch008	26.64	16.2033	9.9224	0	26.1257	0.5143	1.93	0.4407	0.28	no
Ch008	9.9050	0	8.3700	1.3249	9.6949	0.2101	2.12	0	0	yes
LJJZ27	49.0898	28.5147	19.7638	0	48.2785	0.8113	1.65	0.6538	0.32	yes
LJJZ27	19.6268	0	18.0864	1.1567	19.2431	0.3837	1.95	0	0	no
JZ24	7.8218	3.7752	3.7458	0	7.5210	0.3008	3.85	0	0	no
JZ24	3.7752	3.2782	0	0.3779	3.6561	0.1191	3.15	0	0	no
SZ32	6.2090	3.6134	2.4218	0	6.0352	0.1738	2.80	0	0	no
SZ32	2.4218	0	2.1640	0.1933	2.3573	0.0645	2.66	0	0	no
J12	4.7797	4.2155	0	0.4863	4.7018	0.0779	1.63	0	0	no
J12	4.2155	2.9608	1.0366	0	3.9974	0.2181	5.17	0	0	no
J374	17.7097	9.4223	7.7296	0	17.1519	0.5578	3.15	0	0	yes
J374	7.7296	0	7.3471	0.1812	7.5283	0.2013	2.60	0.1752	0.34	no

After being cut the some meteorites were mounted in epoxy then all pieces, mounted or not, were polished. Small meteorites were mounted in epoxy using 2.5 cm aluminum rings. Once the epoxy hardened sandpaper lubricated with water was used to grind the samples to expose the meteorite; sandpaper grit started at 250 followed by 400 and 600. Sandpaper was also used to grind the surfaces of the meteorite pieces not mounted in epoxy following the same steps. Next all meteorites were polished using polishing pads and alumina fluids starting with 5 µm alumina followed by 1 µm and 0.05 µm; alumina fluid consists of alumina particles suspended in water. When polishing is complete the samples are placed in a sonic vibrator to remove residual alumina then dried. Samples are now ready to be carbon coated if necessary.

Some polished samples may be chemically etched to reveal the internal Widmanstätten pattern. The etching process used the etchant nitol and within several minutes the internal texture of the meteorites was visible; nitol is a solution of 10% HNO_3 and 90% ethanol (e.g., Norton, 2002; Szurgot et al., 2008).

A.1.3. Soil and spherule collection

Near the end of processing meteorite shrapnel fragments the first spherules were identified on the exterior weathered surface of some of these meteorites; all meteorites recovered following this discovery were then examined for the presence of spherules on their surfaces prior to the gentle scrub and acetone wash. Spherules found on meteorite surfaces were either embedded in the exterior weathered crust/rind of the meteorites or trapped within sediments filling in grooves or curled edges of the meteorites. Spherules trapped within these sediments were easily removed and embedded ones required additional care to remove, which involved scraping off the weathered rind to expose enough of the spherule that it could be removed intact.

Since these spherules were found adhered to the weathered surface of meteorites it was presumed that the spherules would also be present in the soil. Since most shrapnel meteorite fragments have been found to a depth of 25-30 cm, this also became the target depth for soil collection. Locations of soil collection were first obtained from outside the protected area while still remaining within the shrapnel distribution field. Once a hole was dug a small vertical section of the exposed profile was removed and placed in a bag, while attempting to keep the profile in one piece in order to determine if there are changes in spherule concentration with depth or other features of the soil profile. At soil location 5, 6, and 7 (Fig A-1) the collected soil profiles contained a meteorite in situ in order to determine if there is a relationship with meteorite occurrence (Table 3-1).

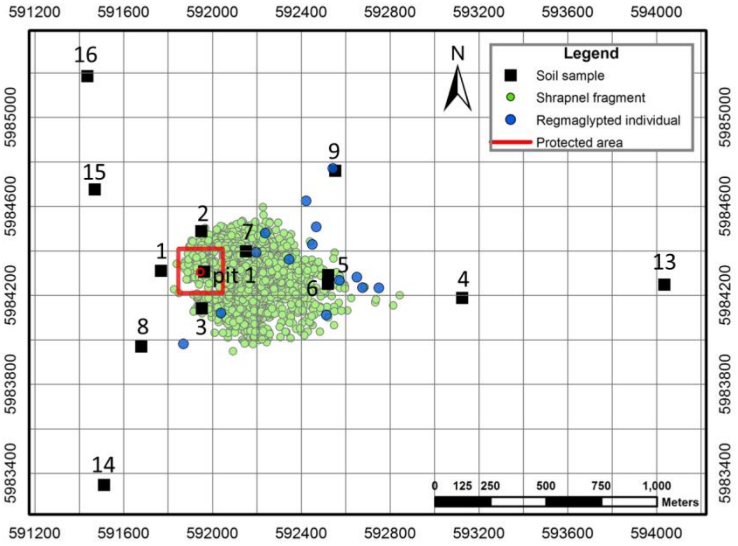

Figure A-1: Locations of collected soil samples with their numeric labels. Numbers correspond to the locations listed in Table 3-1. Grid spacing is 200 m.

A.1.4. Soil processing and spherule preparation

After soil collection the samples were allowed to dry since excess moisture in the soil prevented easy separation of soil components and grains; which was necessary to recognize and separate any spherules from the soil. Soil samples containing spherules were processed in the lab in stages. Soils were examined in depth increments of 5 cm, allowing any change associated with depth to be observed. Smaller subsamples for each increment were examined slowly and carefully for carbonaceous spherules. Even though the spherules are small in diameter their dark colour stands out against the various light coloured sands, clays, organics, and other grains present in the soil. Once identified spherules were carefully removed using tweezers, gently cleaned with Kimwipes, and collected in a vial. Spherule totals were kept to assist with determining their distribution and concentration (Table A-2). The spherule concentration for soil sample location 5 (Table 3-1) was not included because it was the first location to be analyzed and its collection method was not consistent with all subsequent locations, so the results are not directly comparable. Excluding location 5 does not represent a loss in data since location 6 is only 40 m away so there is still data representing the area (Fig. A-1).

Spherules selected for specific analyses were further cleaned with a quick acetone wash to further remove soil particles. Selected spherules included ones that appeared to have no cracks or breaks in the outer crust, ones with varying diameters, and different shapes or morphologies. Some of the spherules with complex shapes were not cleaned so some soil grains remained on their surface, which was done to ensure these rare spherules remained undamaged. Spherules were then mounted on soft colourless wax in preparation for micro-CT scanning. Once scans were acquired and the images were examined some of the spherules were then mounted in epoxy in the same manner as meteorites, with extra care given in all stages due to the spherules' more delicate structure.

Table A-2: Carbonaceous spherule distribution in collected soil samples

Soil sample	# spherules per depth interval					Total spherules	Weight of soil (g)	Spherule concentration (#/g)
	0-5 cm	5-10 cm	10-15 cm	15-20 cm	20-25 cm			
1	3	15	14	9	13	54	50.73	1.1
2	50	32	20	23	11	136	43.68	3.1
3	44	51	37	30	10	172	43.34	4.0
4	31	34	33	11	4	113	55.75	2.0
6	2	33	17	13	3	68	33.02	2.1
7	108	166	55	32	14	375	71.58	5.2
8	14	77	15	16	5	127	32.36	3.9
9	64	19	5	0	0	88	29.72	3.0
13	15	10	2	3	0	30	32.64	0.9
14	4	0	3	0	0	7	25.89	0.3
15	8	6	2	0	0	16	25.74	0.6
16	1	0	0	0	0	1	31.19	0.0
pit 1	75	16	2	2	2	97	28.99	3.3

Based on observations in the micro-CT data some spherules contained small grains and to find more of these grains about 25 were gently broken apart. Before breaking the spherules their exterior surface was cleaned to remove obvious soil particles and examined for any cracks. It was important that the spherule's crust was intact with no cracks present in order to rule out the possibility that any grains found did not enter the spherule via these openings. This method produced nine grains which were colourless or slightly orange in colour. These grains were placed on a stand covered with carbon tape then carbon coated for SEM analysis.

Appendix 2 – Micro-CT scanning methods and details

A.2.1. Carbonaceous spherule scans

Eighteen carbonaceous spherules were selected to be scanned based on their size and morphology. Once selected the spherules were mounted on soft colourless wax. A small wax stand was created in order to have as little of the spherule in contact with the wax as possible. Less contact ensures the wax's interference with the X-rays during the scan is kept to a minimum.

The density of the wax is low enough that contact with a spherule does not impede the X-rays from penetrating into the spherule during the scan. Denser mounting mediums such as clay or putty cause some scan interference. A scan of a spherule mounted in epoxy was tried but the 2.5 cm diameter caused significant interference making the scan unusable.

A SkyScan 1172 desktop microtomograph acquired X-ray scans of the carbonaceous spherules. Due to the small diameters of the spherules high resolution scans could be conducted while keeping files at a manageable size; file size limits the amount of post-scan processing. Scans were set with a source voltage between 40-50 kV, pixel size between 0.9 and 1.6 µm and no filter was applied (Table A-3). Using these settings scan duration was approximately one hour. Scans are composed of a series of transmission images produced when the X-ray beam passes through the spherule (Fig. A-2). The illumination intensity (brightness) in the transmission image corresponds to the absorption of the X-ray beam as it passed through the spherule; zero intensity indicates no absorption and is essentially empty space within the object and high intensity (darker colour) indicates higher density and therefore more X-ray absorption. Images are acquired as a series of fixed rotation steps through 180 or 360 degrees making each sequential image rotated by the rotation step amount. The X-ray exposure time for each rotation step is 2356 ms and the final output image is saved as a TIFF file. Frame averaging and random movement were turned and values set to 2 and 5 respectively for all scans.

Table A-3: Micro-CT acquisition parameters for carbonaceous spherules[1]

Spherule ID	Number of files	Source voltage (kV)	Source current (µA)	Image pixel size (µm)	Filter	Rotation step (deg)	Use 360 rotation	Scan duration
cs1	576	44	226	0.94	No filter	0.34	NO	1:31:15
cs2	490	51	192	1.45	No filter	0.4	NO	1:17:53
cs3	385	50	198	1.45	No filter	0.51	NO	1:01:18
cs4	401	50	198	1.45	No filter	0.49	NO	1:03:53
cs5b	409	50	198	1.45	No filter	0.48	NO	1:05:04
cs6	436	49	200	1.45	No filter	0.45	NO	1:09:23
cs7b	436	40	250	1.62	No filter	0.45	NO	1:09:30
cs8b	351	40	250	1.62	No filter	0.56	NO	0:56:13
cs9b	385	40	250	1.62	No filter	0.51	NO	1:01:42
cs10	467	40	250	1.62	No filter	0.42	NO	1:14:09
cs11e	644	40	250	1.62	No filter	0.56	YES	1:42:33
cs12	393	40	250	1.62	No filter	0.5	NO	1:02:33
cs13	393	40	250	1.62	No filter	0.5	NO	1:02:33
cs14	393	40	250	1.62	No filter	0.5	NO	1:02:33
cs15	371	40	250	1.62	No filter	0.53	NO	0:59:06
cs16b	328	40	250	1.62	No filter	0.6	NO	0:52:21
cs17	385	40	250	1.62	No filter	0.51	NO	1:01:33
cs18	409	40	250	1.62	No filter	0.48	NO	1:05:04

[1] parameters used for the SkyScan 1172 Desktop X-ray microtomograph

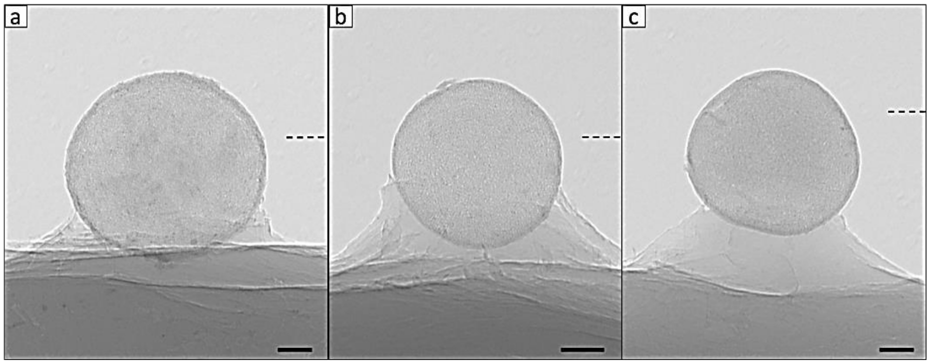

Figure A-2: X-ray transmission images of carbonaceous spherules obtained from a SkyScan 1172 micro-CT scanner; spherules are mounted in wax. (a) Spherule with a thick crust and small areas of higher density which are slightly darker in colour. (b) Thin crusted spherule with a constant and even interior structure. (c) Spherule is quite similar to part b) with the exception of a chip to its exterior; void is located at upper left edge of spherule. Dashed lines indicate the location of the transaxial images in Figure A-3. [scale bars = 200 µm]

A.2.2. Carbonaceous spherule image reconstruction

Once all images are acquired the TIFF output files are reconstructed into transaxial images using SkyScan's reconstruction program NRecon (Fig. A-3). Several processing options are available to correct and enhance the scans such as smoothing, ring artifacts, and beam hardening (Table A-4). These settings can be adjusted and previewed before the reconstruction process is started. When reconstruction is complete the images become a two-dimensional representation of the internal microstructure and density of the scanned spherule.

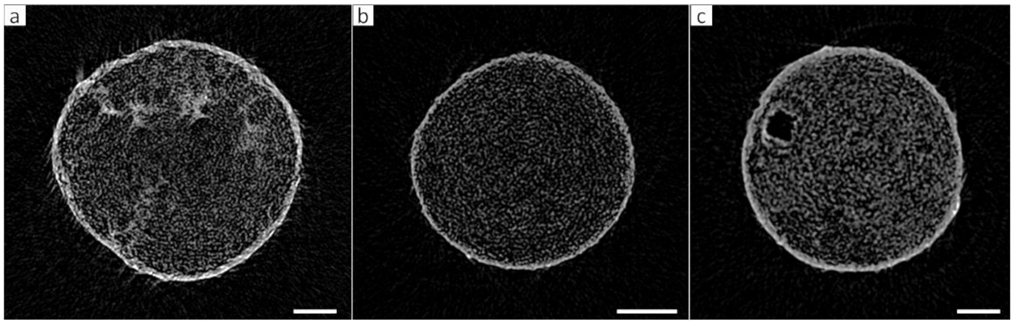

Figure A-3: Reconstructed transaxial images of the spherules shown in Figure A1 with corresponding order. (a) Denser areas of spherule are brighter in colour. (b) Interior of spherule is very uniform. (c) Part of the chip in the crust of this spherule is visible as a large void near the left edge; rest of the spherule's interior is uniform. [scale bars = 200 µm]

Table A-4: Micro-CT reconstruction parameters for carbonaceous spherules[1]

Spherule ID	Postalignment	Sections count	Pixel size (µm)	Smoothing	Ring artifact correction	Beam hardening correction (%)
cs1	0	1154	0.93723	2	8	14
cs2	7	885	1.44895	4	8	14
cs3	4.5	605	1.44895	4	8	14
cs4	5.5	641	1.44895	4	8	14
cs5b	1	527	1.44895	4	8	14
cs6	8.5	741	1.44895	4	8	14
cs7b	9	721	1.61886	4	14	14
cs8b	8	361	1.61886	4	14	14
cs9b	3.5	511	1.61886	4	14	14
cs10	3.5	581	1.61886	4	14	14
cs11e	5	231	1.61886	4	14	14
cs12	6	691	1.61886	4	14	14
cs13	11	451	1.61886	4	14	14
cs14	9.5	631	1.61886	4	14	14
cs15	6	481	1.61886	4	14	14
cs16b	3.5	243	1.61886	4	8	14
cs17	7	411	1.61886	4	14	14
cs18	7.5	871	1.61886	4	8	14

[1] parameters used in the SkyScan reconstruction program NRecon

A.2.3. Carbonaceous spherule image analysis

Three SkyScan programs were available to analyze different attributes of the reconstructed spherule images; DataViewer, CT-Analyser, and CT-Volume. DataViewer is used to examine the images in two or three-dimensions. Two dimensional viewing is limited to transaxial sections while the limited three-dimensional viewing includes coronal and sagittal sections. Any point within the spherule can be selected and the corresponding three views can be simultaneously examined (Fig. A-4). Changes to the images themselves cannot be accomplished with DataViewer, for that CT-Analyser is used. CT-Analyser (CTAn) is a tool that can identify areas with different densities based on attenuation coefficients, select areas of interest, generate binary images, apply different colours, or create three-dimensional models of an entire spherule or just specific areas. Models can then be opened to view and manipulate in three-dimensions using CT-Volume (Fig. A-4).

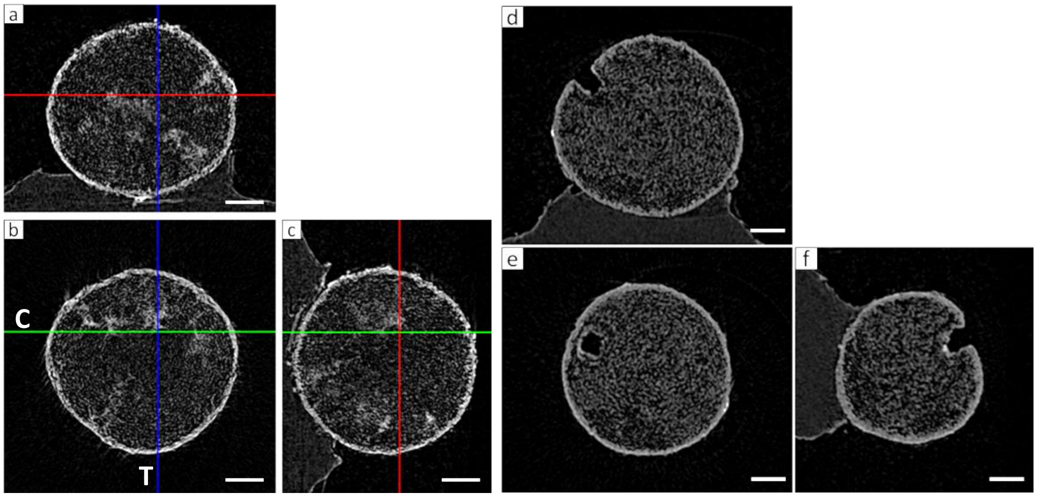

Figure A-4: Addition of coronal and sagittal views for the same transaxial images of spherules as shown in Figure A-3a) and A-3c); obtained using DataViewer. (a-c) This series of images includes a coronal view a) and sagittal view c) which show some of the isolated areas of higher density within this spherule. Coloured crosshairs in image b) correspond to the locations of the coronal view (horizontal green line C = image a) and sagittal view (vertical blue line T = image c). Red line corresponds to the location of transaxial image b). (d-f) This series includes a coronal d), transaxial e), and sagittal view f) which focus on the broken edge of the spherule. Crosshairs are absent so structures are not obscured. [scale bars = 200 µm]

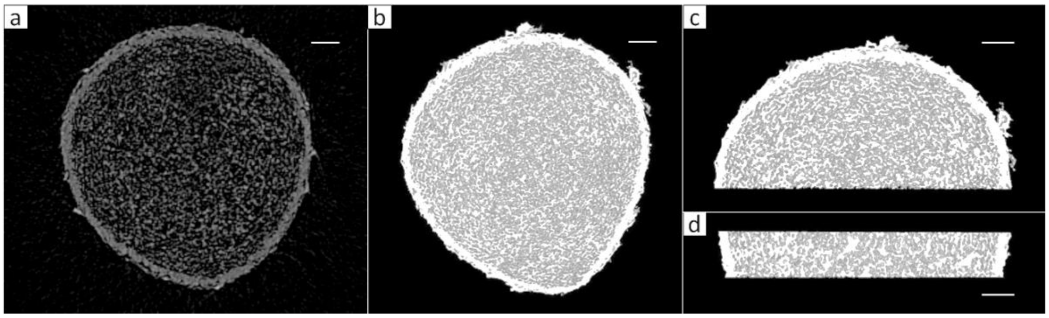

Figure A-5: Spherule models generated from micro-CT data. (a) Transaxial image of a spherule with a thick crust and uniform interior. (b) 3D model of a 146 µm thick section of the spherule generated using reconstructed micro-CT data showing the same cross-section as a). (c) Same model as b) but with a plane cut through the center. (d) Side view created by the plane that cut across the 3D model in c) showing vertical changes within the spherule. [scale bars = 100 µm]

Appendix 3 – Inconclusive analysis: meteorite micro-CT

A SkyScan 1172 microtomograph was used to obtain scans of Whitecourt iron meteorites in an attempt to determine the distribution of accessory minerals. It was quickly discovered that the meteorites were too dense to be able to distinguish between the metal and non-metal phases with any clarity. The dominant metallic phases of kamacite and taenite are even more similar in density so they are undistinguishable from each other in the scans. Next the thinnest meteorites available were scanned to determine if a decrease in thickness would yield better results. The quality of scans showed some improvement and less scattering of X-rays but the high density of the sample still affected scanning precision. Acquisition and reconstruction parameters for the more successful small thin meteorites, as well as the scans that did not yield good results, are given in Table A-5 and Table A-6. Even though this non-destructive technique did not achieve the desired outcome it was able to show the amount of terrestrial weathering present in a sample; this was most evident for two thin and highly weathered shrapnel fragments. The lower density and extensive area the alteration products cover contrasts with the denser metal phase for one of these fragments in Figure A-6. The alteration products cover the external surface and fill preferentially weathered cracks that extend into the interior of the

Table A-5: Micro-CT acquisition parameters for meteorites[1]

Meteorite ID	Number of files	Source voltage (kV)	Source current (µA)	Image pixel size (µm)	Filter	Rotation step (deg)	Use 360 rotation	Scan duration	Exposure (ms)
SZ40a	514	49	200	34.07	Al 0.5 mm	0.7	YES	0:26:25	632
SZ40b	900	100	100	16.87	Al+Cu	0.4	YES	2:22:40	2360
SZ40c	512	100	100	11.93	Al+Cu	0.4	NO	0:46:08	1770
LJJZ62	1200	89	110	8.52	Al+Cu	0.3	YES	9:38:12	9424
BZ34	490	100	100	15.84	Al+Cu	0.4	NO	1:49:40	4425
J251b	512	100	100	11.93	Al+Cu	0.4	NO	0:30:48	1180
SZ44.24c	512	100	100	11.93	Al+Cu	0.4	NO	0:45:58	1770
SZ44.37b	436	100	100	11.93	Al+Cu	0.47	NO	0:26:19	1180
J327b	456	100	100	11.93	Al+Cu	0.45	NO	0:27:31	1180
J353b	395	100	100	11.93	Al+Cu	0.52	NO	0:23:56	1180

[1] parameters used for the SkyScan 1172 Desktop X-ray microtomograph

Table A-6: Micro-CT reconstruction parameters for meteorites[1]

Meteorite ID	Postalignment	Sections count	Pixel size (µm)	Smoothing	Ring artifact correction	Beam hardening correction (%)
SZ40a	0.5	326	34.09362	10	20	49
SZ40b	-2.5	978	16.87707	1	1	0
SZ40c	-2	1526	11.93047	3	17	86
LJJZ62	-9	1957	8.52065	10	20	49
BZ34	-2.5	1006	15.84535	5	9	51
J251b	-3.5	939	11.93047	4	8	0
SZ44.24	-3	1792	11.93047	4	6	26
SZ44.37	-1	941	11.93047	2	8	20
J327	-2	1551	11.93047	3	4	20
J353	-2	2018	11.93047	4	8	20

[1] parameters used in the SkyScan reconstruction program NRecon

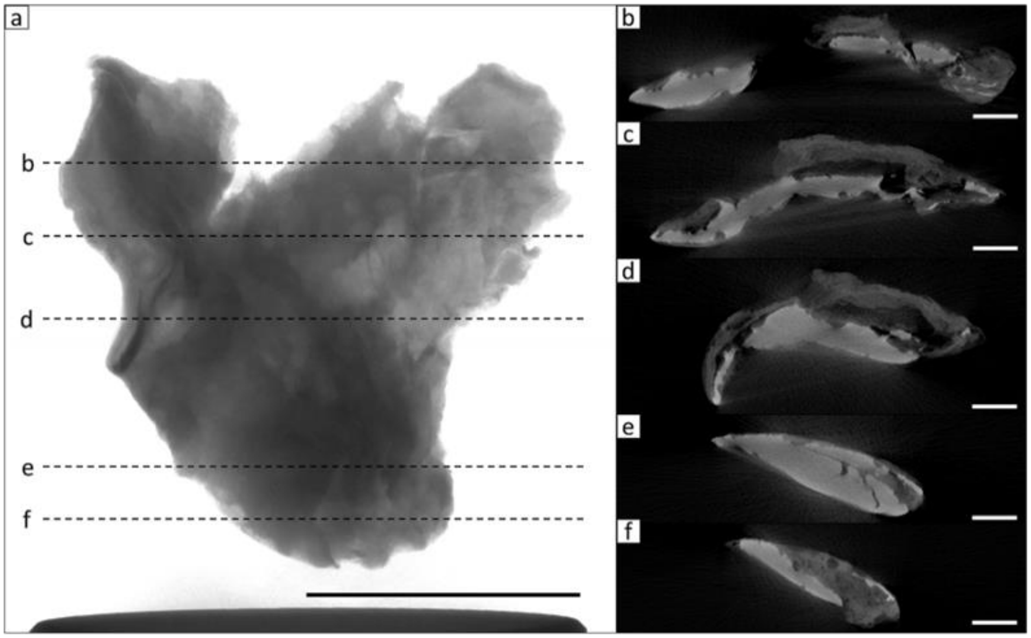

Figure A-6: Micro-CT scan of a small thin iron meteorite; mounted in wax. (a) X-ray transmission image of scanned meteorite. Dashed lines correspond to transaxial image (b-f) locations. [scale bar = 1 cm] (b-f) Reconstructed slices through this meteorite show a highly weathered sample where terrestrial weathering shows as darker colours and the iron portions of the meteorite are the brighter areas. [scale bars = 25 mm]

meteorite. This meteorite also shows small regions of interest in the interior that may be non-metal phases but without exposing the interior their composition remains unknown. The regions of interest are more likely the result of weathering as their density appears to be consistent with the density of weathering products along the meteorite's external surface and their proximity to the exterior or to cracks and are consistent with the weathered edges along cut and polished surfaces of other meteorites that were imaged by SEM (Fig. A-7). Even though the thin meteorites were too dense to be able to show compositional changes within the metal, the series of images in Figure A-8 shows that the extent of terrestrial weathering for this sample can be captured by using different techniques. The hand sample (Fig. A-8a) displays weathering through variation in colour and by the apparent thickness of the alteration product buildup. In the X-ray transmission image (Fig. A-8b) the darker areas correspond to where the denser metal exists and the X-rays are more strongly absorbed. For comparison the wax that mounts the meteorite to the sample holder (black zone at bottom of image) is not visible in the image resulting in the meteorite appearing to be suspended in air above the holder. The reconstructed images (Fig. A-6b-f) were used to generate a three-dimensional model since there was minimal X-ray scattering as edges are well defined. The density change between the meteoritic metal and weathered areas allows for manipulation of colour and transparency of the various densities to highlight details within the sample; brighter (more opaque) areas represent denser metal and darker more transparent areas are more highly weathered (Fig. A-8c).

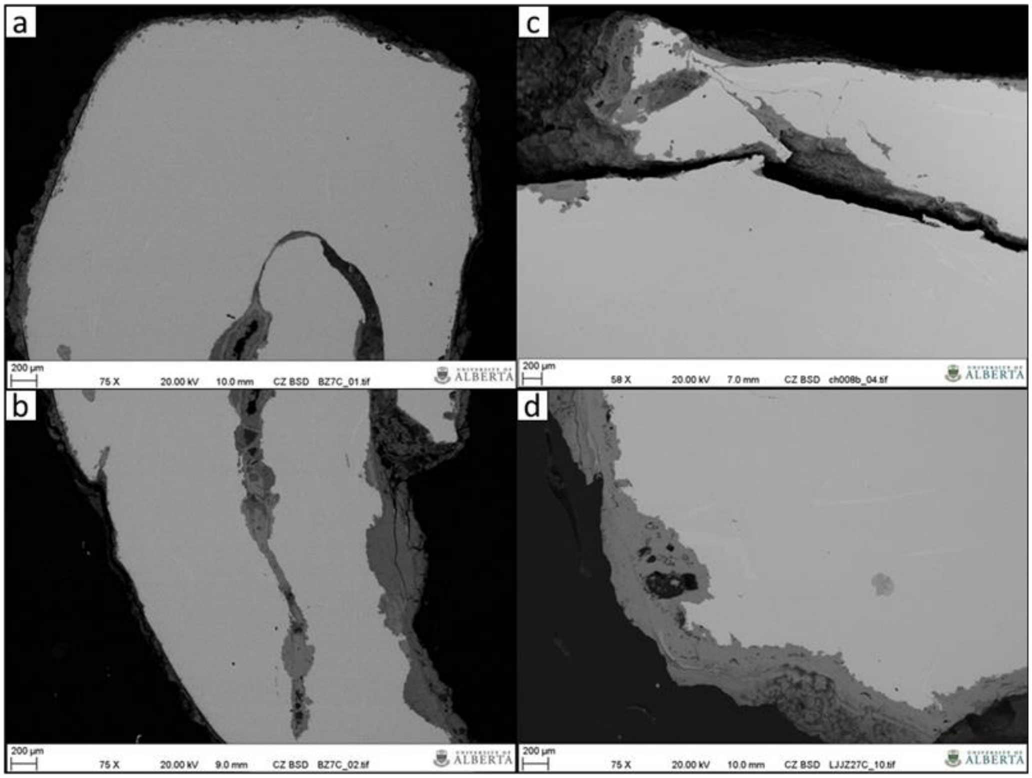

Figure A-7: SEM images of weathering along edges of meteorites. (a-b) These two images from the same meteorite show weathering along the external edge of the sample. Weathering also penetrates into the interior of the meteorite via a crack. (c) A wide crack near the edge of a meteorite shows weathering similar to the external surface of the sample. (d) This sample displays a high degree of terrestrial weathering along its external surface.

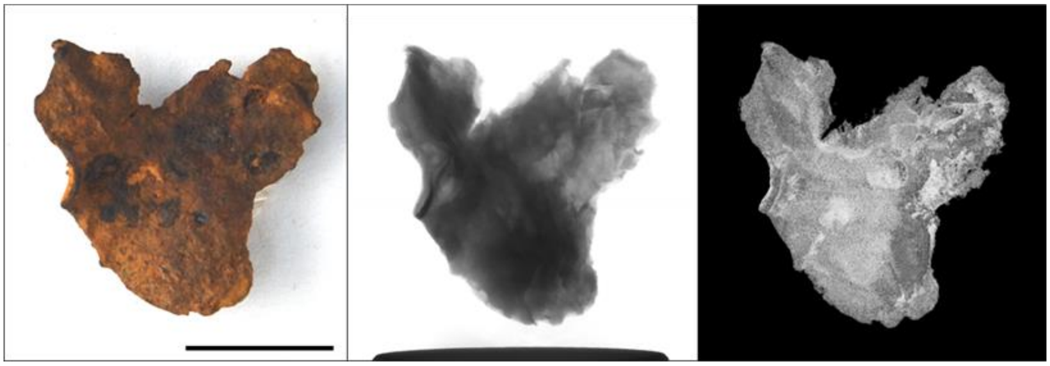

Figure A-8: Sequence of images for the same meteorite viewed in the same orientation. (a) Photograph showing the external morphology of a shrapnel fragment with a highly weathered surface. (b) Transmission image obtained during the acquisition phase of a micro-CT scan. (c) 3-D model generated from reconstructed images. [scale bar = 1 cm]

Appendix 4 – Additional information regarding samples examined in this study

A.4.1. Meteorites

The abundance of meteorites at the WMIC site has permitted a lot of information to be gathered such as meteorite dispersion resulting from the impact and the distribution of their mass. The quantity of meteorites recovered allows representative samples to be selected after examining a large proportion of them. Commonalities between samples become apparent and unique features stand out to be studied further. Meteorites selected to be cut (Table A-1) ranged in morphologies including rounded and angular shrapnel fragments, the presence of octahedral structures, or surface deformations. Not all meteorites that were cut were analyzed further due to the absence of accessory minerals, attributed to the small cross-sectional area of the meteorite; cutting process was restricted to small meteorites due to size limits of the saw. Table A-7 identifies the meteorites examined in this study by figure number. The external morphologies for some of these meteorites appear in Chapter 2 figures before they were cut to be examined and meteorites not previously shown are in Figure A-9 to provide context for their external morphology.

Figure A-9: External morphologies of shrapnel samples cut and had their interiors imaged by SEM for this study, shown in various figures in Chapter 2 and Appendix. (a) Rounded edges. (b-c) Two different views of the same thin angular fragment with curled edges. (d) Angular fragment with straighter edges. (e-f) Two views of the same fragment with a convex shape, relatively smooth surface, and angular edges. [scale bars = 1 cm]

Table A-7: Identification table of meteorites examined in this study

Figure #	Meteorite ID	Mass (g)	Ownership
2-4a	BZ10	67	UAlberta
2-4b	SZ44.14	13.6	Ualberta
2-4c	JZ24	7.8	UAlberta
2-4d	BZ75	21.2	UAlberta
2-4e	GZ48	<0.0-4.0	UAlberta
2-4f	J388	4.8	J. Newman
2-5a	CHZ4	24.9	UAlberta
2-5b	JZ63	57.7	UAlberta
2-5c	J334	67.5	J. Newman
2-5d	B459	31.4	B. Newman
2-5e	LJJZ76	189.7	UAlberta
2-5f	BZ69	30.3	UAlberta
2-6a	RS5	1177.6	UAlberta
2-6b	B147	6510.0	B. Newman
2-7a	J166	40.2	J. Newman
2-7b	B3	31.7	B. Newman
2-8a	JZ24c	0.4	UAlberta
2-8b	Ch008b	8.4	UAlberta
2-8c	Ch008c	1.3	UAlberta
2-8d	JZ24c	0.4	UAlberta
2-9a-d	Whitecourt 13	48.6	UAlberta
2-10a-b	B147 slice a	97.3	B. Newman
2-11a-e	B147uab slice	66.7	UAlberta
2-11f	LJJZ27c	1.2	UAlberta
2-12a-b	B147uab slice	66.7	UAlberta
2-13a	B147uab slice	66.7	UAlberta
2-13b-e	LJJZ27b	18.1	UAlberta
2-13f	B147uab slice	66.7	UAlberta
2-13g-h	LJJZ27b	18.1	UAlberta
2-14a	LJJZ27b	18.1	UAlberta
2-14b-d	B147uab slice	66.7	UAlberta
2-15a	B147uab slice	66.7	UAlberta
2-15b-c	JZ24a	3.8	UAlberta
2-15d	SZ32b	2.2	UAlberta
2-15e	JZ24a	3.8	UAlberta
2-15f	BZ7c	0.4	UAlberta
2-16a-b	LJJZ27b	18.1	UAlberta
2-16c	LJJZ27c	1.2	UAlberta
2-16d	B147uab slice	66.7	UAlberta
2-17a-b	B35	9.3	B. Newman
2-18a-b	J634	380.8	J. Newman
2-17a	BZ7b	1.6	UAlberta
2-17b	LJJZ27c	1.2	UAlberta
2-17c-d	B35	9.3	B. Newman
3-1a-b	B164	7.1	B. Newman
A-6a-f	SZ44.24	1.9	UAlberta
A-7a-b	BZ7c	0.4	UAlberta
A-7c	Ch008b	8.4	UAlberta
A-7d	LJJZ27c	1.2	UAlberta
A-8a-c	SZ44.24	1.9	UAlberta
A-9a	LJJZ27	49.1	UAlberta
A-9b-c	BZ7	5.3	UAlberta
A-9d	SZ32	6.2	UAlberta
A-9e-f	Ch008	26.6	Ualberta

A.4.2. Carbonaceous spherules

Some soil samples yielded more carbonaceous spherules than others but the overall morphology for the spherules was relatively consistent between locations. Initial analysis regarding the spherules' composition was done by semi-quantitative SEM (Table A-8). Further analysis with the EPMA provided more accurate compositions, and more data points, so that data was used. Comparing Table A-8 with Table 3-3 shows the differences in accuracy between the two methods utilized in obtaining compositions of the spherules. The small size and delicate nature of the carbonaceous spherules limits what can be done with them; however these spherule characteristics made them ideal for micro-CT analysis. The high resolution capability of the SkyScan 1172 coupled with the low density of the spherules yielded details at the micron scale which would have otherwise been difficult to detect without some destruction of the

Table A-8: Carbonaceous spherule compositions determined by scanning electron microscopy (SEM)

sample	n	C (wt%)	O (wt%)	Ca (wt%)	Fe (wt%)	Al (wt%)	Mg (wt%)
CS1	2	62.54 ± 1.06[1]	35.05 ± 1.82	2.22 ± 0.96	n.d.[2]	0.39 ± 0.00	n.d.
CS8	4	56.82 ± 2.13	34.74 ± 3.80	4.93 ± 1.69	1.51 ± 0.59	1.18 ± 0.60	0.29 ± 0.12
J527s1	1	56.02	29.70	0.16	13.09	0.53	n.d.
frothy-looking fragment	2	67.62 ± 1.76	27.85 ± 1.15	2.50 ± 0.14	n.d.	1.01 ± 0.26	0.15 ± 0.00

sample	n	Na (wt%)	Si (wt%)	K (wt%)	P (wt%)	Cl (wt%)	S (wt%)
CS1	2	n.d.	n.d.	n.d.	n.d.	n.d.	n.d.
CS8	4	0.11 ± 0.08	n.d.	0.15 ± 0.09	0.21 ± 0.11	n.d.	0.09 ± 0.04
J527s1	1	n.d.	0.34	n.d.	n.d.	0.18	n.d.
frothy-looking fragment	2	0.07 ± 0.00	1.18 ± 0.00	0.24 ± 0.00	n.d.	0.40 ± 0.00	n.d.

[1] Average of n analyses (norm wt%) with standard deviation provided

[2] n.d. = not determined

samples. Details such as enlarged pores, thickened crust, or terrestrial inclusions show clearly in scan data which are not detectable by simple examination of the external surface of the spherule. Figure A-10 provides images of external morphologies of examined spherules not previously been shown and Table A-9 identifies the carbonaceous spherules that were examined in this study by figure number.

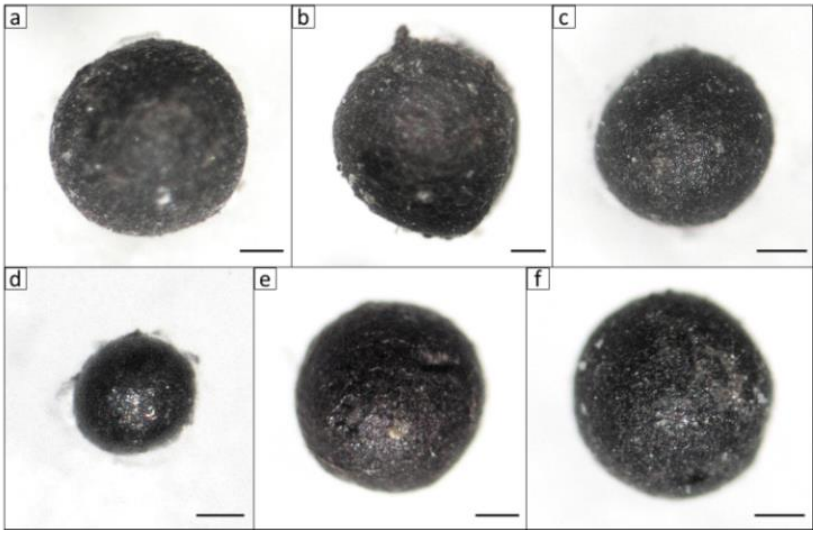

Figure A-10: External morphologies of carbonaceous spherules imaged by micro-CT for this study, shown in various figures in Chapter 3 and Appendix. (a) Sphere-like spherule. (b) Large spherule with a slight teardrop-like shape. (c) Average sized spherule with sphere-like shape. (d) Very small spherule with a smoother, darker, and more vitreous surface than most other spherules. (e) Sphere-like shape with a chip out of the outer crust in the upper right of spherule. (f) Also has a chip in crust located in the dark area at the bottom of spherule. [scale bars = 200 µm except for d) where scale bar = 100 µm]

Table A-9: Identification table of carbonaceous spherules examined in this study

Figure #	Spherule ID	Soil location
3-3a	various-not specified	
3-3b	cs18	8
3-3c-d	cs8	7
3-4a	various-not specified	
3-4b	cs4	1
3-4c	cs5	7
3-4d	cs17	7
3-4e	cs15	1
3-5a-d	cs8	7
3-6a-d	cs6	6
3-7a-d	cs11	4
3-8a-d	cs12	3
3-9a-e	char2	n/a
3-10a-c	char1	7
3-12a-b	cs6	6
3-12c-f	cs8	7
3-12g	cs17	7
3-14a-b	J527 s1	n/a
A-2a	cs1	2
A-2b	cs3	4
A-2c	cs14	5
A-3a	cs1	2
A-3b	cs3	4
A-3c	cs14	5
A-4a-c	cs1	2
A-4d-f	cs14	5
A-5a-d	cs2	3
A-10a	cs1	2
A-10b	cs2	3
A-10c	cs3	4
A-10d	cs11	4
A-10e	cs12	3
A-10f	cs14	5

Bibliography

Norton O. R. 2002. The Cambridge encyclopedia of meteorites, 1st ed. Cambridge: Cambridge University Press. 354 p.

Szurgot, M., Rozniakowski K., Wojtatowicz T. W., and Polanski K. 2008. Investigation of microstructure and thermophysical properties of Morasko iron meteorites. *Crystal Research and Technology* 43:921-930.